Characterization and Modeling of $La_{1-x}Sr_xCoO_{3-\delta}$ Solid Oxide Fuel Cell Cathodes Using Nonlinear Electrochemical Impedance Techniques

Timothy James McDonald

A dissertation
submitted in partial fulfillment of the
requirements for the degree of

Doctor of Philosophy

University of Washington

2014

Committee:

Prof. Stuart Adler, Chair

Prof. Daniel Schwartz

Prof. Eric Stuve

Program Authorized to Offer Degree:
Chemical Engineering

University of Washington

Abstract

Characterization and Modeling of $La_{1-x}Sr_xCoO_{3-\delta}$ Solid Oxide Fuel Cell Cathodes Using Nonlinear Electrochemical Impedance Techniques

Timothy James McDonald

Chair of the Supervisory Committee:
Professor Prof. Stuart Adler
Chemical Engineering

Solid Oxide Fuel Cells (SOFCs) provide a highly efficient means of chemical to electrical energy conversion, and as such they represent a desirable bridge between current heavy reliance on fossil fuel energy and expanded roles of clean alternative energy sources. There are however significant challenges preventing the wide spread commercialization of SOFCs. Of primary concern is the high costs associated with high temperature operation, and reduced performance in the desired intermediate temperature regime. Mixed ionic and electronic conducting materials, such as $La_{1-x}Sr_xCoO_{3-\delta}$, offer increased performance for oxygen reduction due to their ability to transport oxygen ions and extend the active region of the electrode beyond the electrode/electrolyte interface.

This work primarily explores two aspects of SOFC cathode performance (using the mixed conductor $La_{1-x}Sr_xCoO_{3-\delta}$ as a model electrode material) the affects of inhomogeneous cation compositions on the surface exchange rate and the effects of humidity on electrode performance and behavior. Inhomogeneous compositions are explored by studying the electrochemical response of well characterized highly-crystalline, thin-film, microelectrodes using both linear and nonlinear electrochemical spectroscopy. A dual surface/dual bulk compositional model is used to characterize the main affects of both lateral (parallel to the surface) and axial (perpendicular to the surface) compositional variations. Humidity

effects are also studied using linear and nonlinear electrochemical impedance spectroscopy, but on porous electrodes, for which a 1-dimensional, dual transport, altered surface thermodynamic model is used to characterize the observed effects.

Finally a new electrochemical technique called Simultaneous Chemical and Electrochemical Impedance Spectroscopy (SCEIS) is proposed which uses dual perturbations to elicit more detailed information about currently indistinguishable co-limiting processes occurring within mixed-conducting porous electrodes. Initial experimental work on assessing the feasibility of such an experiment is reported.

TABLE OF CONTENTS

LIST OF FIGURES

Chapter 1

BACKGROUND

Solid Oxide Fuel Cells (SOFCs) provide a highly efficient means of chemical to electrical energy conversion, and as such they represent a desirable bridge between current heavy reliance on fossil fuel energy and expanded roles of clean alternative energy sources. In particular, SOFCs high tolerance to catalyst poisoning, allowing for direct conversion of current fossil fuel sources, makes them ideal candidates for many current energy applications such as: auxiliary power units in large vehicles, residential power generation, and industrial power generation in a combined SOFC-gas turbine system.

Unfortunately, several factors have prevented the wide spread commercialization of SOFC systems. Of primary concern is the high operating temperature ($> 900^{\circ}$C), which necessitates a higher system cost for ceramic based interconnects, increases the time required for start-up and shutdown, and causes high rates of cell degradation. Lowering the operating temperature to an intermediate range (500-750°C) is therefore highly desirable, but comes at the cost of decreased efficiency. At lower temperatures, oxygen reduction becomes sluggish, and there is a dramatic increase in overpotential.

The primary components of an SOFC are the porous electrodes (cathode and anode) and the electrolyte. The overall performance of the SOFC depends on the individual performance of the material chosen for each component and optimization of the individual components requires a detailed understanding of the relevant phenomena and material properties. While electrolyte research has advanced to the point where the governing physics are considered well understood, the details of processes occurring in the anode and cathode remain unclear, and thus large electrode overpotential losses at the electrodes remain the primary contributor to poor SOFC performance. In particular, for the low and intermediate

temperature ranges, the oxygen reduction reaction is thought to be the largest contributor to poor SOFC performance and is the subject of much of the research being conducted today.

Mixed ionic and electronic conducting (MIEC) perovskites show promising characteristics for electrode materials in oxygen reduction applications. For materials that do not exhibit significant ionic (or electronic) conductivity, the oxygen reduction reaction is limited to the region where all three phases (gas, electrode, and electrolyte) are present (known as the Three Phase Boundary, TPB). The ability of MIEC materials to transport oxygen ions over long distances increases the active area of the electrode, where the higher the oxygen ion mobility the further the active region of an electrode extends away from the TPB, increasing overall performance.

In this work, $La_{1-x}Sr_xCoO_{3-\delta}$ (LSC) was chosen as a representative cathode material as it exhibits good MIEC behavior and has a large volume of high-quality, independently measured property data. The isolated electrode performance of an LSC cathode will depend on specifics of the thermodynamic, transport, and kinetic behaviors. As such, further development of MIEC perovskite electrodes is aided by an increased understanding of material property effects on rate limiting phenomena. In particular, this work focuses on understanding the effects of compositional variations and environmental conditions on the behavior of LSC electrodes.

1.1 SOFC Materials

One class of MIECs often used in SOFC cathodes are $ABO_{3-\delta}$ transition metal perovskites. In these materials, ion transport is made possible by the formation of oxygen vacancies within the crystal structure of the perovskite. An example crystal structure, for the transition metal perovskite $La_{1-x}Sr_xCoO_{3-\delta}$ (LSC), is shown in Figure 1.1. In this material, the A-site ion La^{3+} is doped with the lower valance state Sr^{2+} ion, while the B-site transition metal ion (Co) can exist in a mixed valance state (2+/3+/4+). The lower valance state dopant creates an intrinsic level of oxygen vacancies related to the amount of dopant (x) and the mixed valance state of the transition metal ion allows for further oxidation and reduction of the

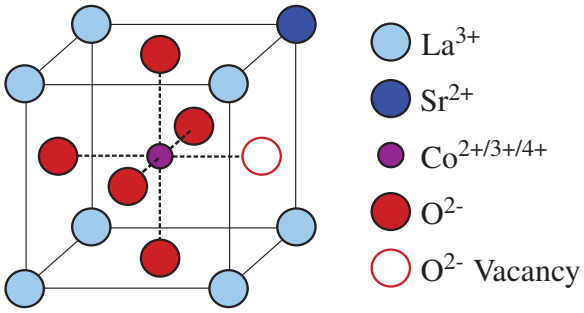

Figure 1.1: Crystal structure of a typical $ABO_{3-\delta}$ transition metal oxide: $La_{1-x}Sr_xCoO_{3-\delta}$

material, giving a total oxygen nonstiochiometry δ.

The choice of an appropriate electrode/electrolyte pair requires careful consideration. An electrolyte material must maintain a high ionic conductivity and electrical insulation in both oxidizing and reducing environments. Also, a good electrode/electrolyte pair will exhibit chemical and mechanical stability. This requires a limited amount of reaction between the electrode and electrolyte (to minimize formation of ionically insulating, or kinetically inactive phases), as well as similar thermal and chemical expansion coefficients to prevent mechanical degradation upon heating. Yttria Stabilized Zirconia (YSZ) is a common electrolyte that exhibits high ionic conductivity at elevated operating temperatures ($> 700^{\circ}$C), but is known to form insulating phases with many La based perovskites. Gadolinia Doped Ceria (GDC) is another common electrolyte that exhibits high ionic conductivity at intermediate temperatures ($500^{\circ}\text{C} - 800^{\circ}\text{C}$), but becomes electronically conducting in reducing gas environments [10, 27]. Previous research has shown success using GDC and YSZ as electrolyte materials with a range of perovskite electrodes, with GDC being used alone at intermediate temperatures or YSZ being used with a GDC protection layer [9, 10]. Both methods are used in this work.

SOFC anode materials are constrained by the necessity for stability in highly reducing conditions, as well as low susceptibility to catalytic poisoning. Because SOFC cathodes are the electrodes of interest in this work, isolation of the cathode response and a single

gas environment are often used to simplify the selection of an appropriate SOFC anode material. Isolation of the cathode response is achieved by using the experimental techniques outlined in section 1.6 along with appropriate reference electrodes or a micro-electrode geometry. The use of single gas environments allows for the same material to be used as both the cathode and anode regardless of the stability of the material in highly reducing environments, as the studies are carried out only in the oxidizing environments of interest to cathode behavior.

1.2 Oxygen Reduction on MIECs

1.2.1 Porous Electrodes

As mentioned previously, MIEC materials provide enhanced catalytic activity through ion transport which allows for the extension of the catalytically active area away from the three phase boundary. An illustration of the oxygen reduction process on a mixed conductor is given in Figure 1.2. There are four main processes which are generally thought to control electrode performance: gas phase diffusion (1), surface exchange reaction (2), oxygen ion transport [bulk (3b), surface (3a)], and electrode/electrolyte charge transfer reaction (4) [2]. Previous research has shown that the contributions of gas phase diffusion and the electrode/electrolyte charge transfer reaction can be mitigated with well designed electrode geometries and careful choice of the electrode/electrolyte pair [2]. This leaves the co-limitation of the surface exchange reaction and oxygen transport within the electrode as the dominant processes.

Despite the simplification of the reduction process to co-limitation, many of the details on the relative importance of each process, which physical properties play a role, and how things change with conditions, remain unclear. As a basis for further investigation, there are a few characteristics reported in literature that are important to consider. First, many researchers observe a segregation of the B-site cation toward the surface of both porous and thin-film perovskite electrodes [7, 14, 17, 29, 31, 47]. This inhomogeneous cation

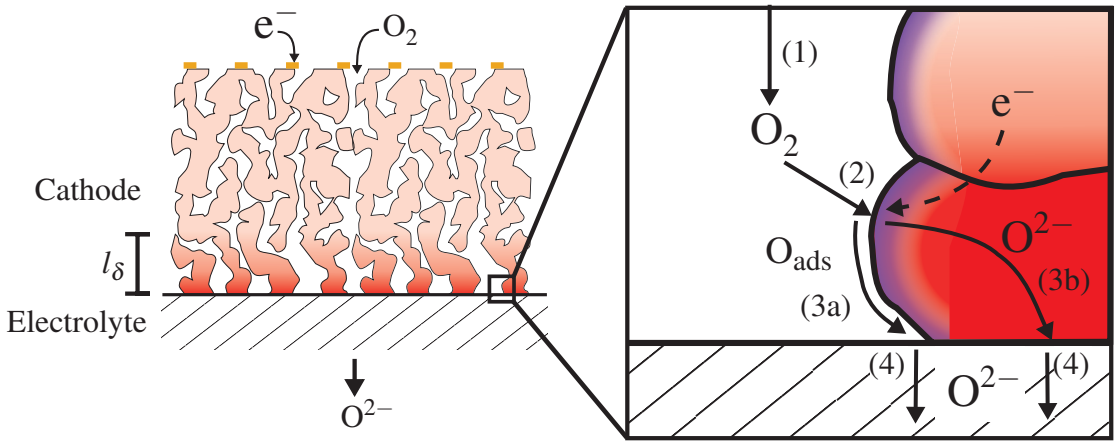

Figure 1.2: Illustration of the possible pathways for oxygen reduction on a porous mixed conductor.

composition affects not just the literal surface of the electrode, but also the region of bulk material near the surface, indicated in Figure 1.2 as the purple colored area. Significant deviation of the near-surface bulk from actual bulk compositions can cause deviations from predicted thermodynamic, transport, and kinetic properties.

Second, the size of the active region of the electrode (defined as the utilization length l_δ in Figure 1.2) will affect the transport behavior. Work by Adler *et al.* found that a 1-dimensional transport model (discussed further in section 3.1.1) could accurately predict linear impedance results under conditions of facile oxygen transport (or long utilization lengths) [1, 4]. Alternatively, Fleig *et al.* and Kreller have found that when utilization lengths are on the same order as geometrical features within a porous electrode, complex 2- and 3-dimensional transport becomes important, as does the exact microstructure of the electrode [19, 28]. This work was expanded by Kreller and Lu *et al.* to include the effects of parallel bulk and surface transport pathways as well as altered material thermodynamics [28, 38].

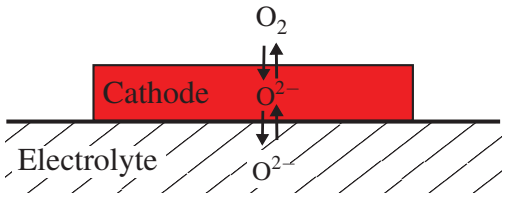

Figure 1.3: Illustration of the possible pathways for oxygen reduction on a thin-film mixed conductor.

1.2.2 Thin Film Electrodes

Further simplification of the oxygen reduction process is achieved by restriction of the electrode geometry to dense thin films. For a dense film with a thickness sufficiently below a critical value, resistance to transport of both oxygen gas and oxygen ions becomes negligible, producing a diffusionally equilibrated film [26]. The behavior of such films is then controlled by the two remaining processes: the surface exchange reaction and the electrode/electrolyte charge transfer reaction. Figure 1.3 illustrates this simplified reduction process.

1.3 Generalized Thermodynamics

As mentioned previously, the high ionic conductivity and catalytic activity of LSC is due to the presence of oxygen vacancies (see Figure 1.1) which are generally denoted by the oxygen nonstoichiometry δ. The oxygen nonstiochiometry in a mixed-conducting perovskite depends on the base material, dopant species, temperature, and p_{O_2}. For the transition metal perovskite $La_{1-x}Sr_xCoO_{3-\delta}$, two methods have been used to study oxygen nonstoichiometry over a range of environmental conditions and dopant amounts (x): thermogravimetric analysis [40, 41, 43] and coulometric titration [35, 36]. Thermogravimetric analysis measures the change in mass of a sample (corresponding to the formation of vacancies) to determine the oxygen nonstoichiometry for different environmental conditions. Coloumetric titration

measures the current resulting from ionic diffusion of oxygen in a coulometric cell to determine the total flux of oxygen over time. The integration of this flux can then be related to changes in the oxygen nonstoichiometry of the sample. While it is theoretically possible to establish an absolute value of the nonstoichiometry with both methods, Lankhorst *et al.* (who used coloumetric titration) only measured changes in oxygen nonstoichiometry, and used absolute values measured at specific conditions by Mizusaki *et al.* (who used thermogravimetric analysis) to establish an absolute scale. In general both groups found that the oxygen nonstoichiometry of LSC increases with increasing Sr doping, increasing temperature, and decreasing p_{O_2}.

The thermodynamic studies of LSC also showed several characteristics that are consistent with a metallic or semi-metallic band structure. Mizusaki *et al.* report a decreasing electronic conductivity with increasing temperature, consistent with metallic conduction, for all materials with a Sr dopant level above $\sim$0.1 and for all temperatures above $\sim$500°C (metallic behavior was seen at much lower temperatures for the higher Sr content, down to room temperature for a Sr dopant level above 0.5) [41]. A low Seebeck coefficient was also reported under similar conditions, further indicating a metallic band structure. Finally, the shape of the nonstoichiometry vs oxygen partial pressure (p_{O_2}) trend indicates metallic behavior as well. Figure 1.4 shows the trend of δ versus p_{O_2} for several different mixed conductors. It is generally understood that the presence of a plateau arises from a p-n transition within semiconducting materials, occurring at the point where the transition metal is predominately in the neutral valance state (corresponding to $\delta = x/2$). Therefore the absence of such a plateau in the LSC trend further indicates a metallic nature.

Both Lankhorst *et al.* and Mizusaki *et al.* have derived models for the relationship of oxygen nonstoichiometry to experimental conditions [36, 40]. The following sections cover a general derivation of an LSC thermodynamic model, detailed descriptions of the literature models, and a generalization of both models to develop a continuously defined empirical model.

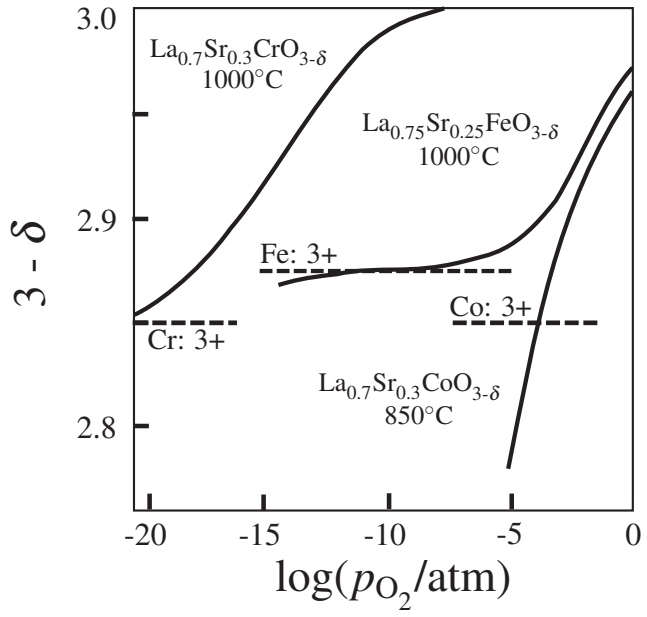

Figure 1.4: Comparison of nonstoichiometry (δ) versus p_{O_2} for different materials, adapted from Reference [40]. Semi-conducting materials LSF and LSCr show a plateau at $\delta = x/2$ (value of δ at this point is indicated by a dashed line), while metallic LSC does not.

1.3.1 Literature Thermodynamic Models

The reduction of mixed-conducting perovskites can be written in Kröger-Vink notation as:

$$O_2^{gas} + 2V_O^{\cdot\cdot} + 4e' \rightleftharpoons 2O_O^{\times} \tag{1.1}$$

where O_2^{gas} is diatomic gas phase oxygen, $V_O^{\cdot\cdot}$ is a lattice oxygen vacancy (with a local charge of 2+), e' is an electron (with a local charge of 1–), and $O_O^{\times}$ is a neutral occupied oxygen lattice site. Equilibrium of the reaction is given by the following relationship between electrochemical potentials (μ):

$$\mu_{O_2^{gas}} + 2\left(\mu_{Vo^{\cdot\cdot}} - \mu_{O_O^{\times}}\right) + 4\mu_{e'} = 0 \tag{1.2}$$

Because lattice oxygen vacancies ($V_O^{\cdot\cdot}$) and occupied oxygen lattice sites ($O_O^{\times}$) cannot be defined independently, it is common to describe a combined species, indicated by the parentheses in Eqn (1.2), called the vacancy building unit (v), hereafter referred to as vacancies.

$$\mu_{O_2^{gas}} + 2\mu_v + 4\mu_{e'} = 0 \tag{1.3}$$

Assuming a random dilute solution of vacancies and ideal gas behavior, the electrochemical potential of oxygen and vacancies can be approximated as:

$$\mu_{O_2^{gas}} = \mu^{o}_{O_2^{gas}} + RT \ln p_{O_2} \tag{1.4}$$

$$\mu_v = \mu_v^{o} + RT \ln x_v + \gamma_v \tag{1.5}$$

where μ_i^{o} is the standard state electrochemical potential of species i, p_{O_2} is the partial pressure of gaseous oxygen, x_v is the mole fraction of vacancies, and γ_v represents non-ideal interactions between vacancies. Because the definition of a vacancy building unit incorporates conservation of oxygen sites, the configurational entropy scales with the natural log of the ratio of oxygen vacancies to occupied oxygen sites:

$$x_v = \frac{\delta}{3-\delta} \tag{1.6}$$

where the concentration of oxygen vacancies is given by the oxygen nonstoichiometry ($[\mathrm{Vo}^{\cdot\cdot}] = \delta$) and the concentration of occupied oxygen sites is given by the conservation of lattice sites $\left(\delta + \left[\mathrm{O}_{\mathrm{O}}^{\times}\right] = 3\right)$.

While the origin and form of non-ideal interactions between vacancies is a subject of debate, the charged nature of vacancy building units means that γ_v will be dependent on the electrical state of the material, and thus indistinguishable from energetic changes in the electrochemical potential of electrons. For a metallic conductor electrons are delocalized and configurational entropy can be ignored, giving a direct relationship between the electron electrochemical potential and γ_v, with the addition of a standard state term:

$$\mu_{e'} = \mu_{e'}^{\mathrm{o}} + \frac{1}{2}\gamma_v \tag{1.7}$$

Combination of Equations (1.3-1.7) gives:

$$RT \ln p_{\mathrm{O}_2} = \left(-2\mu_v^{\mathrm{o}} - 4\mu_{e'}^{\mathrm{o}} - \mu_{\mathrm{O}_2^{\mathrm{gas}}}^{\mathrm{o}}\right) - 2RT \ln \frac{\delta}{3-\delta} - 4\gamma_v \tag{1.8}$$

which represents a general thermodynamic relationship for oxygen vacancies.

1.3.1.1 Lankhorst Model

Lankhorst *et al.* modeled the energetic portion of vacancy interactions (γ_v) with shifts in the Fermi level, assuming a rigid electron band (constant density of states around the Fermi level). For the Lankhorst model, electrons freed by vacancy formation cause shifts in the Fermi level by filling of the rigid band:

$$\gamma_v = \frac{(n - n^{\mathrm{o}})}{g_o} \tag{1.9}$$

where n is the number of electrons added by vacancy formation, n^{o} is the electron occupancy at zero vacancy concentration, and $g\left(E_f\right)$ is the density of states at the Fermi level. Electroneutrality of the material requires:

$$n - n^{\mathrm{o}} = 2\delta - \mathrm{x} \tag{1.10}$$

x	E_{ox} (kJ mol^{-1})	S_{ox} (J mol^{-1} K^{-1})	g_o (kJ mol^{-1})
0.2	-334.1	69.5	0.0159
0.4	-301.4	69.6	0.0159
0.7	-294.5	70.5	0.0152

Table 1.1: Parameters for the thermodynamic model developed by Lankhorst *et al.*, given in Equation (1.11). Values of parameters are taken from Ref. [36]

The Lankhorst model for thermodynamic behavior of LSC is given by combination of Equations (1.8), (1.9), (1.10), and replacing the sum of standard state electrochemical potentials with a dopant dependent standard state enthalpy $[E_{ox}(\mathrm{x})]$ and entropy $[S_{ox}(\mathrm{x})]$:

$$RT\ln p_{\mathrm{O}_2} = \left(E_{ox}(\mathrm{x}) - TS_{ox}(\mathrm{x}) - \mu^{\theta}_{\mathrm{O}_2^{\mathrm{gas}}}(T)\right) - 2RT\ln\frac{\delta}{3-\delta} - 4\frac{(2\delta-\mathrm{x})}{g_o(\mathrm{x})} \tag{1.11}$$

where $\mu^{\theta}_{\mathrm{O}_2^{\mathrm{gas}}}(T)$ represents the additional temperature dependence of the standard state chemical potential of oxygen described by an empirically formulated temperature function [48]. Values of $E_{ox}(\mathrm{x})$, $S_{ox}(\mathrm{x})$, and $g_o(\mathrm{x})$, obtained by fitting coulometric titration data are given in Table 1.1 as a function of dopant concentration.

1.3.1.2 Mizusaki Model

Mizusaki *et al.* left the source of energetic vacancy interactions undefined, deriving instead an empirical dependence:

$$\gamma_v = \frac{1}{2}a(\mathrm{x})\delta \tag{1.12}$$

Following a similar derivation used in the previous section, the Mizusaki model for thermodynamic behavior is:

$$\frac{RT}{2}\ln p_{\mathrm{O}_2} = \left(\Delta H^{\theta}_o(\mathrm{x}) - a(\mathrm{x})\delta\right) - T\left(\Delta S^{\theta}_o(\mathrm{x}) + R\ln\frac{\delta}{3-\delta}\right) \tag{1.13}$$

x	ΔH_o^θ (kJ mol^{-1})	ΔS_o^θ (J mol^{-1} K^{-1})	a (kJ mol^{-1})
0	-211	-96.2	221
0.1	-205	-99.2	552
0.2	-146	-86.6	418
0.3	-112	-76.1	385
0.5	-70.7	-64.4	222
0.6	-61.9	-60.7	172
0.7	-57.3	-58.6	134

Table 1.2: Parameters for the thermodynamic model developed by Mizusaki *et al*., given in Equation (1.13). Values of parameters are taken from Ref. [26]

.

where $\Delta H_o^\theta(\mathrm{x})$ and $\Delta S_o^\theta(\mathrm{x})$ also represent standard state enthalpy and entropy respectively, but differ from those given by Lankhorst *et al*. because of the additional $\mu^\theta_{\mathrm{O}_2^{\mathrm{gas}}}(T)$ and $4\mathrm{x}/g_o(\mathrm{x})$ terms. Values of $\Delta H_o^\theta(\mathrm{x})$, $\Delta S_o^\theta(\mathrm{x})$and $a(\mathrm{x})$, obtained by fitting thermogravimetric analysis data are given in Table 1.2.

1.3.2 General Thermodynamic Model

The models of Lankhorst *et al*. and Mizusaki *et al*. are essentially equivalent; the only differences being explicit and implicit dependencies of the standard state terms on temperature and dopant concentration. Both models include a linear dependence on δ for the vacancy interactions and a standard state free energy term broken into a standard state enthalpy and entropy that are empirically dependent on dopant level. It should also be noted that over the temperature range studied, the effect of the additional temperature dependence in the Lankhorst *et al*. model was negligible.

While it is possible to use either literature model within the regime of conditions tested for that model, model accuracy will decrease when extrapolating to other conditions. In addition, having discrete values for the parameters as a function of dopant level makes it difficult to generate or verify a model for a material of unknown composition. In an effort to minimize these effects, a general thermodynamic model is created that spans the largest set of conditions possible, and is continuous with respect to T, p_{O_2}, and x. Because the form of the x dependence is not known *a priori*, and because the exact T dependence varies slightly between literature models, Equation (1.8) is first generalized as:

$$RT \ln p_{O_2} = \Delta G^{\theta}_{vf}(T, x) - 2RT \ln \frac{\delta}{3} - c_{fit}(x)\delta \tag{1.14}$$

where the standard state terms are collected into an effective standard state free energy of vacancy formation $\left[\Delta G^{\theta}_{vf}(T, x)\right]$ with an unspecified temperature and dopant level dependence, and the vacancy interaction term is given a linear δ dependence with an unspecified dopant level dependence of the fitting parameter $c_{fit}(x)$. An additional assumption, of a solvent approximation, was made for the configurational entropy of the vacancy building unit ($\delta/(3-\delta) \approx \delta/3$). This was done for calculation purposes and provides nearly identical results for the range of δ found in all collected nonstoichiometry data.

In order to determine the dependencies of the fitting parameters $\Delta G^{\theta}_{vf}(T, x)$ and $c_{fit}(x)$, least squares fits of nonstoichiometry data collected in References [36, 40] were obtained as a function of temperature and dopant level. It should be noted that some data collected by Lankhorst *et al.*, for $La_{0.8}Sr_{0.2}CoO_{3-\delta}$, seemed to exhibit an absolute nonstoichiometry error, where the values of nonstoichiometry appear to approach a non-zero intercept as the material approaches full stoichiometry (shown in Figure 1.5). Because Lankhorst *et al.* established the absolute scale for the nonstoichiometry by assigning an absolute value for a single nonstiochiometry from data collected by Mizusaki *et al.* (and then defining all other values as relative to that absolute value) the absolute scaling is subject to errors in the single measurement. This error becomes negligible as the absolute value of the vacancy becomes large compared to experimental error (which is likely the case for the higher dopant concen-

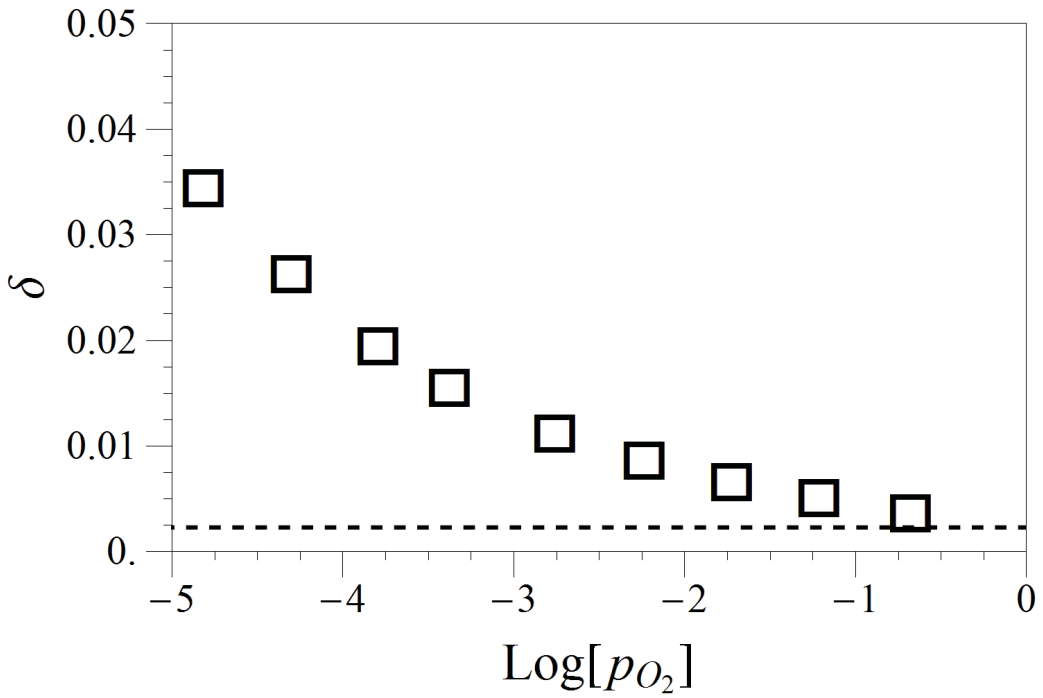

Figure 1.5: Plot of nonstoichiometry (δ) reported by Lankhorst *et al.* [36] versus p_{O_2}, for LSC-82, at the lowest T measured (700°C). This corresponds to the lowest nonstoichiometry values measured by Lankhorst *et al.* A fullstoichiometry plateau occurs at $\delta = 0.0023$, indicated by the dashed line.

tration experiments). To account for the offset error, all nonstoichiometry values reported for $La_{0.8}Sr_{0.2}CoO_{3-\delta}$ were adjusted by subtracting out the value of the apparent plateau (shown in Figure 1.5), which was determined by least squares fitting (further discussion of fitting process is given in Appendix A.1). No other data set seemed to contain this error.

$c_{\text{fit}}(\text{x})$ was found to have a weak dependence on dopant level, and could be assumed to be independent of dopant level without negatively affecting the accuracy of the model. Conversely, $\Delta G^{\theta}_{\text{vf}}(T,\text{x})$ was found to depend heavily on temperature and dopant level as shown in Figure 1.6 (data points represent independent least squares fits at each set of conditions T and x). From the trends indicated in Figure 1.6, $\Delta G^{\theta}_{\text{vf}}(T,\text{x})$ was assumed to

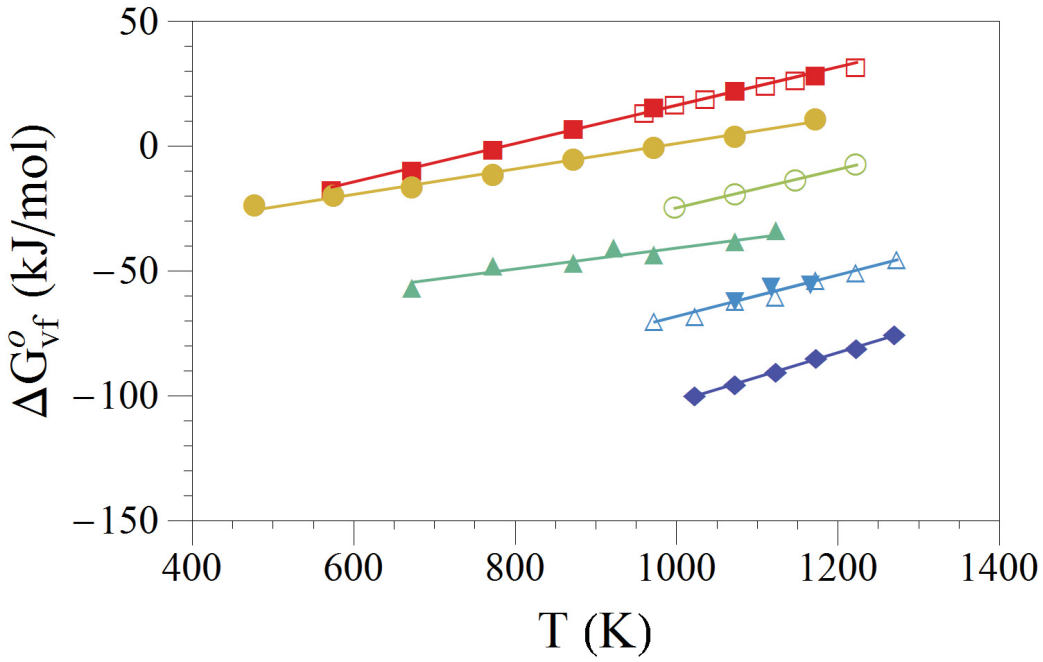

Figure 1.6: Data points indicate values of $\Delta G^{\theta}_{\mathrm{vf}}(T,\mathrm{x})$ extracted from least squares fitting of literature nonstoichiometry data for LSC. Fits were obtained at Sr concentrations of x=0.1 (red squares), x=0.5 (yellow circles), x=0.4 (light green circles), x=0.3 (dark green upawards triangles), x=0.2 (light blue downard triangles), and x=0.1 (dark blue diamonds). Lines indicate best fits of $\Delta H^{\theta}_{\mathrm{vf}}(\mathrm{x})$ and $\Delta S^{\theta}_{\mathrm{vf}}(\mathrm{x})$ to extracted $\Delta G^{\theta}_{\mathrm{vf}}(T,\mathrm{x})$ values. Open data points are fits to data from Reference [36] and closed data points are fits to data from Reference [40].

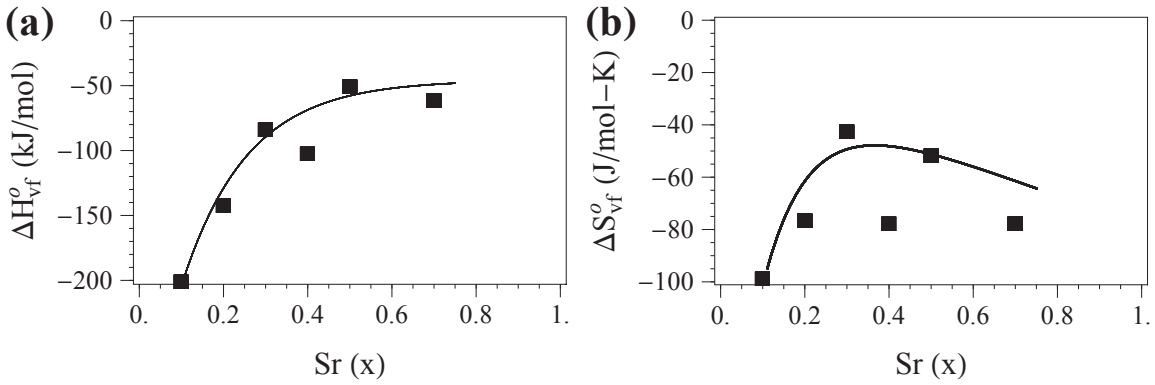

Figure 1.7: Data points represent best fits of $\Delta H^{\theta}_{\mathrm{vf}}(\mathrm{x})$ and $\Delta S^{\theta}_{\mathrm{vf}}(\mathrm{x})$ to fit values of $\Delta G^{\theta}_{\mathrm{vf}}(T,\mathrm{x})$. Lines indicate best fits of the full continuous generalized thermodynamic model, given by Equations (1.15) and (1.16a,b), to nonstoichiometry values taken from literature. The only adjustable parameters are the empirical parameters $\Delta H^{\theta}_{\mathrm{fit,i}}$ and $\Delta S^{\theta}_{\mathrm{fit,i}}$ from Equations (1.16a,b).

have a linear temperature dependence. Combining this dependence with a dopant level independent c_{fit} gives the following modified thermodynamic model:

$$RT \ln p_{O_2} = \left(\Delta H^{\theta}_{\text{vf}}(\text{x}) - T\Delta S^{\theta}_{\text{vf}}(\text{x})\right) - 2RT \ln \frac{\delta}{3} - c_{\text{fit}}\delta \tag{1.15}$$

where $\Delta H^{\theta}_{\text{vf}}(\text{x})$ and $\Delta S^{\theta}_{\text{vf}}(\text{x})$ are standard state enthalpy and energy of vacancy formation, and are only dependent on x. To determine the appropriate form of the dopant level dependence of $\Delta H^{\theta}_{\text{vf}}(\text{x})$ and $\Delta S^{\theta}_{\text{vf}}(\text{x})$, discrete values were obtained for each dopant level by least squares fitting of extracted $\Delta G^{\theta}_{\text{vf}}(T,\text{x})$ values, using Equation (1.15) (fits shown in Figure 1.6, fitting methods given in Appendix A.1). Figure 1.7 illustrates the extracted values as a function of x. Visual inspection of the data points in Figure 1.7 does not reveal an obvious trend for $\Delta H^{\theta}_{\text{vf}}(\text{x})$ or $\Delta S^{\theta}_{\text{vf}}(\text{x})$. However, it is reasonable to assume that the values collected at $\text{x} = 0.4$ will be the most variable (due to the small sample size), which is illustrated by a deviation for the $\text{x} = 0.4$ point in the otherwise consistent exponential trend (indicated by the solid fit line) of $\Delta H^{\theta}_{\text{vf}}(\text{x})$. Excluding $\text{x} = 0.4$, the dependence for $\Delta H^{\theta}_{\text{vf}}(\text{x})$ that best approximates the observed trend is a negative exponential that decays to 0 with increasing x, while the best approximation for the dependence of $\Delta S^{\theta}_{\text{vf}}(\text{x})$ is a coupled negative exponential (that decays to 0 with increasing x) and a negative linear trend that becomes increasing negative with increasing x. These dependencies can be expressed as:

$$\Delta H^{\theta}_{\text{vf}}(\text{x}) = \Delta H^{\theta}_{\text{fit,1}} + \Delta H^{\theta}_{\text{fit,2}} e^{-x\Delta H^{\theta}_{\text{fit,3}}} \tag{1.16a}$$

$$\Delta S^{\theta}_{\text{vf}}(\text{x}) = \Delta S^{\theta}_{\text{fit,1}} + \Delta S^{\theta}_{\text{fit,2}} e^{-x\Delta S^{\theta}_{\text{fit,3}}} + x\Delta S^{\theta}_{\text{fit,4}} \tag{1.16b}$$

where $\Delta H^{\theta}_{\text{fit,i}}$ and $\Delta S^{\theta}_{\text{fit,i}}$ correspond to empirical fitting parameters. Combination of Equation (1.15) and Equations (1.16a,b) give a model that is continuous in T, p_{O_2}, and x. The values for the empirical fitting parameters were determined by least squares fitting of the data collected from References [36, 40], and are reported in Table 1.3. Figure 1.7 illustrates the resulting trends for $\Delta H^{\theta}_{\text{vf}}(\text{x})$ and $\Delta S^{\theta}_{\text{vf}}(\text{x})$. In Figure 1.8, data collected by Lankhorst *et al.* and Mizusaki *et al.* for $La_{0.8}Sr_{0.2}CoO_{3-\delta}$ and $La_{0.3}Sr_{0.7}CoO_{3-\delta}$, are compared to all three available models. The generalized continuous model shows similar or improved ac-

$\Delta H^{\theta}_{\text{fit},1}$ (kJ mol^{-1})	$\Delta H^{\theta}_{\text{fit},2}$ (kJ mol^{-1})	$\Delta H^{\theta}_{\text{fit},3}$	c_{fit} (kJ mol^{-1})
-45.8	-302	6.44	228
$\Delta S^{\theta}_{\text{fit},1}$ (J mol^{-1} K^{-1})	$\Delta S^{\theta}_{\text{fit},2}$ (J mol^{-1} K^{-1})	$\Delta S^{\theta}_{\text{fit},3}$	$\Delta S^{\theta}_{\text{fit},4}$ (J mol^{-1} K^{-1})
-20.1	-192	9.34	-58.7

Table 1.3: Best fit values of the full continuous generalized thermodynamic model given by Equations (1.15) and (1.16a,b). Values are obtained by least squares fitting of nonstoichiometry data taken from References [36, 40].

curacy across the range of conditions tested as the previously reported literature models.

1.3.3 Thermodynamic Factor

The electrode behavior of LSC depends not only on the absolute value of the nonstoichiometry, but also the rate of change in nonstoichiometry with changing oxygen partial pressure. For example, the rate of change can be used to predict the driving force for the surface exchange reaction for small to moderate deviations from equilibrium; this is discussed in more detail in Section 1.4. This rate of change can be expressed in terms of a thermodynamic factor A (or γ), which is a descriptor for how facile oxygen vacancy formation is, under a given set of conditions. The thermodynamic factor(A_o) and equilibrium thermodynamic factor (A_o) are defined as:

$$A = -\frac{1}{2\gamma} = -\frac{1}{2}\frac{\partial \ln f_{\text{O}_2}}{\partial \ln \delta} \tag{1.17a}$$

$$A_o = -\frac{1}{2\gamma_o} = -\frac{1}{2}\frac{\partial \ln p_{\text{O}_2}}{\partial \ln \delta} \tag{1.17b}$$

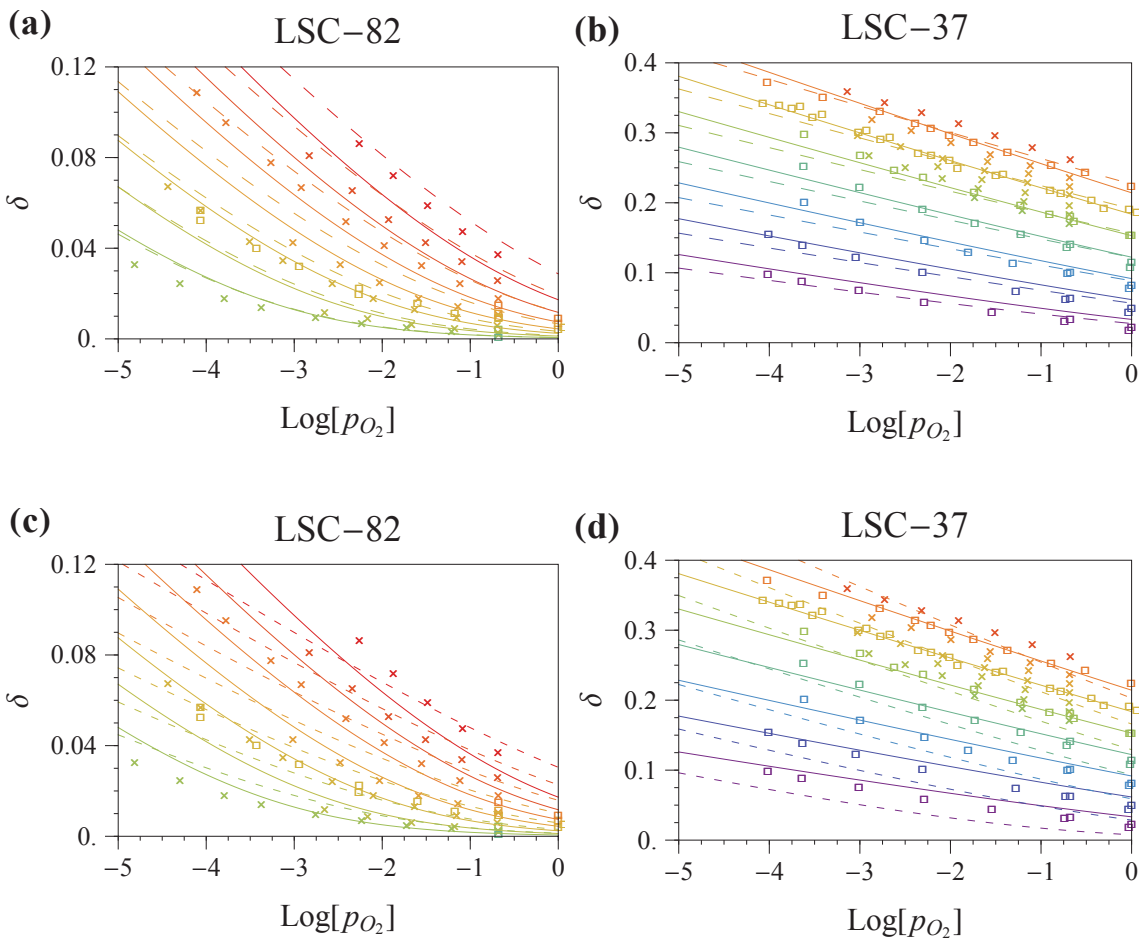

Figure 1.8: Comparison of thermodynamic models to measured nonstoichiometry for LSC-82 (plots a, c) and LSC-37 (plots b, d). Measured values are extracted from Lankhorst *et al.* (adjusted for observed offsets) [36] (squares), and Mizusaki *et al.* [40] (×'s), with colors indicating temperature from 300°C (purple) to 1000°C (dark red); longer wavelength colors indicate higher temperatures. Plots (a,b) compare the generalized model (continuous lines) to the Lankhorst model [36] (long dashed lines), while plots (c, d) compare the generalized model (continuous lines) to the Mizusaki model *et al.* [40] (short dashed lines).

This definition yields the following formulas for A_O, for each of the previously discussed thermodynamic models:

$$A_o \approx 1 + \frac{4\delta}{g_o RT} \qquad \text{(Lankhorst)} \tag{1.18a}$$

$$A_o \approx 1 + \frac{a\delta}{RT} \qquad \text{(Mizusaki)} \tag{1.18b}$$

$$A_o = 1 + \frac{c_{fit}\delta}{2RT} \qquad \text{(General)} \tag{1.18c}$$

The larger the value of A_o the more readily oxygen vacancies are formed. Values of A_o close to 1 are indicative of a small concentration of oxygen vacancies and small driving forces.

1.4 Oxygen Reduction Rate Law

Equation (1.1) defines the oxygen reduction reaction occurring at the surface of mixed-conducting electrodes (often referred to as the surface exchange reaction). Because this reaction is non-faradaic, contains charged species, and can exhibit large nonlinear driving forces, the form of the kinetic rate law is of important consideration. The most appropriate form of a kinetic rate law for this reaction will depended on the primary source of free energy shifts (energetic or entropic) within the mixed conductor and their magnitude.

Systems with ideal thermodynamic behavior and a predominately entropic driving force (such as changes in concentration of neutral reactive species) can be described with a mass action rate law that involves a forward and backward rate dependent on species concentrations and kinetic coefficients (which are independent of the driving force). Alternately, reactions that involve primarily energetic changes in the free energy (such as faradaic reactions of charged species) can be described with a Butler-Volmer type rate law. In both cases, it is often difficult to correct for nonideal thermodynamics, especially under increasingly large driving forces. Adler *et al*. have proposed a general rate law based on transition state theory and nonideal thermodynamics to incorporate both energetic and entropic contributions to the free energy of reactive species, while maintaining agreement with thermo-

dynamics in the limit of equilibrium [3]:

$$r_j = k_j e^{-\Delta G^{\theta}_{f,j}/RT} e^{\left[(1-\beta_j)\Delta E_j\right]/RT} \left[1 - e^{-\Lambda_j/RT}\right] \prod_i c_i \tag{1.19}$$

where Λ_j is the free energy driving force of the reaction, $\Delta G^{\theta}_{f,j}$ is the forward rate free energy barrier, ΔE_j is the relative shifts in free energy of the products versus reactants, c_i are the concentrations of reacting species in the forward direction, j is the reaction index indicating which rate law (and corresponding assumptions) is being used, and i is the species index. The general rate law can also be written more succintly as:

$$r_j = \Re_o \left[1 - e^{-\Lambda_j/RT}\right] \tag{1.20}$$

where $\Re_o$ represents the equilibrium exchange rate. Using the generalized thermodynamic model given in Equation (1.14), the free energy driving force for the overall oxygen reduction reaction can be written as:

$$\Lambda = RT \ln\left[p_{\mathrm{O}_2} (x_v)^2\right] - \Delta G^{\theta}_{\mathrm{vf}} + 3c_{\mathrm{fit}} x_v \tag{1.21}$$

where $\Delta G^{\theta}_{\mathrm{vf}}$ is the standard state free energy of the reaction (vacancy formation). Examining Equation (1.21) shows that the free energy driving force for oxygen reduction on LSC contains energetic ($3c_{\mathrm{fit}} x_v$) and entropic ($RT \ln p_{\mathrm{O}_2} (x_v)^2$) contributions.

To determine the specific form of the rate law it is important to establish a reaction mechanism and possible rate determining steps. A likely mechanism for oxygen reduction on LSC is given by Adler *et al.*, consisting of three sequential steps [3]. First, gaseous oxygen is adsorbed onto a surface vacancy site through either a physisorption or chemisorption process. Next, a second vacancy reacts with the adsorbed diatomic oxygen, in the presence of electrons, causing dissociation of the diatomic and creation of two monotomic oxygen ions. Finally, the surface oxygen ions can be incorporated into the bulk through reaction with bulk oxygen vacancies. The exact charge of reactive intermediates is not established, but the general form of this reaction mechanism can be expressed in Kröger-Vink notation

as:

$$O_2^{gas} + V_{O_s}^{q_s\cdot} + q_{ads}e' \rightleftharpoons (O_2)_{O_s}^{q_{O_2}\cdot} \quad \text{(Adsorption)} \tag{1.22a}$$

$$(O_2)_{O_s}^{q_{O_2}\cdot} + V_{O_s}^{q_s\cdot} + q_{diss}e' \rightleftharpoons 2\,(O)_{O_s}^{q_O\cdot} \quad \text{(Dissociation)} \tag{1.22b}$$

$$(O)_{O_s}^{q_O\cdot} + V_{O_b}^{\cdot\cdot} + q_{incorp}e' \rightleftharpoons O_{O_b}^{\times} + V_{O_s}^{\cdot\cdot} \quad \text{(Incorporation)} \tag{1.22c}$$

$$O_2^{gas} + 2V_O^{\cdot\cdot} + 4e' \rightleftharpoons 2O_{O_b}^{\times} \quad \text{(Overall Reaction)} \tag{1.22d}$$

where $V_{O_s}^{q_s\cdot}$ is a surface oxygen vacancy with a charge of q_s, $V_{O_b}^{\cdot\cdot}$ is a bulk oxygen vacancy with a charge of 2+, $O_{O_b}^{\times}$ is a bulk neutral occupied oxygen lattice site, $(O)_{O_s}^{q_O\cdot}$ is a surface occupied oxygen lattice site of charge q_O, and $(O_2)_{O_s}^{q_{O_2}\cdot}$ is an adsorbed diatomic oxygen with a charge of q_{O_2}. The sum of electrons transfered in each individual step must equal the total number of electrons transfered. In this case:

$$q_{ads} + q_{diss} + q_{incorp} = 4 \tag{1.23}$$

If a single step is rate determining, then the free energy driving force of that particular step becomes proportional to the overall driving force, while the other steps reach a pseudo-equilibrium.

$$\Lambda_j = \frac{\Lambda}{\lambda_j} \tag{1.24a}$$

$$\Lambda_{i\neq j} \approx 0 \tag{1.24b}$$

Using a similar approach to determing the thermodynamics for the overall reaction in Section 1.3, a free energy driving force for each step can be derived. These results can be summarized by using a general form of the driving force:

$$\Lambda_j = RT \ln Q_j - \Delta G_j^{\theta} + \Delta E_j \tag{1.25}$$

Values of Q_j, ΔG_j^o, and ΔE_j, for the three steps outlined above are given in Table 1.4. Manipulation of Table 1.4 and Equations (1.19,1.24a,1.25) can yield specific rate laws for

Step (j)	Q_j	ΔE_j	ΔG_j^o
Adsorption	$\frac{p_{O_2}\Gamma_s}{\Gamma_{sO_2}}$	$q_{ads}\gamma_v$	$\mu^\theta_{sO_2} - \mu^\theta_{O_2} - \mu^\theta_s$
Dissociation	$\Gamma_s\Gamma_{sO_2}$	$q_{diss}\gamma_v$	$-\mu^\theta_{sO_2} - \mu^\theta_s$
Incorporation	$\frac{x_v}{\Gamma_s}$	$q_{incorp}\gamma_v$	$\mu^\theta_s - \mu^\theta_v$
Total Reaction	$p_{O_2}x_v^2$	$4\gamma_v$	$-\mu^\theta_{O_2} - 2\mu^\theta_v$

Table 1.4: Components of the thermodynamic driving force for different rate limiting steps, based on equation (1.25).

each reaction step in terms of overall reaction species and the overall thermodynamic driving force.

$$r_{ads} = k_{o,ads}p_{O_2}x_v e^{\frac{3c_{fit}x_v}{RT}\left(\frac{1}{2}+\frac{q_{ads}(1-\beta_{ads})-q_{diss}}{8}\right)}\left[1-e^{-\Lambda_{ads}/RT}\right] \tag{1.26a}$$

$$r_{diss} = k_{o,diss}p_{O_2}x_v^2 e^{\frac{3c_{fit}x_v}{RT}\left(1-\frac{\beta_{diss}q_{diss}}{4}\right)}\left[1-e^{-\Lambda_{diss}/RT}\right] \tag{1.26b}$$

$$r_{incorp} = k_{o,incorp}x_v e^{\frac{3c_{fit}x_v}{RT}\left(\frac{(1-\beta_{incorp})q_{incorp}}{2}\right)}\left[1-e^{-\Lambda_{incorp}/RT}\right] \tag{1.26c}$$

Of particular interest is the case of an entropically limited dissociation reaction. For this reaction, the barrier to dissociation is not an energy barrier but rather it is the limited site availability for materials with dilute concentrations of vacancies. It is entropically unfavorable to have multiple vacancies come together to dissociate the adsorbed diatomic oxygen. For this mechanism, the symmetry parameter β would be 1, indicating that the entire limitation is on the forward rate, without any appreciable resistance to the backwards rate. This particular rate law is often called the Dissociative-Adsorption rate law (r_{da}), to emphasize the fact that given the nature of the entropic barrier, adsorption and dissociation often occur almost simultaneously. Studies on LSC electrodes, both porous and dense, using several different fabrication techniques, and across a range of experimental conditions found that the dissociative-adsorption type rate law best describes the observed electrode

behavior [3, 16, 29, 50].

1.5 Mixed-Conducting Transport

A necessary component of any electrode is high electrical conductivity. As discussed in section 1.3, LSC materials generally exhibit metallic or semi-metallic behavior with correspondingly high electronic conductivity at elevated temperatures or high Sr dopant concentrations. Mizusaki *et al*. report transitions from semi-conducting to metallic behavior (where metallic behavior is indicated by decreasing conductivity with increasing temperature and low seeback coefficients) at different temperatures for different Sr dopant concentrations [41]. Most transitions occure below 500°C (except for the undoped case), and for highly doped (x>0.5) materials metallic behavior extends all the way to room temperature [41]. At 1 atm p_{O_2} and over a temperature range of 400-800°C, the reported electronic conductivity for all LSC materials ranges from ∼700-1600 S/cm [41].

What makes materials like LSC advantageous is their relatively high ionic conductivity, in addition to their high electronic conductivity, giving rise to mixed-conductivity. A variety of techniques have been used to study the increased oxygen ionic conductivity in LSC and similar materials including: electron blocking methods [45], oxygen 18 isotope tracer experiments with post analysis using Secondary Ion Mass Spectrometry (SIMS) [8], and conductivity relaxation [46, 44]. Such works typically report diffusion coefficients ($\tilde{D}$, D_{chem}, or D^*) which are closely related to the oxygen vacancy diffusivity (D_v), and can be used to determine the oxygen ionic conductivity ($\sigma_{O^{2-}}$) if the concentration of oxygen vacancies and thermodynamic factors are known. SÃÿgaard *et al*. report oxygen ion conductivities for LSC-64 over a range of temperatures (650-1000°C) and oxygen partial pressures (10^{-4}-10^{0} atm), with all values falling in the range of 0.01 to 0.5 S/cm [44]. Comparison of the ionic conductivity and electronic conductivity of LSC materials shows that while there is a significant amount of ionic conductivity, the transference number of electrons remains near unity.

1.5.1 Bulk vs Surface Diffusion

As discussed in section 1.2, one of the co-limiting steps involved in the overall process of oxygen reduction on a mixed-conducting electrode is two parallel solid phase transport processes. To clarify, it is possible that oxygen ions, or more generally oxygen species, can diffuse not only through the bulk of LSC (as oxygen vacancies), but also along the surface or near-surface bulk region of the electrode as oxygen vacancies, oxygen ions, adsorbed oxygen diatoms, or some other form of oxygen species. Current measurement techniques are limited in their ability to distinguish between these parallel process, but in general it seems that the role of the surface transport pathway has more readily observable effects in materials with small oxygen vacancy concentrations.

A study by La O' *et al.* on dense, thin film, micro patterned LSM electrodes, using electrochemical impedance spectroscopy, found a moderate diffusion resistance, indicated by the presence of a Warburg like element in the impedance spectra [33]. However, estimation of a bulk diffusion coefficient based on the total observed resistance yielded values that were many orders of magnitude higher than values seen in literature. This led the authors to conclude that surface diffusion, which occurs over a smaller cross sectional area and would thus produce a larger resistance for similar transport properties and conditions, is the likely diffusion pathway for the studied LSM electrodes. A similar study by Adler, for LSC electrodes, predicts diffusion coefficients that are in line with those reported in the literature in conditions that favor oxygen vacancy formation (high Sr content, high temperature, low p_{O_2}), but start to deviate as conditions begin to favor small vacancy concentrations [1].

Lu *et al.* and Kreller have attempted to model the parallel diffusion pathways in LSC for both linear and nonlinear electrochemical impedance spectroscopy measurements [38, 28]. The study by Lu *et al.* found significant evidence of surface diffusion in LSC-82 electrodes but no evidence for LSC-64 electrodes, using linear electrochemical impedance spectroscopy. Alternatively, Kreller found evidence for surface diffusion in both materials, but with reduced contributions for LSC-64, examining the full nonlinear response. In both

cases, the relative amount of surface diffusion to bulk diffusion was characterized by a dimensionless parameter ν, which represents the ratio of surface diffusion rates to bulk diffusion rates (further details in section 3.1.1). Lu *et al.* report values of ν, for LSC-82 at 650°C, ranging from 0.1 to 15 over a range of p_{O_2} from 0.01 to 1 atm. Kreller reports values of ν, for LSC-64 at 600°C, ranging from ~0.01-0.1 over a range of p_{O_2} from 0.01 to 0.21 atm. Interestingly, in both cases the values of ν increase with increasing temperature and p_{O_2}. Because the rate of surface diffusion for oxygen vacancies should scale proportionally with the concentration of oxygen vacancies, the inverse dependence of ν compared to oxygen vacancy concentration suggests that oxygen species (referred to as a surface interstitial oxygens in the cited work) rather than oxygen vacancies are responsible for the surface transport pathway.

1.6 Electrochemical Techniques

Electrochemical measurement techniques provide direct access to information about the behavior of charged systems. Electrochemical testing can be broken into two broad categories, DC and AC. A DC polarization response curve can provide information about the total system performance. Alternatively, an AC Electrochemical Impedance Spectroscopy (EIS) measurement provides information about processes occurring within a system separated by timescale. Timescale separation is achieved by measuring across a range of AC frequencies, which yields responses at each frequency that are only determined by processes with a similar timescale as the applied frequency. This type of a measurement is particularly useful for systems that have several complex processes occurring on different timescales.

1.6.1 Linear Electrochemical Impedance Spectroscopy

In a linear EIS measurement, the system is perturbed from equilibrium with a small amplitude AC signal over a range of frequencies. The AC perturbation can be either voltage

or current and is maintained until the system reaches a periodic steady state. The periodic steady state perturbation and response are recorded and analyzed (using a Fast Fourier Transform) to determine the amplitudes and phases of periodic signals. The amplitude and phase of the response depend on the electrochemical characteristics of the system. For an EIS measurement consisting of a current perturbation, the perturbation and complex response can be written as:

$$i = \frac{1}{2}\left(\tilde{i}e^{j\omega_o t} + \tilde{i}e^{-j\omega_o t}\right) \tag{1.27a}$$

$$V = \frac{1}{2}\left(\tilde{V}_1 e^{j\omega_o t} + \tilde{V}_1^* e^{-j\omega_o t}\right) \tag{1.27b}$$

where $\tilde{i}$ is the real amplitude of the current perturbation, $\tilde{V}_1$ is the complex first order Fourier coefficient corresponding to a periodic signal occurring at the perturbation frequency ω_o, and the superscript $*$ represents the complex conjugate. The complex Fourier coefficient characterizes both the amplitude and phase shift of the voltage response. The current perturbation coefficient has no complex conjugate because because it is a purely real signal with no phase shift.

The characteristics of the system are described by the relative changes in the response to a given perturbation. Relative changes in the response can be represented by the impedance (Z), which is defined as the ratio of complex Fourier coefficients:

$$Z = \frac{\tilde{i}_1}{\tilde{V}_1} = \frac{i_1'}{V_1' + jV_1''} = Z' + jZ'' \tag{1.28}$$

where superscripts indicate the real part ($'$) and imaginary part ($''$) of complex numbers.

Impedance results are often plotted in Nyquist form, where the negative imaginary component of the impedance (-Im Z = -Z'') is plotted against the real component (Re $Z = Z'$). Figure 1.9 gives example Nyquist plots for typical half cell measurements on SOFCs. Frequency is not plotted directly, but is increasing in the direction of the origin. Different features can be seen in in the Nyquist plots corresponding to processes that are occurring at different timescales. The porous electrode impedance spectra shows 3 distinct features: an offset of the high frequency intercept (intercept closest to the origin), a semi-circular

arc at intermediate frequencies, and a half teardrop (or Gerischer) shape at low frequencies. These three features are generally attributed to the ohmic resistance of ion transport in the electrolyte (Z_{elyte}), kinetic losses from the charge transfer reaction at the electrode/electrolyte interface (Z_{int}), and co-limitation of electrode ion transport and kinetics of the surface exchange reaction (Z_{chem}). The different timescales for dominant processes leads to a clear separation of the electrolyte, interfacial, and electrode effects, while the co-limiting electrode processes remain convoluted. In contrast, a dense thin-film electrode impedance spectra often exhibits only 2 distinct features: A high frequency ohmic offset and a low frequency kinetic semi-circle. The small diffusion resistances (from short diffusion pathways) and increased kinetic resistances (from small electrode surface areas) lead to a primarily surface exchange dominated electrode response.

Single features of impedance spectra can be defined by characteristic values of the response. In Figure 1.9b the thin film semi-circular arc is defined by a characteristic resistance corresponding to the arc width (R_{chem}) and a characteristic frequency corresponding to the frequency at the peak of the arc (ω_{chem}). The charactersitic frequency can also be related to a characteristic time constant $t_{\text{chem}} = 1/\omega_{\text{chem}}$. Another set of characteristic values is shown in Figure 1.9a , where the characteristic resistance is given as the arc height (R_{c}) rather than the arc width (R_{chem}), with the normally defined characteristic frequency (ω_{chem}). The choice of characteristic parameters is somewhat arbitrary , although consistency is necessary for accurate analysis, but arc height (R_{c}) may be beneficial in situations where overlapping features obscure the measurement of the arc width(R_{chem}).

1.6.2 NonLinear Electrochemical Impedance Spectroscopy

In a NLEIS measurement, the system is perturbed from equilibrium with a moderate amplitude AC signal over a range of frequencies and perturbation amplitudes. The relative size (moderate versus small) of a perturbation amplitude is based on the DC *i-V* characteristics of the sample system. A small amplitude is defined by a range over which the *i-V* curvature is linear. EIS measurements (small amplitude) will only produce a response

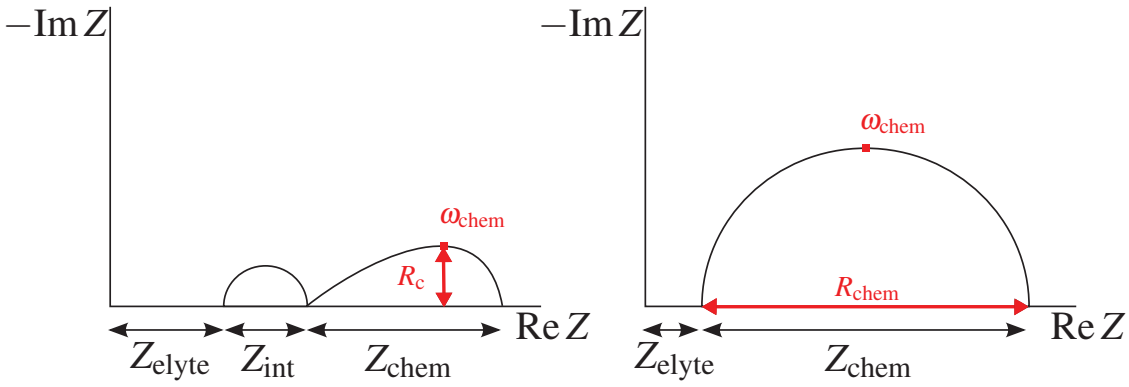

(a) Porous electrode (b) Dense thin-film micro electrode

Figure 1.9: Example impedance response of MIEC electrodes plotted in Nyquist form.

signal at the first order harmonic of the perturbation frequency. A moderate amplitude perturbation is defined by a range over which the *i*-*V* curvature is slightly nonlinear. NLEIS measurements (moderate amplitude) produce periodic signals at higher order harmonics of the perturbation frequency. A moderate amplitude is distinguished from a large amplitude by the number of measurable higher order harmonics present. Figure 1.10 illustrates the difference between the response signals for the two measurements in the time domain. For NLEIS the AC perturbation is generally the current, which is maintained until the system reaches a periodic steady state (before the measurement begins). The periodic steady state current perturbation and voltage response are recorded and analyzed (with a Fourier Transform), to determine the amplitudes and phases of the harmonics. The voltage response for an NLEIS measurement has a form similar to Equation (1.27b), but contains signals at integer multiples of the current perturbation:

$$i = \frac{1}{2}\left(\tilde{i}e^{j\omega_o t} + \tilde{i}e^{-j\omega_o t}\right) \tag{1.29a}$$

$$V = \frac{1}{2}\sum_{k=0}^{\infty} \tilde{V}_k e^{jk\omega_o t} + \tilde{V}_k^* e^{-jk\omega_o t} \tag{1.29b}$$

where k represents the order of the harmonic response.

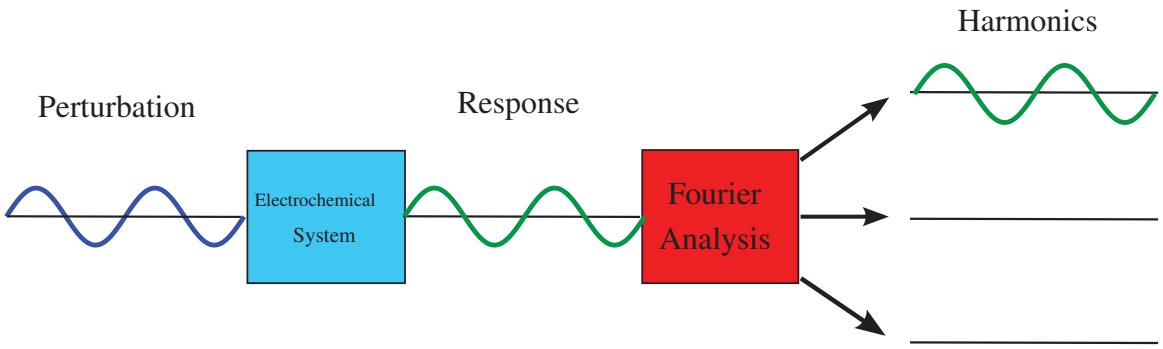

(a) EIS measurement

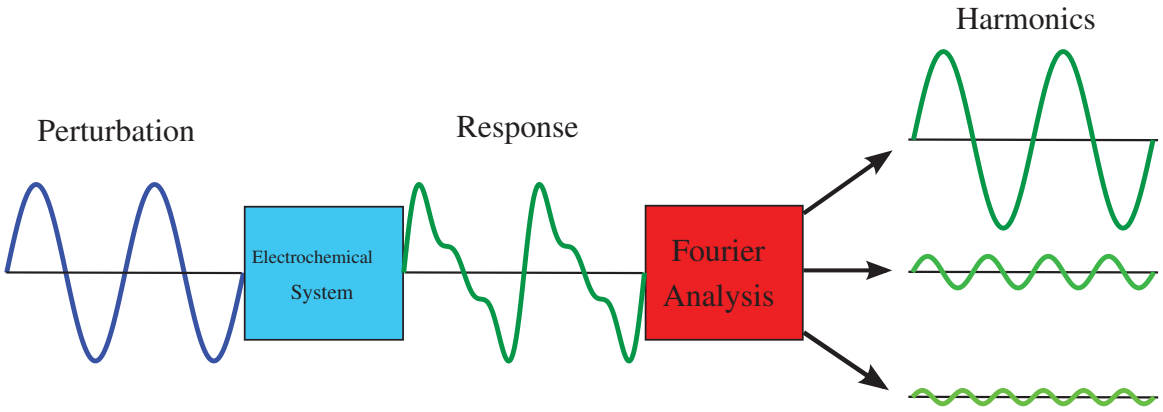

(b) NLEIS measurement

Figure 1.10: Time domain response of linear and nonlinear impedance measurements.

For each frequency used, a range of perturbation amplitudes is tested. The size and number of harmonics measured depends on the magnitude of the perturbation amplitude and the extent of nonlinearity within the system. Perturbation amplitudes are chosen to extend from the linear regime to the moderately nonlinear regime. The voltage response Fourier coefficients, measured over a range of perturbation amplitudes, can then be fit to a power series to extract amplitude independent complex coefficients ($\tilde{V}_{k,m}$):

$$\tilde{V}_k\left(\tilde{i},\omega_o\right)=\sum_{r=1}^{\infty}\alpha^{k+2r-2}\tilde{V}_{k,k+2r-2}\left(\omega_o\right) \tag{1.30}$$

where α is a dimensionless current (which allows $\tilde{V}_{k,m}$ to have units of volts) and the index $m=k+2r-2$ represents the order in α of the coefficients for a skipping order power series. α is given by the relationship $\alpha=\tilde{i}/i^*$ where i^* represents a characteristic current amplitude indicating the onset of nonlinearities, and is related to the characteristic voltage and resistance through Ohm's law:

$$V^*=i^*R_{\text{chem}} \tag{1.31}$$

A moderate amplitude perturbation corresponds to α on the order of 1. Use of a moderate amplitude allows for the truncation of the infinite Fourier series and power series with no appreciable loss in accuracy. Typical NLEIS measurements can be truncated at a 5$^{\text{th}}$ order response, giving the following expansions for the first three Fourier coefficients:

$$\tilde{V}_1\left(\tilde{i},\omega_o\right)=\alpha\tilde{V}_{1,1}\left(\omega_o\right)+\alpha^3\tilde{V}_{1,3}\left(\omega_o\right)+\alpha^5\tilde{V}_{1,5}\left(\omega_o\right)+O\left[\alpha^7\right] \tag{1.32a}$$

$$\tilde{V}_2\left(\tilde{i},\omega_o\right)=\alpha^2\tilde{V}_{2,2}\left(\omega_o\right)+\alpha^4\tilde{V}_{2,4}\left(\omega_o\right)+O\left[\alpha^6\right] \tag{1.32b}$$

$$\tilde{V}_3\left(\tilde{i},\omega_o\right)=\alpha^3\tilde{V}_{3,3}\left(\omega_o\right)+\alpha^5\tilde{V}_{3,5}\left(\omega_o\right)+O\left[\alpha^7\right] \tag{1.32c}$$

Like EIS, it is the relative size of the response (rather than the absolute size) that represents the characteristics of the system. The first order harmonic can be scaled to the current perturbation amplitude in a manner similar to the EIS response, and in fact it can be shown that the linear portion of the first order response $\tilde{V}_{1,1}$ is directly proportional to the

impedance obtained by EIS in the limit of small perturbations ($\alpha << 1$).

$$Z = \frac{\tilde{V}_1}{\tilde{i}} = \frac{\alpha \tilde{V}_{1,1}}{\alpha i^*} = \frac{\tilde{V}_{1,1}}{i^*} \tag{1.33}$$

Because $\tilde{V}_{1,1}$ represents an amplitude independent coefficient, the constraint of small perturbations ($\alpha << 1$) is unnecessary and only used for clarification purposes, but in fact the linear characteristics of the system (given by the impedance Z) can always be calculated from the linear portion of the first order response $\tilde{V}_{1,1}$. In a fashion similar to the linear characteristics, the nonlinear characteristics can be determined by examining the behavior of the lowest order terms in the second and third harmonics, $\tilde{V}_{2,2}$ and $\tilde{V}_{3,3}$. While the first order harmonic response was scaled to the amplitude of the current perturbation, the higher order harmonics are scaled to the magnitude of the first order harmonic, to give the extent of nonlinearities relative to the overall response size:

$$\tilde{U}_{2,2} = \frac{\tilde{V}_{2,2}}{\left|\tilde{V}_{1,1}\left(\omega_o \to 0\right)\right|} \tag{1.34a}$$

$$\tilde{U}_{3,3} = \frac{\tilde{V}_{3,3}}{\left|\tilde{V}_{1,1}\left(\omega_o \to 0\right)\right|} \tag{1.34b}$$

where $U_{2,2}$ and $U_{3,3}$ are dimensionless scaled harmonics that represent the relative extent of nonlinearity of the system at a given perturbation frequency. Typically, the electrolyte and interfacial contributions to the magnitude of the first harmonic response will be removed for this calculation as the nonlinearities arise primarily from the electrode behavior. This electrode specific magnitude can be defined in terms of the characteristic resistance and current:

$$\tilde{U}_{2,2} = \frac{\tilde{V}_{2,2}}{R_{\text{chem}} i^*} = \frac{\tilde{V}_{2,2}}{V^*} \tag{1.35a}$$

$$\tilde{U}_{3,3} = \frac{\tilde{V}_{3,3}}{R_{\text{chem}} i^*} = \frac{\tilde{V}_{3,3}}{V^*} \tag{1.35b}$$

Figure 1.11 gives example 2$^{\text{nd}}$ and 3$^{\text{rd}}$ harmonic spectra, plotted in Nyquist form. The curves are the harmonic spectra, while the lines (commonly referred to as phasor lines) are drawn to indicate the point on the spectrum that corresponds to a particular response

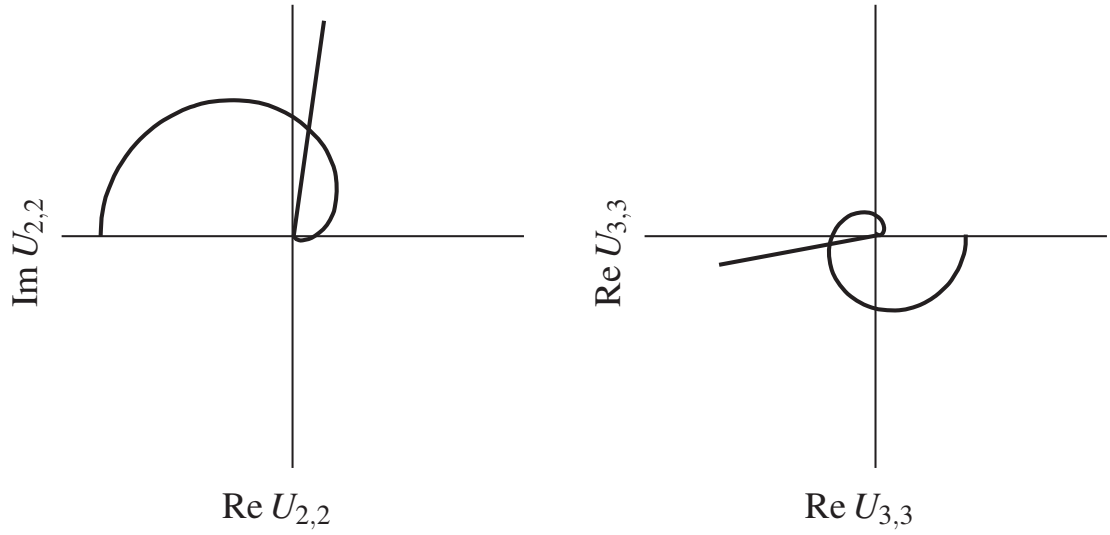

(a) 2nd harmonic spectra

(b) 3rd harmonic sepctra

Figure 1.11: Example higher order harmonic spectra and phasor lines, plotted in Nyquist form.

frequency (usually the characteristic frequency ω_{chem}). Because each harmonic occurs at an integer multiple of the perturbation frequency, the phasor lines will not be indicating the point where there perturbation frequency is equal to ω_{chem}, but rather when the harmonic response frequency is equal to ω_{chem}. Thus, 2nd harmonic phasor lines indicate a perturbation frequency of $\omega_{\text{chem}}/2$, while 3rd harmonic phasor lines indicate a perturbation frequency of $\omega_{\text{chem}}/3$.

1.6.2.1 NLEIS Scaling for a Non-Stationary Response

A strength of the NLEIS technique is that the nonlinear response of the system is probed as a function of frequency. This makes NLEIS less susceptible to errors arising from convolution of system drift and system nonlinearities, so long as the system remains stationary over the period of a single frequency measurement. Previous studies on porous LSC elec-

trodes have shown a timescale for system drift which is much longer than that of a complete NLEIS measurement. However, the thin films discussed in Chapter 2 exhibit system drift on a timescale similar to an entire NLEIS measurement, but longer than a single frequency NLEIS measurement.

For a diffusionally equilibrated thin film, the semi-circular impedance response can be fit to an equivalent RC circuit of the form:

$$Z = \frac{R_{chem}}{1 + j\left(\frac{\omega}{\omega_{\text{chem}}}\right)} \tag{1.36}$$

The real and imaginary components of the impedance are then given as:

$$Z' = \frac{R_{chem}}{1 + \left(\frac{\omega}{\omega_{\text{chem}}}\right)^2} \tag{1.37a}$$

$$Z'' = -\frac{R_{chem}\left(\frac{\omega}{\omega_{\text{chem}}}\right)^2}{1 + \left(\frac{\omega}{\omega_{\text{chem}}}\right)^2} \tag{1.37b}$$

As long as the characteristic parameters (R_{chem} and ω_{chem}) are stable over the length of a single frequency NLEIS measurement, they can be fit from the measured impedance, using Equations (1.37a,b), at each frequency measured. This allows the impedance and the higher order harmonics to be normalized to characteristic parameters for each frequency point by point. Figure 1.12 illustrates a graphical representation of the point by point normalization technique, where each arc (solid lines) indicates the expected linear impedance at different frequency points collected over time, and used to scale the higher order harmonics for the corresponding frequencies.

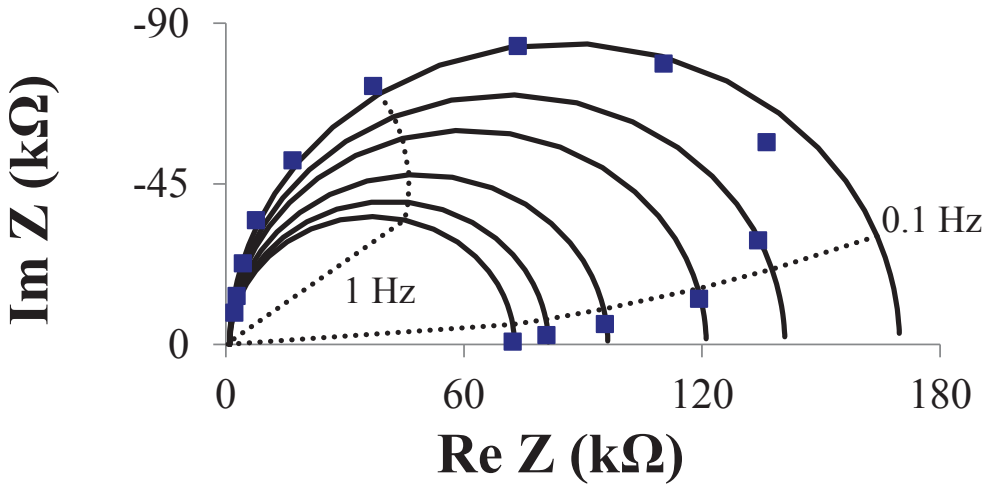

Figure 1.12: Illustration point to point normalization for NLEIS technique. Data points represent impedance data collected for an LSC-64 thin film electrode at 640°C and 1 atm p_{O_2}. Solid lines indicate expected impedance arcs for each individual data point collected and dashed lines indicate constant frequency. Characteristic resistance is seen to increase with time causing a drift in the low frequency intercept towards the origin. Data points closest to the origin represent higher frequencies and shorter measurement times and are seen to approximately agree with the same expected impedance arc, indicating a small amount of drift.

Chapter 2

LSC THIN FILMS: CHARACTERIZATION AND MODELING

Linear and nonlinear electrochemical testing and modeling of highly-oriented, crystalline thin films of $La_{0.8}Sr_{0.2}CoO_{3-\delta}$ (LSC-82) and $La_{0.6}Sr_{0.4}CoO_{3-\delta}$ (LSC-64) is reported in this chapter. The films were studied using linear and nonlinear electrochemical impedance spectroscopy across a range of temperatures, partial pressures of oxygen, and film thickness to assess thermodynamic and kinetic behavior. Wilson *et al*. [50] have shown the nonlinear response of polycrystalline LSC-82 to be consistent with the dissociative adsorption kinetic mechanism and enhanced thermodynamic behavior (higher concentration of vacancies and higher thermodynamic factor) from similarly doped freestanding bulk material. Kawada *et al*. [26] and DeMartini [16] studied polycrystalline LSC-64 films and found the thermodynamic behavior to be suppressed from that of similarly doped freestanding bulk material, with DeMartini reporting that both the LSC-82 and LSC-64 films studied agreed with the dissociative-adsorption rate law allowing for altered thermodynamic behavior. Crumlin *et al*. [12], found similar thermodynamic behavior for highly oriented crystalline LSC-64 films. The consistent findings between both materials being the alteration of expected thermodynamic behavior and the adherence to a dissociative-adsorption rate law.

Previous research by this group on similarly made LSC-82 films attempted to model electrode behavior using the dissociative-adsorption rate law combined with a film composition model that integrated cation segregation by defining a small uniform surface layer with an increased Sr dopant concentration [29]. While this model successfully captured some of the previously mentioned altered electrode behavior, inconsistencies remained. One possible source of error is the simplification of Sr segregation to axial (perpendicu-

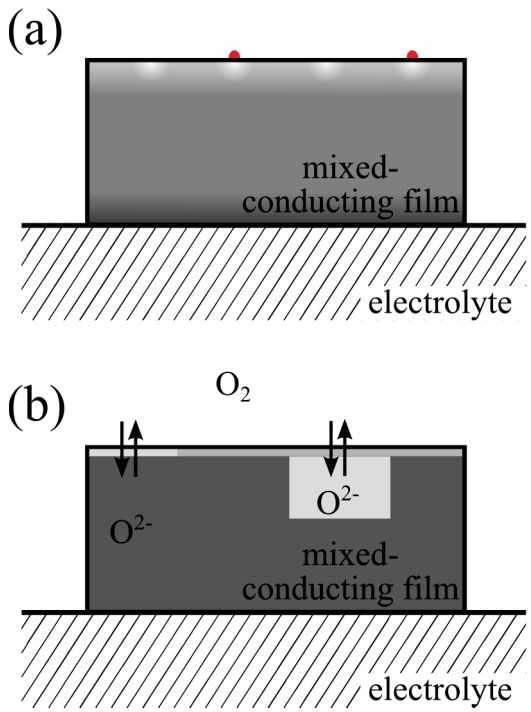

Figure 2.1: Schematic of dense thin film electrodes with an example illustration of a likely physical distribution of Sr content (with exaggerated gradients) (a) and with averaged cation compositions for a mixed surface/mixed bulk model (b). Gray scale colors indicate changing Sr dopant concentrations, while red surface dots indicate precipitates of a Sr rich phase.

lar to surface) compositional inhomogeneity without accounting for any lateral (parallel to surface) compositional inhomogeneity. An artistic rendering of likely compositional variation of Sr cations within the film is given in Figure 2.1, with color gradients indicating the exclusion of Sr dopant both laterally and axially, eventually resulting in precipitation of Sr rich phases (discussed further in Section 2.3.1). This work seeks to expand on the previous study to include the effects of lateral Sr distribution and different nominal film compositions in a nonlinear electrode model for prediction of NLEIS measurements.

2.1 Theory

As discussed in section 1.2.2, a dense film with a thickness sufficiently below a critical value can be assumed to be diffusionally equilibrated. The dominant processes for such a film are the surface exchange reaction and the electrode/electrolyte charge transfer reaction. The use of impedance based electrochemical measurements allows for the separation of the two processes, and thus the isolated study of oxygen exchange kinetics on the surface of the thin films.

2.1.1 Compositional Model

Changes in local cation composition within electrodes can create significant deviations from expected electrode behavior. In this work a new compositional model is proposed that incorporates inhomogeneity within the bulk and along the surface of the electrode (illustrated in Figure 2.1). This mixed surface/mixed bulk model is intended as a simplistic representation that can capture the most important effects of parallel surface reactions and altered bulk thermodynamics. A simplistic model is used (as opposed to more realistic cation distributions) as it was found to be impossible to distinguish between well-defined and averaged distributions due to the diffusionally equilibrated nature of the films (TJ McDonald and Stuart Adler unpublished data).

The mixed surface/mixed bulk model (Figure 2.1) defines two surface regions and two bulk regions within the film, each with a distinct composition. Because the surface exchange reaction is very sensitive to the exact composition of the surface, while the bulk thermodynamic response is only sensitive to averaged values of bulk compositions, the surface regions are assumed to contain a negligible volume and do not contribute to the bulk thermodynamic response. This allows for the precise description of surface compositions untied to the averaged parameters that define bulk thermodynamics. There are then three independent parameters that define the surface regions, and are determined by the behavior

of the surface exchange reaction:

$$x_{s1}(T),\ x_{s2}(T),\ \varepsilon_1(T) \tag{2.1}$$

where x_{si} is the mole fraction of Sr dopant in surface region i and ε_1 is the fraction coverage of surface region 1. Bulk regions are similarly defined by three parameters:

$$x_{b1}(T),\ x_{b2}(T),\ \lambda_1(T) \tag{2.2}$$

where x_{bi} is the mole fraction of Sr dopant in bulk region i and λ_1 is the fractional volume of bulk region 1. The bulk parameters are, however, not completely independent; the total composition is restricted buy the nominal composition of the deposited electrode material. Allowing for some loss of Sr cations through Sr precipitation gives the following inequality for the nominal composition (x_n):

$$\lambda_1 x_{b1} + (1-\lambda_1)\, x_{b2} \leq x_n \tag{2.3}$$

Bulk region parameters are determined by the bulk thermodynamic behavior of the film.

2.1.2 Thin Film Electrode Model

The behavior of MIEC electrodes can be modeled by analyzing the oxygen vacancy material balance within the film. For a diffusionally equilibrated thin film of a uniform composition, the material balance for oxygen vacancies simplifies to that of a stirred tank reactor:

$$\frac{V}{V_m}\frac{\partial \delta}{\partial t} = a_e N_v|_{\text{elyte}} - a_s N_v|_{\text{gas}} \tag{2.4}$$

where V is the volume of the electrode, a_e is the area of the electrode/electrolyte interface, a_s is the total surface area of the electrode, V_m is the molar volume of the electrode material, t is time, and N_v is the area-specific flux of vacancies at either the electrode/electrolyte interface (elyte) or the electrode/gas interface (gas). The flux of vacancies at the gas-exposed interface is controlled by the surface exchange reaction, while the flux of vacancies at the

electrode/electrolyte interface is given by Faraday's Law:

$$N_v|_{\text{gas}} = 2r_{\text{O}_2} \tag{2.5a}$$

$$N_v|_{\text{elyte}} = -\frac{\tilde{i}}{2F}\cos(\omega t) \tag{2.5b}$$

where r_{O_2} is the net rate of molecular O_2 reduction (in moles $\text{O}_2/\text{cm}^2/\text{s}$), $\tilde{i}$ and ω are the current perturbation amplitude and frequency (respectively), and F is FaradayâĂŹs constant. r_{O_2} is assumed to follow the rate law given by Equation (1.26b), with the additional assumptions of the dissociative-adsorption rate law outlined in section 1.4. The four regions of the mixed surface/mixed bulk model establish parallel surface exchange reactions and parallel vacancy accumulation terms, giving a total electrode oxygen vacancy material balance of:

$$\frac{1}{V_m}\left(V_1\frac{\partial\delta_{b,1}}{\partial t} + V_2\frac{\partial\delta_{b,2}}{\partial t}\right) = -a_e\frac{\tilde{i}}{2F}\cos(\omega t) - 2a_1 r_{O_2,1} - 2a_2 r_{O_2,2} \tag{2.6}$$

where V_i is the volume of bulk region i, a_i is the surface area of surface region i, $\delta_{b,i}$ is the oxygen nonstiochiometry in the bulk region i, and r_{O_2} corresponds to the surface exchange reaction taking place in surface region i.

Equilibrium between the regions can be built into the material balance by replacing oxygen nonstiochiometry with the oxygen fugacity in the solid phase, which is uniform everywhere for an equilibrated film. Re-expressing Equation (2.6) in terms of an oxygen fugacity and adjustable parameters from the mixed surface/mixed bulk electrode composi-

tional model gives:

$$\frac{V}{aV_m}\left(\lambda_1\frac{\partial\delta_{b,1}}{\partial\ln f_{O_2}}+(1-\lambda_1)\frac{\partial\delta_{b,1}}{\partial\ln f_{O_2}}\right)\frac{\partial\psi}{\partial t}= -\frac{\tilde{i}}{2F}\cos(\omega t)-2\varepsilon_1 r_{O_2,1}-2(1-\varepsilon_1)r_{O_2,2} \tag{2.7a}$$

$$\frac{\partial\delta_{b,i}}{\partial\ln f_{O_2}}=-\frac{\delta^o_{b,i}}{(A_{o,bi}-1)}\frac{W\left[(A_{o,bi}-1)\,e^{-\frac{1}{2}\ln\frac{f_{O_2}}{p_{O_2}}+(A_{o,b}-1)}\right]}{1+W\left[(A_{o,bi}-1)\,e^{-\frac{1}{2}\ln\frac{f_{O_2}}{p_{O_2}}+(A_{o,bi}-1)}\right]} \tag{2.7b}$$

where V is the total volume of the electrode, a is the cross sectional area of electrode (where $a_e \approx a_s \approx a$ for a thin film), $\delta^o_{b,i}$ is the equilibrium value of the oxygen nonstiochiometry in bulk region i, $A_{o,bi}$ is an equilibrium thermodynamic factor for bulk region i, f_{O_2} is the solid phase oxygen fugacity, and $W[]$ is the Lambert function. It is important to note that $A_{o,bi}$ and $\delta^o_{b,i}$ do not represent additional fitting parameters, as both represent equilibrium values and can thus be explicitly calculated through the thermodynamic relationship given in section 1.3.2, and from the corresponding Sr dopant mole fraction (x_i) for the same region.

Finally, the cell voltage can be related to the oxygen fugacity through the Nernst equation:

$$V=\frac{RT}{4F}\ln\left[\frac{f_{O_2}}{p_{O_2}}\right] \tag{2.8}$$

Equations (1.21), (1.26b), (2.7), and (2.8) can be combined with the characteristic nondimensionalization parameters given in Table 2.1 to give the dimensionless thin film electrode model:

$$U=\psi \tag{2.9a}$$

$$-(\lambda_1\beta_1+(1-\lambda_1)\beta_2)\frac{\partial\psi}{\partial\tau}=-\alpha\cos(\sigma\tau)-\zeta_1\rho_{da,1}-(1-\zeta_1)\rho_{da,2} \tag{2.9b}$$

and

$$\beta_i = \frac{1}{\lambda_1 \frac{\left(A_{\mathrm{o},b1}-1\right)}{A_{\mathrm{o},b1}} + \left(1-\lambda_1\right)\frac{\left(A_{\mathrm{o},b2}-1\right)}{A_{\mathrm{o},b2}}} \frac{W\left[\left(A_{\mathrm{o},bi}-1\right)e^{-\psi+\left(A_{\mathrm{o},bi}-1\right)}\right]}{1+W\left[\left(A_{\mathrm{o},bi}-1\right)e^{-\psi+\left(A_{\mathrm{o},bi}-1\right)}\right]} \tag{2.10a}$$

$$\rho_{\mathrm{da},i} = \left(\frac{1}{2}e^{2\left(A_{\mathrm{o},si}-1\right)-2W\left[\left(A_{\mathrm{o},si}-1\right)e^{-\psi+\left(A_{\mathrm{o},si}-1\right)}\right]}\right)\left(e^{-2\psi}-1\right) \tag{2.10b}$$

$$\zeta_1 = \frac{\theta\left(\delta^o_{v,s1}\right)^2}{\left[\theta\left(\delta^o_{v,s1}\right)^2+\left(\delta^o_{v,s2}\right)^2\right]} \tag{2.10c}$$

$$\theta = \frac{\varepsilon_1 k_{\mathrm{da},1}}{\left(1-\varepsilon_1\right)k_{\mathrm{da},2}} \tag{2.10d}$$

where the dimensionless surface exchange rate given by Equation (2.10b) represents the rate law given by Equation (1.26b), with the additional assumptions for dissociative-adsorption.

Equations (2.9a-b, 2.10a-d) can be used to solve for the first and higher order harmonics, $U_{m,m}$. Environmental conditions enter the model through the equilibrium thermodynamic factors.

It should be noted that for the derived model, changes in surface coverage of regions 1 and 2 are indistinguishable from changes in exchange rate coefficients for surface regions 1 and 2. The combined contributions of the surface coverage and exchange rate coefficients can be defined as a hypothetical ratio of active sites, corresponding to the dimensionless parameter θ.

Quantity	Dimensional Variable	Dimensionless Form	Dimensional Group
Oxygen Fugacity	f_{O_2}	$\psi = \frac{1}{2}\ln\frac{f_{\mathrm{O}_2}}{p_{\mathrm{O}_2}}$	p_{O_2}
Time	t	$\tau = \frac{t}{t^*}$	$t^* = \frac{2FVx^o_{v_\mathrm{b}}}{V_m a A_{o,\mathrm{b}}}\frac{1}{i^*}$
Frequency	ω	$\sigma = \omega t^*$	$\frac{1}{t^*}$
Current Density	$\tilde{i}$	$\alpha = \frac{\tilde{i}}{i^*}$	$i^* = 8F\left(\varepsilon_1\Re_{\mathrm{o},1} + (1-\varepsilon_1)\Re_{\mathrm{o},2}\right)$
Voltage	V	$U = \frac{V}{V^*} = \psi$	$V^* = \frac{RT}{2F}$
Reaction Rate	r_{da}	$\rho_{\mathrm{da}} = \frac{r_{\mathrm{da}}}{\Re_o}$	$\Re_o$

Table 2.1: Dimensionless parameters for the nondimensionalized thin film model.

2.1.3 Electrochemical Response

Analysis of EIS-type measurements often falls into two general categories: equivalent circuit fitting and direct physical models. Equivalent circuit fitting allows for the simple extraction of important characteristics of the electrode behavior, while direct physical models allow for the attribution of characteristic behavior to likely physical phenomena. For the current study, an equivalent circuit is used to define the characteristic behavior of the linear EIS response, and the direct physical model, given by the combination of Equations (2.10a-d), is used to predict trends of the fit characteristics as well as the nonlinear behavior (NLEIS).

The portion of the linear EIS response, for thin film MIEC electrodes, corresponding to the surface exchange reaction can be described using an RC equivalent circuit of the form [23, 26]:

$$Z(\omega) = \frac{i(\omega)}{V(\omega)} = \frac{R_{chem}}{1 + j\frac{\omega}{\omega_{chem}}} \tag{2.11}$$

where Z is the measured impedance, R_{chem} is a characteristic resistance, and ω_{chem} is a characteristic frequency. As defined, R_{chem} represents the width of the impedance arc,

while ω_{chem} represents the angular frequency at the peak of the arc (as illustrated in Figure 1.9). The characteristic resistance of the electrode is related to the linear portion of the surface exchange reaction. Using Equations (2.10a-d, 2.11), the following relationship can be derived:

$$R_{chem} = \frac{RT}{8F^2} \frac{1}{\varepsilon_1 \Re_{O_2,1} + (1-\varepsilon_1)\Re_{O_2,2}} \tag{2.12}$$

A characteristic capacitance (which represents the chemical capacitance of the electrode) can also be defined based on the two previous characteristic parameters:

$$aC_\delta = \frac{R_{chem}}{\omega_{chem}} \tag{2.13}$$

where C_δ is an area specific chemical (faradaic) capacitance of the electrode (units of F/cm^2) and a is the cross sectional area of the film. The chemical capacitance of the electrode is related to the thermodynamics of oxygen vacancy exchange [26]. For the generalized thermodynamic model detailed in section 1.3.2, the following relationship can be derived:

$$C_\delta = -\frac{8F^2L}{V_m}\frac{\partial \delta^o}{\partial \mu_{O_2}} = \frac{4F^2L}{V_m\left(\frac{c_{\text{fit}}}{2} + \frac{RT}{\delta^o}\right)} \tag{2.14}$$

Using Equations (1.15), (1.16a-b), and (2.14), the electrode capacitance in each region can be calculated by solving for δ^o for different conditions given a Sr dopant level. A total volume specific capacitance (VSC) of the mixed bulk thin film is then given by the addition of the parallel capacitances corresponding to the two bulk regions scaled by the thickness of the film (L):

$$\text{VSC} = \frac{C_{\delta,1} + C_{\delta,2}}{L} \tag{2.15}$$

The response to a NLEIS measurement can be modeled using the ordinary differential equation given by Equations (2.10a-d), assuming a solution of the deviation variable ψ that matches the form of the voltage Fourier series outlined in section 1.6.2, and iteratively solving for the harmonic voltage coefficients of interest (further details given in references [5, 49, 51]). The calculated quantities are the impedance $Z(\omega)$ (EIS and NLEIS) as well as 2nd ($U_{2,2}$) and 3rd ($U_{3,3}$) dimensionless harmonic coefficients (NLEIS). Solutions for the

2nd ($U_{2,2}$) and 3rd ($U_{3,3}$) harmonic coefficients provide a complex relationship that depends only on experimental conditions and adjustable parameters for the mixed surface/mixed bulk electrode composition model. As outlined in a previous publication, the 2nd and 3rd harmonic coefficients are expected to depend only on the thermodynamic properties of the film (and thus the adjustable compositional parameters) and not on the linear portion of the surface exchange reaction (R_{chem}) [29].

2.2 Experimental Methods

2.2.1 Film Fabrication

Films studied in this work were prepared by Shao-Horn, Crumlin, Mutoro, and coworkers at the Electrochemical Energy Laboratory at Massachusetts Instituite of Technology with the assistance of the Center for Nanophase Materials Science at Oak Ridge National Laboratory. Details of the fabrication technique can be found in References [32, 34]. LSC powders, of both 20% and 40% Sr concentrations, were synthesized by solid state reaction from stoichiometric mixtures of La_2O_3, $SrCO_3$, and Co_3O_4 (Alfa Aesar, USA) at 1,000°C in air for 12 hours. Electrodes were then deposited using pulsed laser deposition (PLD) on (001)-oriented, single crystal YSZ (9.5 mol% Y_2O_3-stabilized ZrO_2, Princeton Scientfic, USA). Details of the fabrication technique can be found in references [32, 34]. For this study, a KrF excimer laser at $\lambda = 248$ nm, 10 Hz pulse rate, and ~ 50 mJ pulse energy was used to ablate the targets at 10 mTorr p_{O_2} and 680°C.

Working electrodes consisted of a thin ($\sim$ 5 nm) layer of $Gd_{0.2}Ce_{0.8}O_2$ (GDC) PLD-deposited on the YSZ substrate, followed by an electrode layer of either LSC-64 or LSC-82, at various thicknesses. The GDC layer was used to prevent interfacial reactions between the LSC electrode and YSZ electrolyte materials. Counter electrodes were made by painting Pt ink on the unpolished side of YSZ electrolyte, which was then sintered at 800°C, prior to PLD of the electrode film. After film deposition, Ag ink was used to adhere the completed cell to a larger substrate (prior to electrochemical testing), yielding a large porous Pt/Ag

counter electrode.

A microelectrode pattern (see Figure 2.2b) was created by photo-lithography using a OCG positive photoresist (Arch Chemical Co, USA) on the film surface and patterning with a mask aligner (Karl SÃijss, Germany, $\lambda = 365$nm). After developing the photoresist (Developer 934 1 1, Arch Chemical Co., USA), the films were etched in hydrochloric acid to form circular microelectrodes. Acetone was used to remove the photoresist. The microelectrodes studied were 200 μm in diameter.

2.2.2 Measurement Apparatus

Figure 2.2 is an illustration of the microelectrode testing setup (a modified microprobe station) and sample. Tips for making electrical connections with microelectrodes were platinum coated tungsten and made contact by pressing into sample with the spring force of needle holders. The sample was placed inside an open ceramic heater within a closed end cylindrical shaped holder and the entire setup was partially sealed by placing overlapping glass slides on the open end of the holder. The glass slides were used to allow independent adjustment of each tip. An overhead optical microscope was used to ensure the correct placement of electrical contacts. Oxygen partial pressures were varied by using different blends of argon and oxygen (Praxair) with an active flow over the cell. Platinum coated sample contacts were connected to a dielectric interface (Solartron 1296) and frequency response analyzer (Solartron 1260) or an electrochemical interface (Solartron 1287) and a high speed digitizer (National Instruments 5122), which were used to make linear EIS or NLEIS measurements, respectively.

2.2.3 Electrochemical Measurements

Linear EIS and NLEIS measurements were collected for the flowing temperatures: 450, 520, 580, 640, and 700°C, and oxygen partial pressures: 0.01 atm, 0.1 atm, and 1.0 atm. Due to testing limitations only a limited subset of the conditions were obtained for each

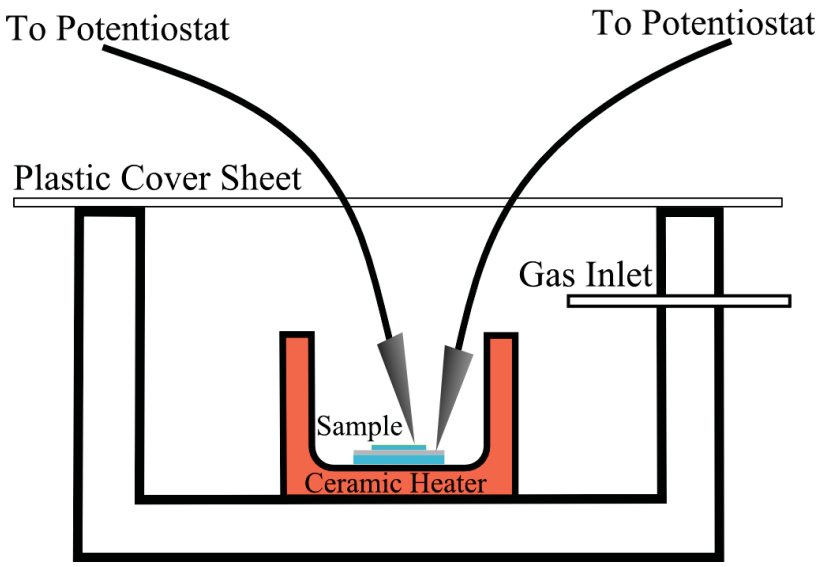

(a) Cross section view of measurment apparatus. Sizes are not to scale.

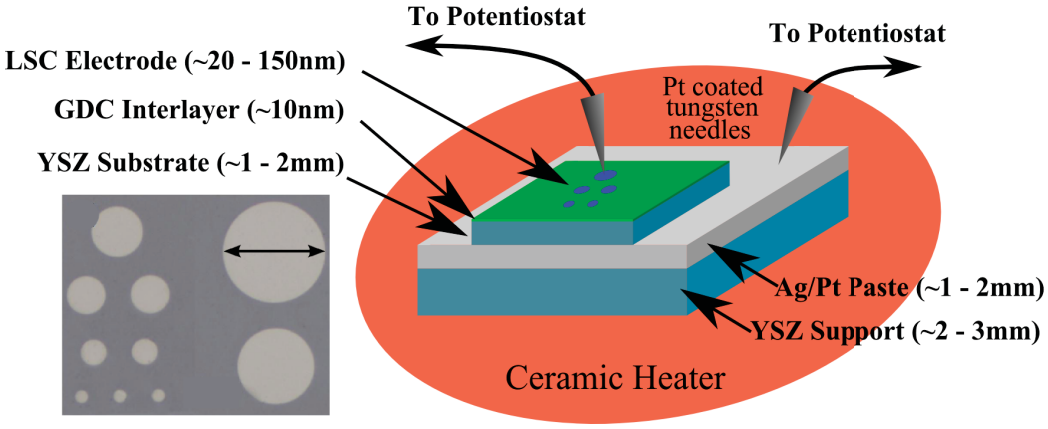

(b) Close up of microelectrode thin film LSC sample.

Figure 2.2: Microelectrode experimental apparatus and sample.

Compositions	Thickness (nm)	T (°C)	P_{O_2} (atm)
$La_{0.8}Sr_{0.2}CoO_{3-\delta}$	34, 56, 90	520, 580, 640	0.01, 0.1, 1
$La_{0.6}Sr_{0.4}CoO_{3-\delta}$	28, 48, 77	580, 640	0.01, 0.1, 1

Table 2.2: List of compositions, film thicknesses, and experimental conditions tested for linear EIS measurments. A few combinations of composition, thickness, and experimental conditions are missing due to restrictions in experimental setups and stability of electrode films. Additionally, a few data sets were collected outside of the given ranges.

electrode material. Tables 2.2 and 2.3 outline the conditions where completed data sets were recorded for linear EIS and NLIES measurements, respectively. At a given testing condition, EIS was performed on several microelectrodes in an array (of the same electrode diameter), using a frequency response analyzer (Solartron 1260, USA) and a dielectric interface (Solartron 1296, USA). Two electrodes with a representative response were chosen for continued testing, with one electrode tested using EIS only, and the other electrode tested with a combination of EIS and NLEIS. NLEIS measurements were performed with a waveform generator (National Instruments PCI-5412, USA), high speed digitizer (National Instruments PCI-5122), and an electrochemical interface (Solartron 1287, USA). Both EIS and NLEIS measurements were obtained over an input frequency range of 0.01 Hz to 10 kHz, with EIS using 10 frequencies per decade and a single perturbation amplitude at each frequency and NLEIS using 5-10 frequencies per decade and 10-20 amplitudes per frequency (values used depended on the non-stationary behavior and characteristic time constant). Details of the NLEIS measurement technique are covered in Section 1.6.2 and elsewhere [5, 49, 51]. To account for any system drift occurring with a single NLEIS measurement time-frame, the higher harmonic spectra were normalized using a point to point normalization, as discussed in Sections 1.6.2.1 and 2.3.2.

Compositions	Thickness (nm)	T (°C)	P_{O_2} (atm)
$La_{0.8}Sr_{0.2}CoO_{3-\delta}$	34, 90	580, 640	0.01, 0.1, 1
	56	640	0.01, 0.1, 1
$La_{0.6}Sr_{0.4}CoO_{3-\delta}$	28	580, 640	0.01, 0.1, 1
	48	640	0.01, 0.1, 1
	77	640	0.1, 1

Table 2.3: List of compositions, film thicknesses, and experimental conditions tested for NLEIS measurments. A few combinations of composition, thickness, and experimental conditions are missing due to restrictions in experimental setups and stability of electrode films. Additionally, a few data sets were collected outside of the given ranges.

2.3 Experimental Characterization and Modeling Results

2.3.1 Film Characterization

Material characterization of the films studied was performed by Ethan Crumlin, Eva Muratoro, Dangkyu Lee, Chris Carlton, Yang Shao-Horn, and co workers at the Massachusetts Institute of Technology. Additionally, SIMS characterization of the films studied previously was performed by Kilner and Chater at Imperial College. Details of the analysis techniques can be found in References [13, 15, 29, 32].

Characterization work on highly oriented crystalline thin films created under conditions similar to those studied here show several key characteristics. Rutherford back scattering (RBS), performed on samples prior to microelectrode patterning, indicates that the average composition of both LSC-82 and LSC-64 films are close to their nominal stoichiometry. Auger electron spectroscopy (AES) was also used to measure near surface compositions ($\sim$5 nm depth), for both LSC-82 and LSC-64 films. Compositional values from RBS and AES measurements, for LSC-82 films studied by Kreller *et al.*, are given in Table 2.4. RBS

	Nominal Composition	Bulk (RBS)	Surface (AES)
La	16	15	14.99
Sr	4	3.5	8.78
Co	20	17.5	21.87
O	60	64	54.35

Table 2.4: Atomic composition of LSC-82 films determined by RBS (bulk) and AES (surface).

results indicate bulk compositional values near the composition of the deposited material, while AES indicates an enhancement of Sr doping near the surface.

In addition to the LSC-82 results, a more in-depth AES study was performed on LSC-64 films for both as-deposited films and films annealed at 550°C for 6 hours in air. The annealed films showed significant surface roughening and possible precipitation of secondary phases (seen as light areas in Figure 2.3). At this time it is not known whether the surface particles represent a new phase or remain perovskites with altered compositions. Area averaged atomic compositions were obtained for both the pristine and annealed films. In addition, for the annealed films spot AES measurements were taken for both the nominal film surface (dark areas marked by x's 3 and 4) and on surface particles (light areas marked by x's 1 and 2). The values for atomic composition calculated from AES measurements are given in Table 2.5.

Values for the pristine LSC-64 films show a close to nominal ratio of the A-site cations (La/Sr $\approx$ 3/2), but a significant depletion of the B-site cation (Co). The annealed films show a slight depletion of Sr on the film surface, but a significant enhancement of Sr in the surface particles ($\sim$25%) as well as a similar depletion in the B-site cation. At this point, it is unclear whether the depletion of the B-site cation seen in the LSC-64 results, or

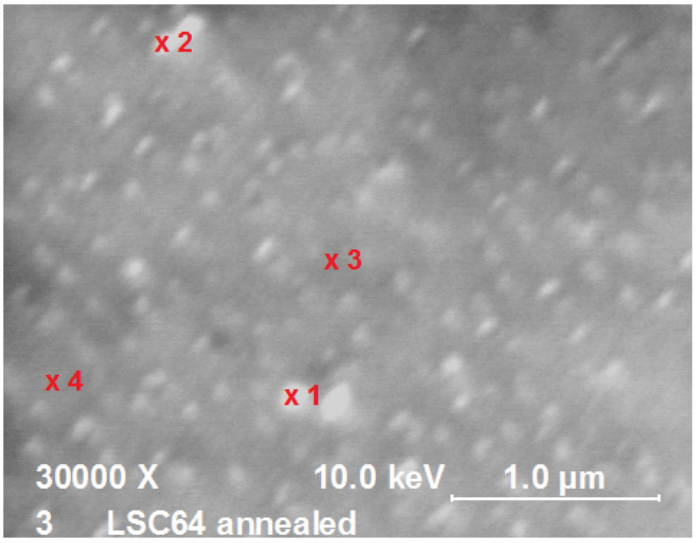

Figure 2.3: Scanning electron microscope (SEM) image of LSC-64 surface after annealing for 6 hours, at 550°C in air. Numbers indicate locations for spot AES measurments.

	Nominal Composition	Pristine Film (Area)	Annealed Film (Area)	Annealed Film Normal Surface	Annealed Film Surface Particle
La	12	25.89	30.80	30.98	25.29
Sr	8	18.02	16.53	16.63	25.64
Co	20	7.16	6.17	7.11	6.04
O	60	48.92	46.49	45.28	43.01

Table 2.5: Surface atomic composition of LSC-64 films determined by AES for as-deposited films and annealed films (6 hours at 550°C in air). Area averaged compositions were obtained for both pristine and annealed films; in addition, annealed films were spot measured in locations corresponding to nominal surface and in the presence of a surface particle.

the enhancement of the B-site cation seen in the LSC-82 results, is an artifact of the semi-quantitative calculations for atomic composition from AES intensity measurements or a real departure from the nominal composition. It is, however, clear that the ratio of La to Sr cations in the LSC-64 films increases significantly upon annealing, with a corresponding formation of surface particles that exhibit a reduced ratio. These results indicate that Sr is generally depleted on the surface of annealed LSC-64 films (compared to pristine), while surface particles that form exhibit an enhancement in Sr content, leading to significant lateral (parallel to surface) deviations in Sr composition.

To establish the crystallinity of the films, X-Ray Diffraction (XRD), in both normal and off-normal configurations, was used. Because of the oriented crystalline nature of the films, the rotation of the sample in the off-normal configuration is only expected to show peaks at rotation angles that align with the crystal structure. Example spectra are shown in Figure 2.4. Results from XRD indicate that the films contain only a single phase and are highly oriented. Additionally, the [001] LSC phase appears to be rotated 45° with respect to [001] GDC and [001] YSZ and exhibits slightly non cubic lattice parameters (corresponding to <1% tensile strain).

Depth profile SIMS analysis was used to qualify non-uniformity of A-site cation concentrations with LSC-82 films studied previously (Figure 2.5). The results indicate a Sr enrichment in the near surface region ($\sim$10 - 20 nm). The Sr profile within the films appears exponential near the surface, quickly approaching a plateau. Depth of the profile differed between two samples of different thickness, with the larger sample exhibiting a larger decay length. While the recorded intensity of a SIMS measurement is not strictly analytical, if the plateau region is assumed to correspond to the nominal Sr composition, the percent change in the Sr to La ratio was $\sim$25% for both samples.

Crumlin *et al.* have also investigated segregation of Sr within similarly deposited films, as well as porous electrodes of similar composition, using ambient pressure x-ray photoelectron spectroscopy (APXPS) and x-ray diffraction (XRD) [14]. XRD results indicate that both the thin films and the porous film electrodes contained secondary (non perovskite)

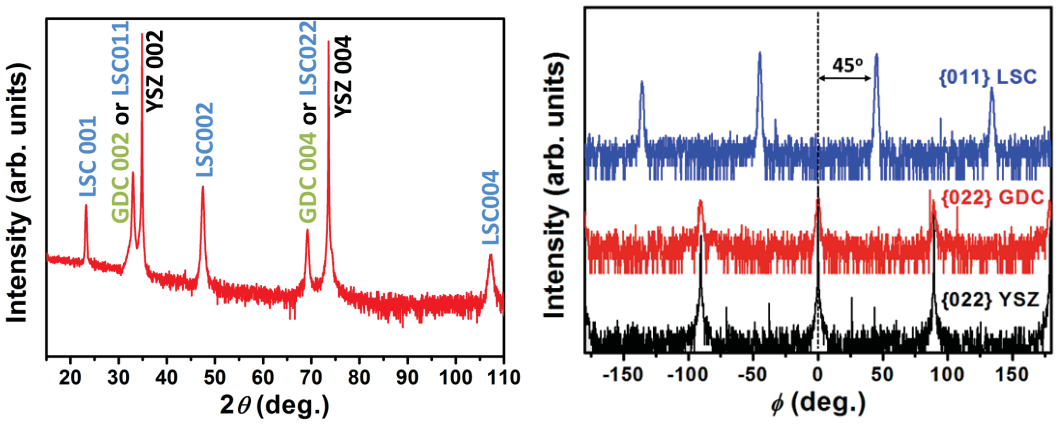

(a) Normal configuration

(b) Off-normal configuration (ϕ = rotation)

Figure 2.4: XRD results for LSC-82 thin films on YSZ substrate with a small GDC protection layer.

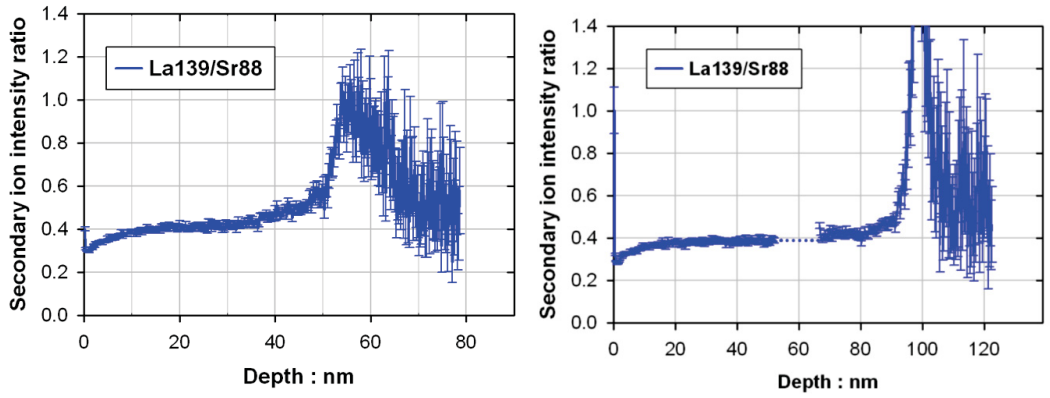

(a) 45 nm film

(b) 90 nm film

Figure 2.5: Depth profile SIMS results for LSC-82 thin films with a thickness of 45 nm (a) and 90 nm (b). Values indicate the composition ratio of A-site cations (La/Sr) as a function of depth.

LSC-82* (nm)	LSC-82 (nm)	LSC-64 (nm)
45	34	28
90	56	48
	90	77

Table 2.6: AFM measured thickness for LSC-82 and LSC-64 films. LSC-82* are previously studied films.

phases on the surface, with the porous film having a much larger coverage. APXPS indicated that, at low temperatures ($< 250^{\circ}$C), there was no measurable enhancement of Sr concentration in either film. However, upon heating to $\sim$520°C the thin films exhibited a strong surface peak for the Sr 3d orbital. Fitting of the obtained spectra revealed that much of the surface Sr enhancement occurred within the perovskite lattice rather than as a precipitation of a secondary Sr rich phase on the surface.

Finally, surface roughness and film thickness were determined by Atomic Force Microscopy (AFM) at the edge of a microelectrode. For all films, the surface roughness prior to electrochemical testing was found to be less than 2 nm. Film thicknesses are reported in Table 2.6.

2.3.2 Nonstationary Behavior

Both LSC-64 and LSC-82 films were found to exhibit significant nonstationary behavior in the electrochemical response. The timescale of the nonstationary behavior was such that, within a single EIS measurement, no observable deviation from the expected semi-circular response was seen (Figure 2.9), but significant changes in extracted characteristic parameters were seen over longer time periods. Figure 2.6 illustrates the changes in characteristic values of the impedance (VSC and R_{chem}) as a function of time and over a range of ex-

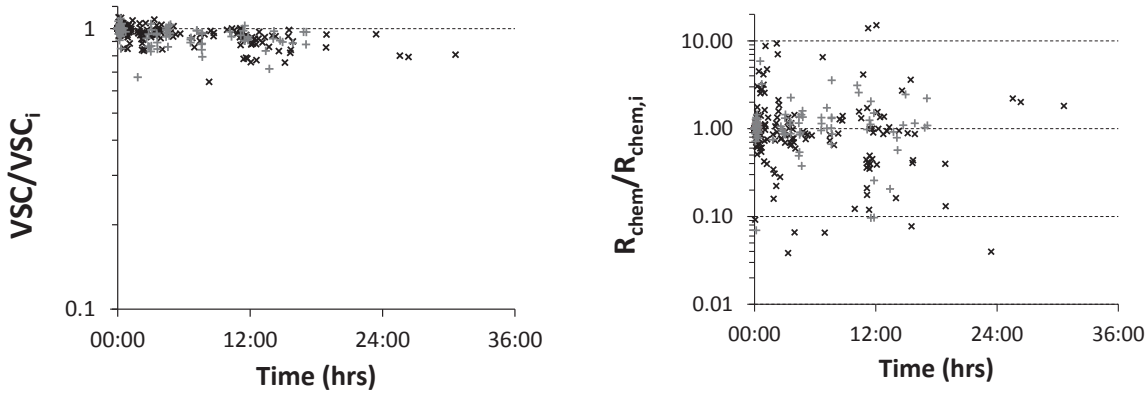

(a) VSC

(b) R_{chem}

Figure 2.6: Relative changes in the values of characteristic parameters R_{chem} and VSC over time, for LSC-82 films (gray +'s) and LSC-64 films (black x's), across all measured conditions. Relative changes are calculated by deviding by the intial value taken at the begining of measurements at a single set of experimental conditions.

perimental conditions. All nonstationary behavior observed vs. time was tracked within a single experimental condition (changing conditions are represented by additional data sets starting at $t = 0$).

R_{chem} is seen to both increase and decrease with time, over a relatively short time period (< 12 hrs). Decreases in magnitude range from 10-100%, while increases in magnitude range from 10-400%. Although extensive long term studies were not conducted, there does not appear to be any correlation in direction or magnitude of changes in R_{chem} with the experimental conditions, composition of the electrode, or thickness of the film. The exception to this observation is that extended testing at high temperatures ($> 650^{\circ}$C) universally led to increases in R_{chem} of several orders of magnitude (data not shown).

In contrast to the changes seen in R_{chem}, changes in VSC were relatively small, with the most common effect being a decrease of less than 20%, over similar timescales. Examining

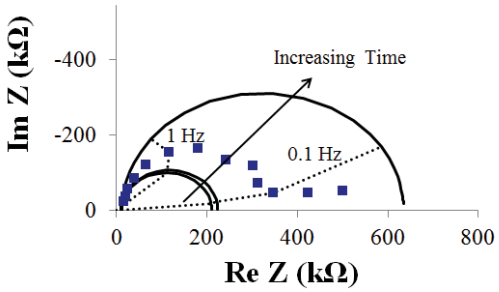

(a) NLEIS (data points) and EIS (solid lines) impedance spectra on a LSC-82, 90 nm film, at 520°C and 1 atm p_{O_2}.

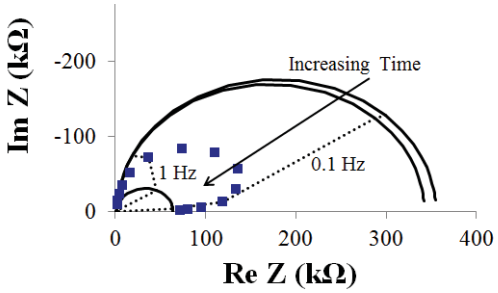

(b) NLEIS (data points) and EIS (solid lines) impedance spectra on a LSC-64, 48 nm film, at 640°C and 0.1 atm p_{O_2}.

Figure 2.7: Impedance spectra collected over 10 and 11 hours on an LSC-64 and LSC-82 films, respectively. Points indicate impedance measured by NLEIS, while solid lines indicate impedance measured by EIS. EIS measurements lasted ∼30 minutes, while NLEIS measurements lasted ∼9-10 hrs. Arrows indicate progression of time.

the relationships in Equations (2.14) and (2.12) suggests that changes in the surface rate coefficient $k(T)$ are more pronounced than changes in the thermodynamic properties of the film over short timescales ($<$ 36 hrs).

While the timescale of the nonstationary behavior was such that single linear EIS measurements could be taken successfully without any indication of drift, NLEIS experiments, which occur over a longer timescale, are subject to nonstationary behavior. Examples of nonstationary effects seen in an NLEIS measurement are illustrated in Figure 2.7. In general EIS experiments were on the order of ∼30 minutes, while NLEIS experiments could range from 2-12 hours depending on the characteristic time constant of the electrode. Both EIS and NLEIS measurements are parametric in frequency, and it can be seen that at high frequencies (data points that are closer to the origin), impedance spectra from both measurements predict semi-circular behavior, while at low frequencies NLEIS measurements devi-

ate significantly. High frequency points are collected on a similar timescale between EIS and NLEIS measurements, but low frequency points take significantly longer for NLEIS due to the multiple amplitudes needed and signal acquisition techniques. The observed drift is not attributed to effects caused by EIS or NLEIS measurements, as similar drift was observed in cells measured only infrequently with EIS and not at all with NLEIS. The behaviors indicated in Figure 2.7 are opposite for the two films, where the LSC-64 film improved with time, while the LSC-82 film degraded. These trends were not consistent, and films of both compositions exhibited both trends, with no apparent correlation to an environmental conditions.

Because the timescale of NLEIS measurements is on the order of the timescale for significant variations in R_{chem}, the method for determination of the 2nd and 3rd order harmonics must be adjusted. So long as the nonstationary effects are limited within the timeframe of a single frequency measurement, a point to point type normalization can be used to adjust for system instability, as described in section 1.6.2.1. Figure 2.8 shows 2^{nd} and 3^{rd} harmonic spectra collected sequentially, on LSC-64, in the same environment, and normalized using the point to point technique. The relative stability of the harmonics over time gives validity to the point-to-point scaling method as well as the previous finding of drift being primarily driven by changes in surface rate coefficients (which are not expected to affect nonlinear behavior).

2.3.3 Linear Results

EIS measurements were obtained across a range of environmental conditions, for two different material compositions (LSC-82 and LSC-64), and for several different film thicknesses. Table 2.2 provides the set of experimental conditions tested with linear EIS for the different films. Representative impedance spectra are shown in Figure 2.9 for LSC-82 and LSC-64 films, as a function of p_{O_2}, at 640°C. Within individual spectra there is a single dominant feature at low frequencies (a semi-circular arc), that increases in magnitude with decreasing p_{O_2}, consistent with an impedance dominated by kinetics of the surface

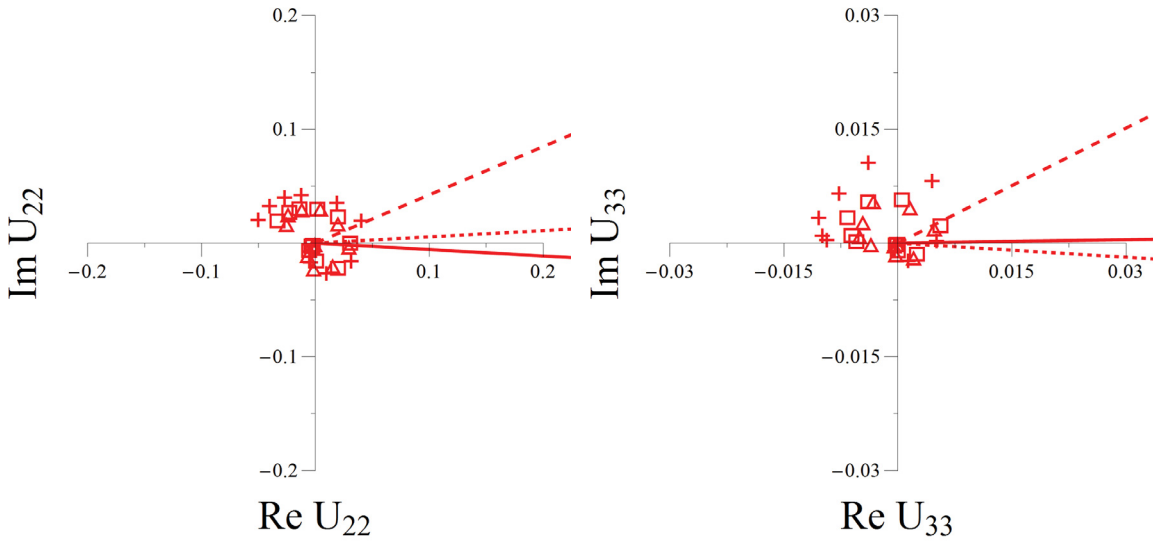

(a) 2nd harmonic spectra

(b) 3rd harmonic spectra

Figure 2.8: Sequential 2nd and 3rd harmonic spectra, collected on a 48 nm, LSC-64 film, at 640°C and 1 atm p_{O_2}.

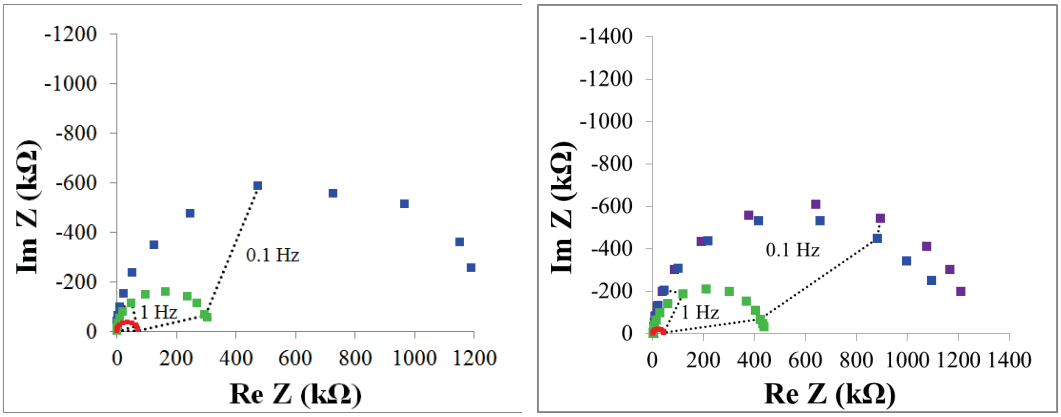

(a) LSC-82 90 nm film, at 640°C, in 1 atm O_2 (Red Squares), 0.1 atm O_2 (Green Squares), and 0.01 atm O_2 (Blue Squares).

(b) LSC-64 28 nm film, at 640°C, in 1 atm O_2 (Red Squares), 0.1 atm O_2 (Green Squares), 0.01 atm O_2 (Blue Squares), and 0.001 atm O_2 (Purple Squares).

Figure 2.9: Example impedance spectra for LSC-82 and LSC-64 thin films, at 640°, and various p_{O_2}.

exchange reaction and modeled by the RC circuit given in Equation (2.11).

Average VSCs are plotted as a function of p_{O_2} for LSC-82 films at 520°C, 580°C, and 640°C (Figure 2.10), and LSC-64 films at 580°C, and 640°C (Figure 2.11). Figure 2.10 includes additional data from a previous publication on similarly made films for comparison [29]. Along with measured values, predicted values are also given for freestanding bulk LSC-82 and freestanding bulk LSC-64, calculated assuming a uniform material composition equal to the nominal composition of the deposited electrode material (dashed lines).

VSCs for all electrodes measured are shown to increase with decreasing p_{O_2}. However, LSC-82 and LSC-64 films exhibit different behavior compared to expected freestanding bulk values. LSC-82 values exhibit a weaker p_{O_2} dependence and an increase in magnitude (ranging from a ≈2X to ≈2 orders of magnitude) compared to freestanding bulk values,

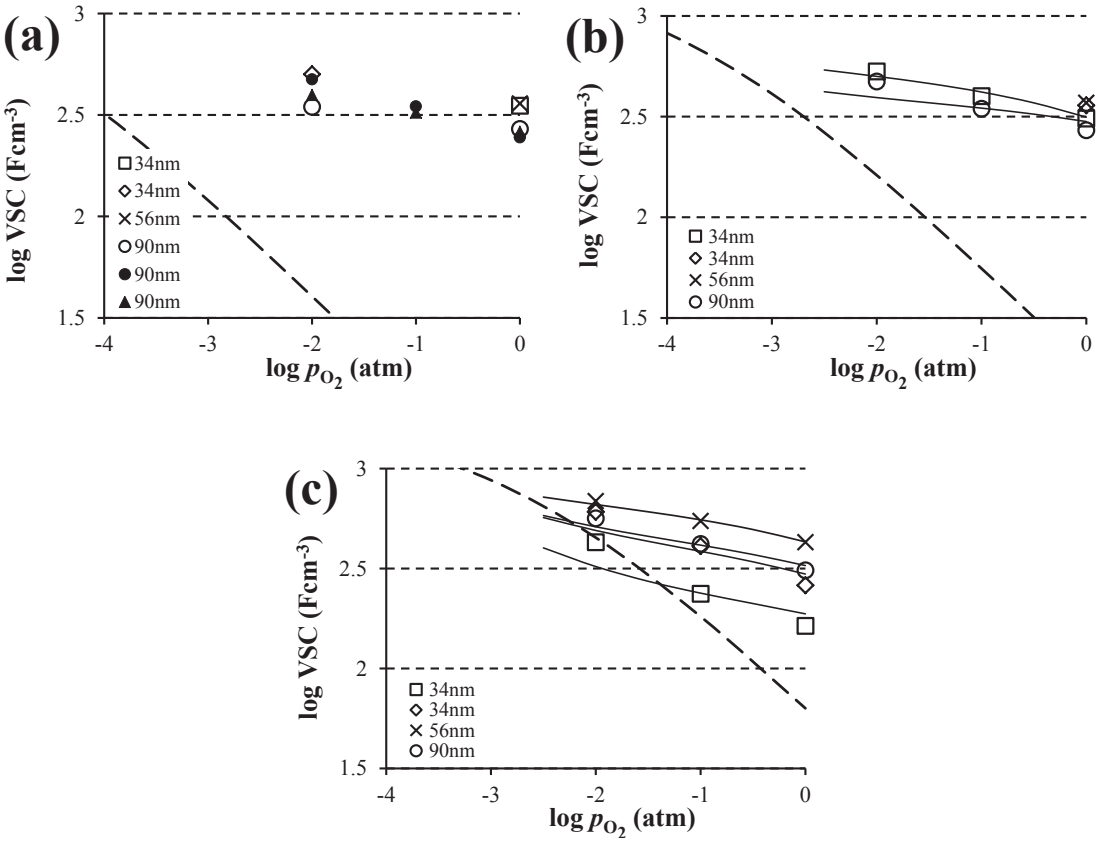

Figure 2.10: Volume specific capacitances for LSC-82 films of varying thicknesses, plotted as a function of p_{O_2}, at 520°C (a), 580°C (b), and 640°C (c). Data points were obtained from equivalent circuit fitting of experimental data. Open markers represent data collected in this study, while closed markers represent data collected in an earlier published study [29]. Gray color indicates a repeated test on the same cell at the same conditions after additional testing at other conditions. Dashed lines are predicted values for freestanding LSC-82 bulk material using the generalized thermodynamic model from section 1.3.2 , and solid lines are predicted values for the mixed bulk model outlined in section 2.1.3

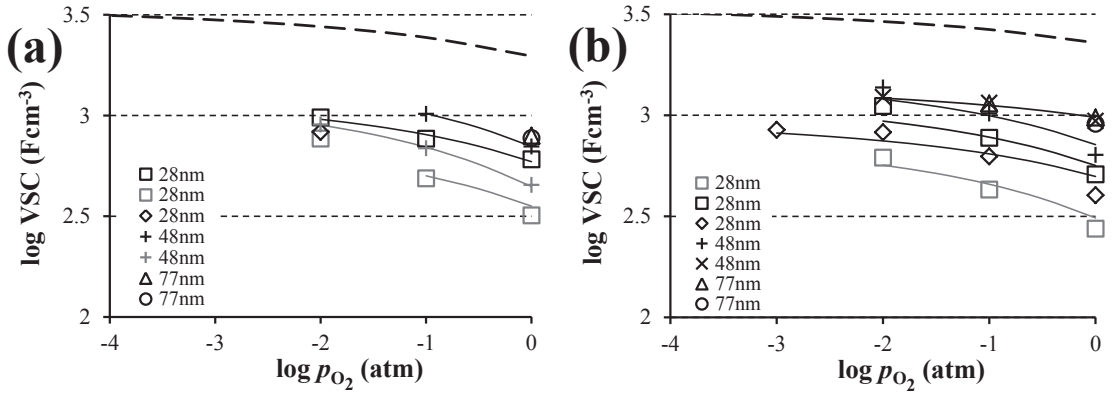

Figure 2.11: Volume specific capacitances for LSC-64 films of varying thicknesses, plotted as a function of p_{O_2}, at 580°C (a) and 640°C (b). Data points were obtained from equivalent circuit fitting of experimental data. Gray color indicates a repeated test on the same cell at the same conditions after additional testing at other conditions. Dashed lines are predicted values for freestanding LSC-64 bulk material using the generalized thermodynamic model from section 1.3.2 , and solid lines are predicted values for the mixed bulk model outlined in section 2.1.3

with the largest offsets occurring under oxidizing conditions of low temperature and high p_{O_2}. In contrast, LSC-64 thin films exhibit a similar p_{O_2} dependence to the predicted freestanding bulk values, but a ≈3-6X smaller magnitude.

It can also be seen in Figures 2.10 and 2.11, that VSCs for both LSC-82 and LSC-64 films show a moderate dependence on film thickness, although the trend is not constant across all conditions. LSC-82 films exhibit decreased VSC with increasing thickness at 520°C and 580°C, but have no consistent trend at 640°C. LSC-64 films always show an increasing VSC with increasing thickness. There are also variations between identically made films of the same thickness and between the same cells tested at different times (with different testing histories) that are of roughly the same size as the variations seen between thicknesses. Because the capacitances are already normalized to the differing volume of the films, the VSCs are expected to be independent of film thickness. A thickness dependent relationship suggests that the active volume of the electrode films differs from the total volume, and cell to cell variability suggests that the active volume is cell history dependent.

Finally, predicted values of VSC were calculated using the mixed bulk electrode model and generalized thermodynamic mode, with compositions obtained through least squares regression (see Appendix A.2) of the mixed surface/mixed bulk model (solid lines). Because surface compositions are assumed to negligibly affect the total concentration of Sr within the film, fitting of the VSC involves only the three bulk compositional parameters (x_{b1}, x_{b2}, λ_1). Parameters are assumed to be independent of oxygen partial pressure (p_{O_2}), but are allowed to change with temperature. Changes with respect to temperature are not necessarily attributed to the changing conditions, but are necessary to accommodate the larger nonstationary behavior across the longer time frame of experiments measured at different temperatures. Bulk compositional parameters are also subject to the additional constraint that the average Sr dopant level within the film cannot exceed the level of the original deposition material. Having only an upper bound allows for the adjustment to Sr lost to precipitation of a secondary, inactive phase. It should also be noted that while fitting of the VSC was the primary method for determining the values of the bulk compositional

parameters, small changes ($< 5\%$) were allowed for improved nonlinear fits (further details in section 2.3.4).

The mixed bulk model shows good agreement with both the magnitude and p_{O_2} dependence of measured VSCs for both LSC-82 and LSC-64 films. Values for the model parameters are illustrated in Figure 2.12. LSC-82 films were found to consist of a small amount ($< 20\%$ of total volume) of a much higher doped ($0.39 < x < 0.46$) material, while the remaining bulk was decreased ($0.16 < x < 0.18$), maintaining an average bulk composition very close to the original composition of the film ($x \approx 0.2$). The higher doped material dominates the capacitance in the most oxidizing conditions (high p_{O_2} and low T), while both materials contribute to the overall capacitance at more reducing conditions. In contrast, LSC-64 films were found to consist of a moderate ($\sim$20-40% of total volume) amount of material that was close to the nominal composition of the deposited material ($0.35 < x < 0.43$), while the rest of the material was inactive and did not contribute to the total capacitance. This inactive region manifested itself as low fit values for the bulk compositional variable x_{b1}, which could be set to 0 with no change in predicted results. This does not necessarily indicate large amounts of Sr precipitation, rather, that bulk region 1 of the electrode was inactive and did not contribute capacitive behavior to the overall electrode response. Setting the composition to a value of 0 is the simplest way to represent an inactive volume for the mixed bulk model as the continuous thermodynamic equations predict a negligible capacitive response at that composition. For both film compositions, fit values were found to contain some variability between film thicknesses and the measurement temperature, but there were no consistent trends.

2.3.4 NLEIS Results

NLEIS measurements were also obtained across a range of environmental conditions, for two different material compositions (LSC-82 and LSC-64), and for several different film thicknesses. Table 2.3 provides the set of experimental conditions tested for different films. The films and conditions tested for NLEIS were a subset of those tested for linear EIS, as

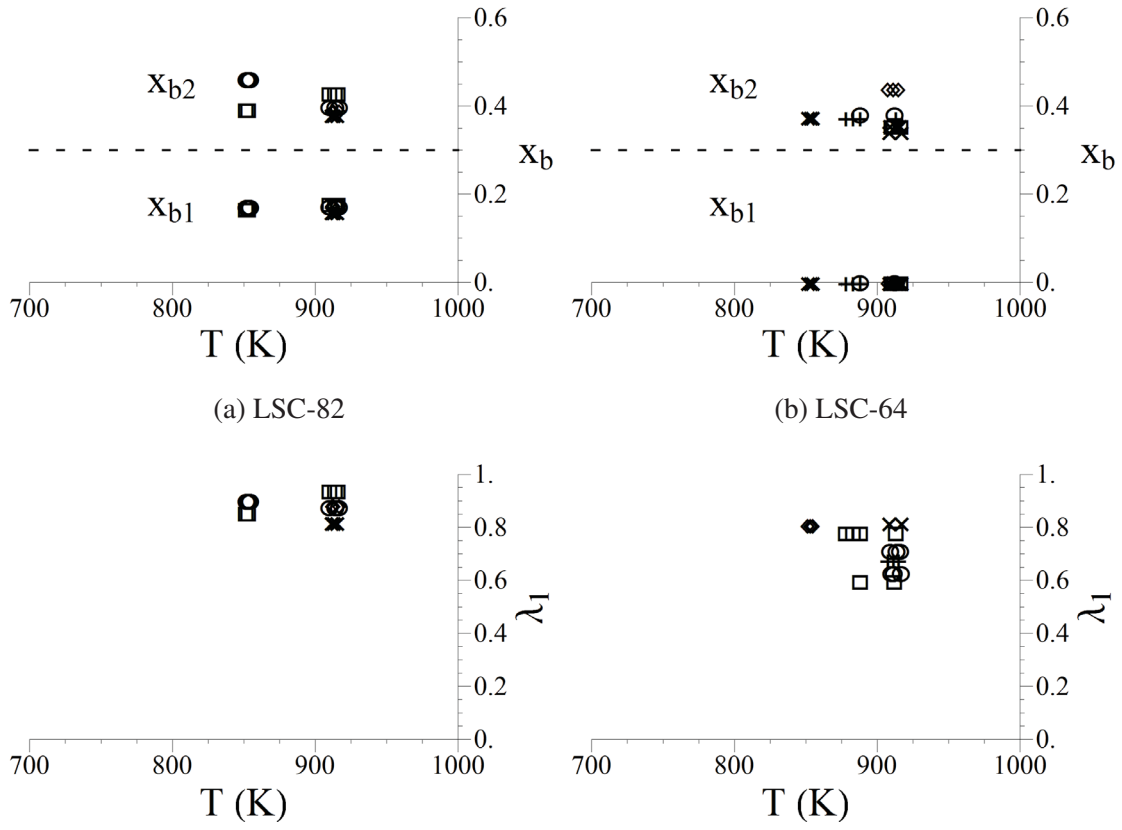

(a) LSC-82

(b) LSC-64

(c) LSC-82

(d) LSC-64

Figure 2.12: Best fit, bulk compositional values, for a mixed bulk model of LSC-82 (a and c) and LSC-64 (b and d) films. λ_1 represents the fractional volume of bulk region 1 (with a composition x_{b1}) with the remaining volume being bulk region 2 (with a composition x_{b2}). Values are obtained at several temperatures and film thicknesses.

the longer timescale of NLEIS experiments, coupled with large nonstationary behavior of the electrodes, makes testing electrodes with a significant portion of the response at lower frequencies (< 0.1 Hz) impossible.

The effect of film thickness on harmonic spectra is illustrated in Figure 2.13 for both LSC-82 and LSC-64 films. Each graph plots the 2^{nd} and 3^{rd} order harmonic spectra for films of the same composition and at the same testing conditions, but with different film thicknesses (and most likely different testing histories). While the harmoics of the LSC-82 films appear similar (Figure 2.13a), LSC-64 films show larger variations among film thicknesses (Figure 2.13b). It's unclear if the larger variations are due to thickness-mitigated driving forces for altered thermodynamic behavior, or if they merely represent variations in testing history. The variation with film thicknesses was found to be on the order of the variation from cell to cell, which is similar to what was seen in the linear capacitive results.

Figures 2.14 and 2.15 illustrate representative 2nd and 3rd harmonic spectra for LSC-82 and LSC-64 films, with best fit model predictions for a mixed surface/mixed bulk model (solid curves). Nyquist plots are used which are parametric in frequency (ω) and follow the general trend of spiraling outwards from the origin as frequency decreases. Phasor lines are used to indicate frequency for both the measured data (dashed lines) and the model (solid lines). 2nd harmonic phasor lines intercept the data (or model) where $\omega = \omega_{chem}/2$, and the 3rd harmonic phasor lines intercept where $\omega = \omega_{chem}/3$. For measured data, linear interpolation between the two nearest frequencies is used to approximate the phasor line interception point. The higher order harmonics for both films are similar despite having different compositions and different predicted thermodynamic behavior of freestanding bulk materials.

The 2nd harmonic spectra exhibit a low frequency intercept in the 2nd quadrant that becomes increasingly negative with decreasing p_{O_2}, as well as a counterclockwise rotation of the phasor lines with decreasing p_{O_2}. These trends were consistent across the majority of the collected data set, although an inversion of low frequency intercept trend (with p_{O_2})

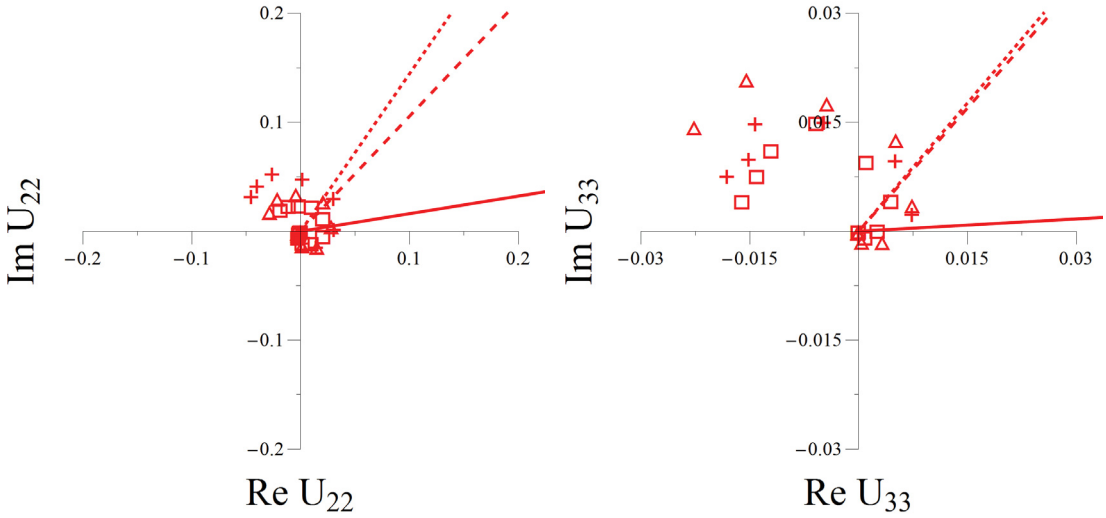

(a) LSC-82

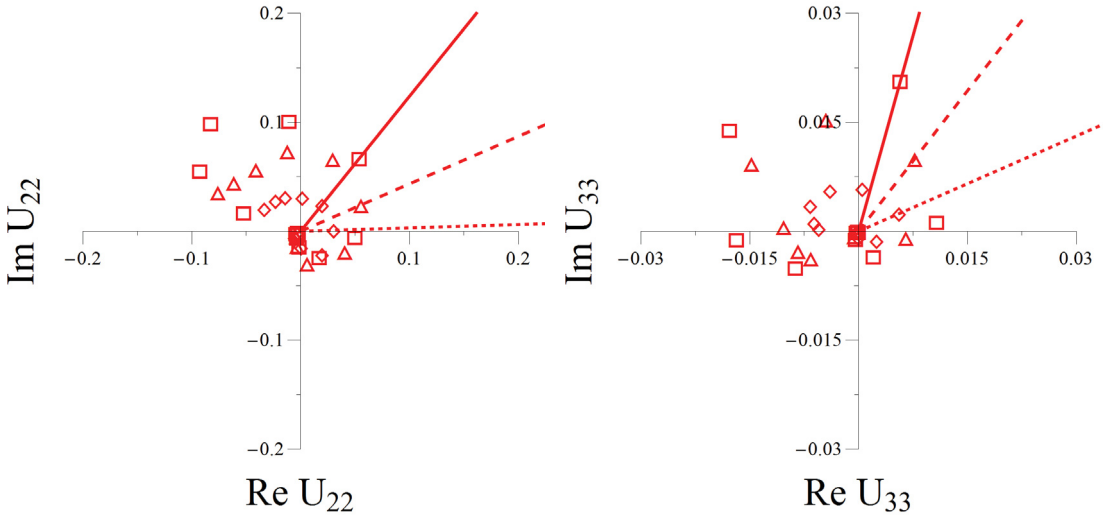

(b) LSC-64

Figure 2.13: Normalized 2nd and 3rd harmonic spectra for LSC-82 and LSC-64 thin films at 640°C and 1.0 atm p_{O_2}. Film thicknesses for LSC-82 films are: 34 nm (Squares), 56 nm (Plus), and 90 nm (Triangles); while thicknesses for LSC-64 films are: 28 nm (Squares), 48 nm (Diamonds), and 77 nm (Triangles).

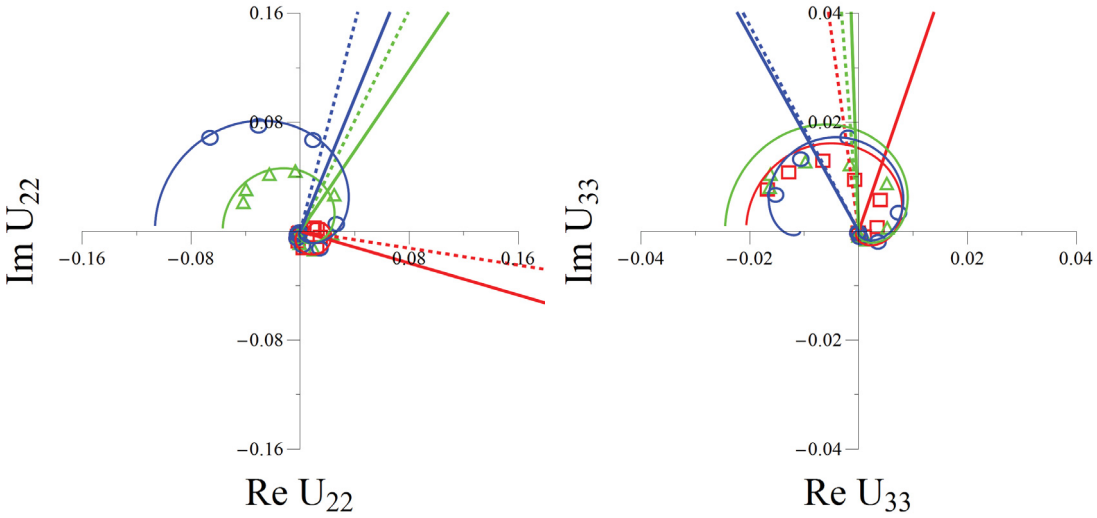

(a) LSC-82, 90 nm, 580°C

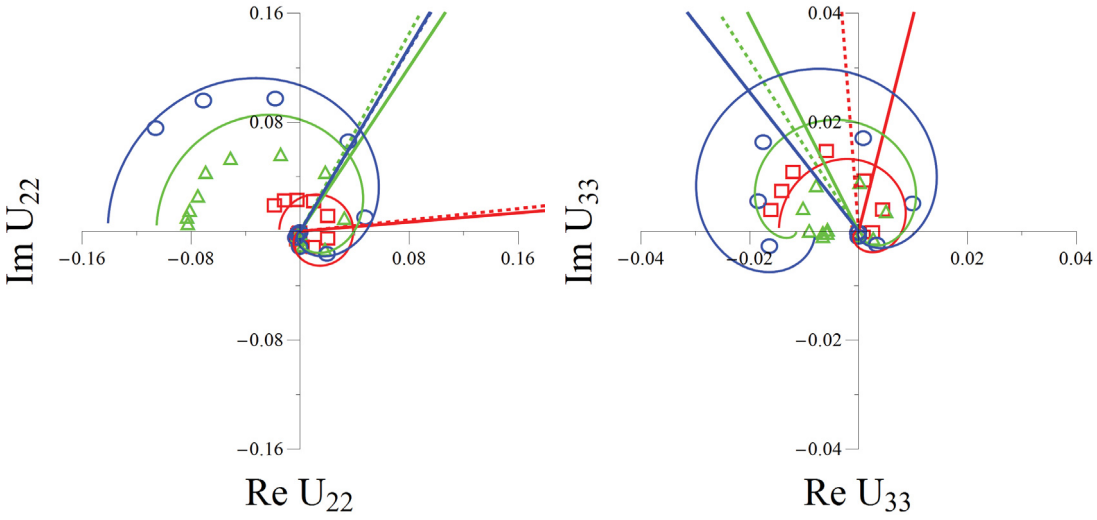

(b) LSC-82, 48nm, 640°C

Figure 2.14: 2nd ($U_{2,2}$) and 3rd ($U_{3,3}$) harmonic spectra for a 90 nm and 34 nm thick LSC-82 film, collected at 580°C and 640°C, and oxygen partial pressures of: 0.01 atm (blue circles), 0.1 atm (green triangles) , and 1 atm (red squares). Data points represent measured harmonics (dashed phasor line) while solid curves indicated best fit model.

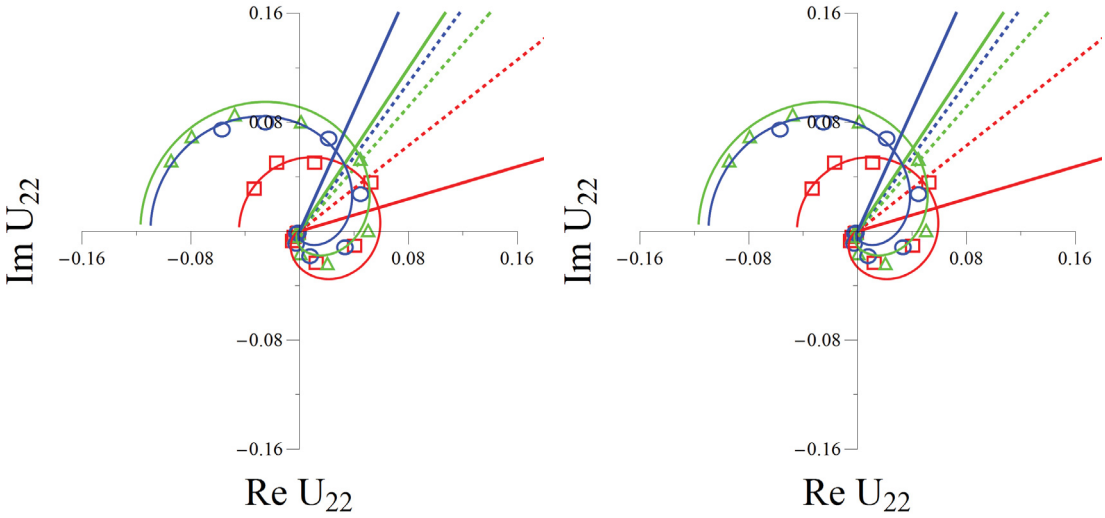

(a) LSC-64, 28 nm, 580°C

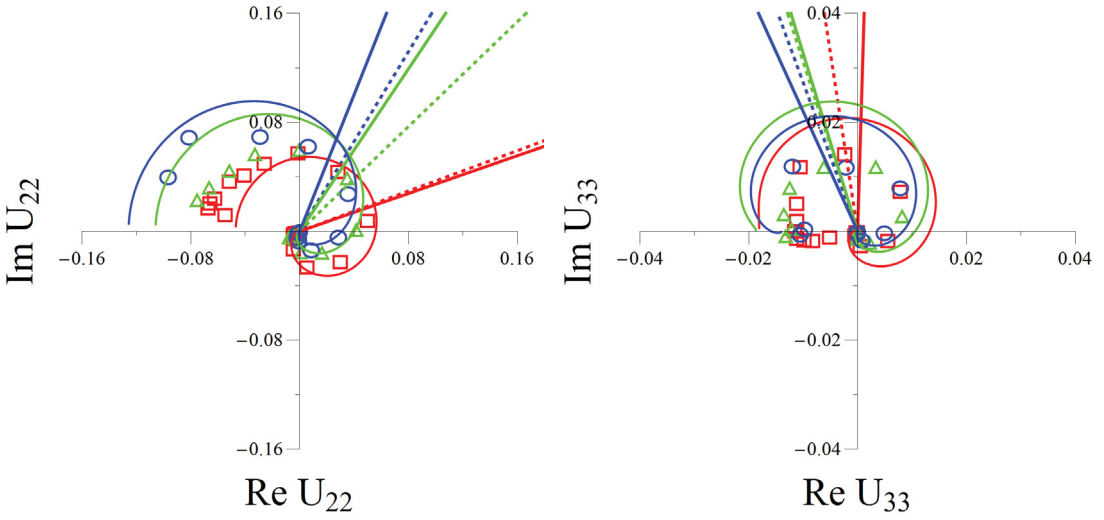

(b) LSC-64, 28nm, 640°C

Figure 2.15: 2nd ($U_{2,2}$) and 3rd ($U_{3,3}$) harmonic spectra for a 28 nm thick LSC-82 film, collected at 580°C (a) and 640°C (b), and oxygen partial pressures of: 0.01 atm (blue circles), 0.1 atm (green triangles) , and 1 atm (red squares). Data points represent measured harmonics (dashed phasor line) while solid curves indicated best fit model.

was seen for two LSC-64 films at 640°C, which corresponds to the two highest compositional parameters (x_{b2}) reported below. The 3rd harmonic also exhibits low frequency intercepts in the 2nd quadrant, but values do not change appreciably (no consistent trend in low frequency intercept) with changing p_{O_2}. 3rd harmonic phasor rotations are similar to the 2nd harmonic for 640° in both LSC-82 and LSC-64 films, but at 580°C the rotation becomes inconsistent with p_{O_2}.

Semi-quantitative agreement can be seen between the measured 2nd and 3nd order harmonics and the mixed surface/mixed bulk model. Importantly, the model captures the weak p_{O_2} dependence (very weak for $U_{3,3}$) of the low frequency intercept of the measured harmonics, as well as accurately predicting the overall magnitude and p_{O_2} trends of the spectra. Of all the Sr redistribution models tested (2 layers, exponential decay from surface, sigmoidal axial distribution) the mixed surface/mixed bulk model was the only one capable of accurately predicting all of these features.

Model predictions for the harmonic spectra represent a best fit of the mixed surface/mixed bulk model using least squares regression (see Appendix A.2). Initial bulk compositional values (x_{b1}, x_{b2}, λ_1) were taken from VSC fits and only allowed to change over a range of $\pm 5\%$ (subject to the same constraints mentioned previously). Surface compositional values (x_{s1}, x_{s2}) were allowed to vary over a range of $0.1 \leq x_{si} \leq 0.7$, which represents the most accurate portion of the continuous phase thermodynamic model, and a very conservative estimate of the likely maximum range of values based on previous and current film analysis. Additionally, as a first approximation, surface rate coefficients for each region are assumed to change in a correlated manner, giving a consant value for the ratio of effective coverages θ. This allows for estimation of the contribution to a weak p_{O_2} dependence arising from the mixed surface, rather than a convolution of a time dependent θ. Values for the bulk compositional values are reported above (Figure 2.12) and surface compositional values are given in Figure 2.16.

LSC-82 films were found to exhibit a slightly elevated ($0.22 < x < 0.3$) amount of Sr doping for a large amount of the active sites on the surface ($\theta \sim 10$), as well as a small

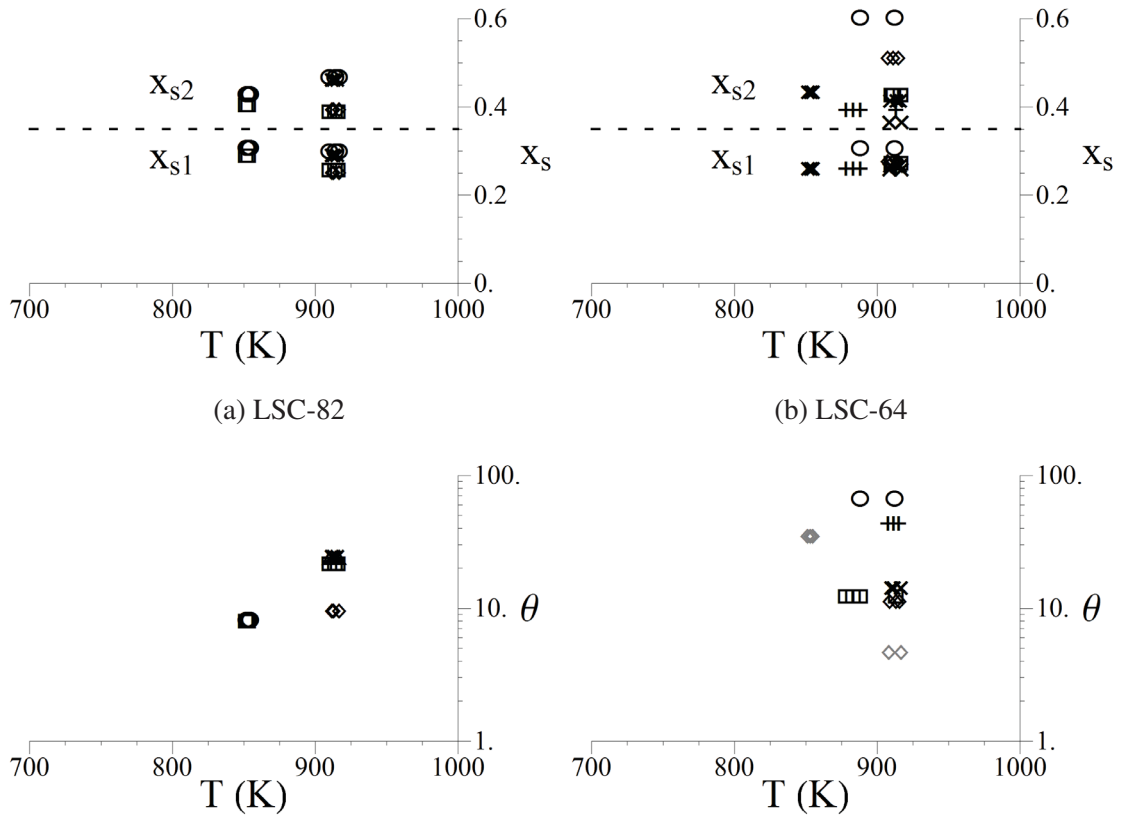

(a) LSC-82

(b) LSC-64

(c) LSC-82

(d) LSC-64

Figure 2.16: Best fit surface compositional values for a mixed surface model of LSC-82 (a and c) and LSC-64 (b and d) films. θ represents the ratio of active site concentrations in surface region 1 (with a composition x_{s1}) to surface region 2 (with a composition x_{s2}). Values were obtained for several temperatures and film thicknesses. Film thickness LSC-82 films are: 34 nm (□/◇), 56 nm (x/+), and 90 nm (△/○); while thicknesses for LSC-64 films are: 28 nm (□/◇), 48 nm (x/+), and 77 nm (△/○)

amount highly doped ($0.39 < x < 0.46$) material. The results for LSC-64 films were very similar to those for LSC-82. Like LSC-82 films, LSC-64 films consisted of a mixed surface with a large amount material ($\theta > 10$) with a lower Sr dopant level ($0.26 < x < 0.3$) and a small amount of a similarly doped ($0.37 < x < 0.44$) material. However, the nominal composition of LSC-64 films is much higher, indicating that the majority of the surface of LSC-64 films is Sr depleted. This at least qualitatively agrees with the results of the pristine and annealed AES study, which also predicted depletion of Sr levels on the majority of the surface of LSC-64 films, except for small regions of enhancement near surface particles. As with bulk compositional values, there was some variation in the obtained surface compositional values, but with no consistent trends.

It should be noted that the previously mentioned range for the highly doped Sr dopant level (x_{s2}) in LSC-64 films excluded two data sets that exhibited a much higher level of bulk Sr content ($x_{b2} = 0.5$ and $x_{b2} = 0.6$). These data sets were unique in that both exhibited inverse trends in the measured harmonics with respect to changing oxygen partial pressure. The $x_{s1} = 0.5$ data set exhibited a higher level ($\sim 22-25\%$ vs $\sim 10-18\%$) of capacitive drift over the time frame of collected data, which could indicate a larger than normal drift in the compositional values. While the $x_{s1} = 0.6$ data set contained harmonics and VSCs at only two oxygen partial pressures, making it harder to ascertain the correct p_{O_2} dependence and possibly leading to best fit compositional values that represent a non-physical local minimization. Addtionally, both data sets represented the high end of non-stationary behavior.

2.4 Discussion

Analysis of LSC-82 and LSC-64 thin films suggests that several important factors contribute to their unique electrochemical responses. The governing rate law for O_2 exchange was found to be consistent across nominal compositions, local compositions, film thickness, and system drift, with dissociative-adsorption being the rate determining step (indicated by inaccuracies of models with alternative rate laws not shown here). Alternatively, the overall

rate of O_2 exchange was affected by both long term changes in the local surface compositions and short term changes in the rate coefficient $k(T)$. Interestingly, modeling fits for both LSC-82 films and LSC-64 films indicated a similar surface Sr composition. Finally, the capacitive response of the films was affected by long term changes in bulk composition (for LSC-82 films) and large scale film deactivation (for LSC-64 films). The exact cause of the observed changes remains somewhat unclear.

The changes observed between the thin films studied and freestanding bulk material of the same composition were primarily explained with Sr redistribution and bulk deactivation. For LSC-82 films only Sr redistribution was invoked, with an exclusion of Sr toward the surface and further exclusion of Sr towards a likely precipitation point. High Sr regions dominate the electrochemical response in more oxidizing conditions (low T and high p_{O_2}) and the larger low Sr regions become important in increasingly reducing environments. While the 4 composition model used is an oversimplification of actual compositional distributions, the diffusionally equilibrated nature of the films made explicit spatially resolved compositions indistinguishable from averaged behavior within the limits of cell to cell variability. These results are in agreement with previous studies that have reported increased surface concentration of the A-site cation dopant in several different perovskites [14, 25, 47], with some studies on thin-films indicating that substrate induced lattice strain may play an important roll [18, 39].

Interestingly, the similar surface compositions between LSC-82 films and LSC-64 films suggests that there is an equilibrium surface Sr composition that is independent of the deposition material composition. The majority of the surface for both films seemed to equilibrate to a Sr dopant level around $0.3 \leq x \leq 0.35$, while the small amount of higher doped surface seems to equilibrate to around $0.38 \leq x \leq 0.45$, based on the generalized thermodynamic model. Because the generalized model does not perfectly predict measured data, the exact reported values for Sr content should be examined with caution, as it is possible that there exists an offset of the reported values from the actual values that would most closely match the predicted thermodynamics. Nevertheless, this offset does not affect the general

observation of a seemingly constant composition regardless of the initial composition of the material. If lattice strain were assumed to be the main driving force for dopant redistribution, this equilibrium point may correspond to a minimized surface free energy, and would thus be experimental condition dependent. However, as the exact mechanism for redistribution is unclear it is uncertain what conditions are necessary for redistribution, and thus what conditions dictate the final composition.

In contrast to the Sr redistribution observed, there are no physical data to suggest a mechanism for deactivation of bulk material, seen in LSC-64 films. One possible explanation for this phenomenon would be the growth of a thin ion exchange blocking layer at the electrode/electrolyte interface. If ion exchange at the interface was blocked over areas that far exceed the thickness of the film, the material above those areas would require long scale ionic diffusion from the unblocked interface to become active. Because the diffusion rate to such areas would be much slower than the rate of oxygen surface exchange (due to the small thickness of the film), those areas would essentially be inactive over the range of frequencies where oxygen surface exchange was dominant. Additionally, the formation of a very thin (< 5 nm) blocking layer may be difficult to detect with ordinary compositional measurement techniques, as the total volume of material would be very small.

Another interesting observation is that at testing conditions ($< 650^{\circ}$C) analysis of the nonstationary behavior of the films indicates that the compositions and active volume are relatively stable. This is highlighted by the small changes in capacitance (Figure 2.6a) and nonlinear response (Figure 2.8) over time, as compared to the changes seen in the characteristic resistance (Figure 2.6b). The primary effect seems to be changes in the surface exchange rate coefficients $k(T)$, rather than further Sr redistribution or deactivation, which could be explained by formation and destruction of active sites (without modification to near-surface material properties). Additionally, as the assumption of a constant ratio of effective coverages (θ) with time did not seem to appreciably degrade model fits, it seems as though the rate of active site desctruction is uniform over the entire surface. Several physical processes could produce this effect, such as increased active site coverage of non-

participating molecules, and annealing of the surface leading to morphological changes (which has been observed in similarly made thin films [29]).

Finally, it is important to note that the previous analysis and discussion is intended as a general guideline to the unique behavior of the LSC thin film electrodes. It is likely that the small variations and inaccuracies seen in the analysis are due to secondary phenomena not accounted for in the theoretical model, as well as oversimplification of the primary phenomenon of Sr redistribution and deactivation. Additionally, it is possible that there are alternative primary phenomena that could have overlapping or encompassing effects. Given the characterization of similarly made films, which has to date only provided evidence of the assumed primary phenomenon of Sr redistribution (see section 2.3.1), the provided explanations seem the most likely source for observed behavior.

2.5 Summary

In this chapter, the electrochemical characteristics of epitaxially grown thin films were studied for LSC-82 and LSC-64 films, for a range of thicknesses and of operating conditions. This analysis was complicated by the unstable behavior of the films, which exhibited large changes in overall electrode resistance as a function of time and large variability among similarly grown films. While the origin of this behavior is unclear, given the relative stability of the capacitive and thermodynamic behavior, it is possible that the cause is related to creation/destruction of active sites for the exchange reaction. Additionally, because of the nature of impedance testing, normalizations could be applied to yield time independent harmonic spectra.

Several unique electrochemical characteristics were found for the thin-film, epitaxially-grown, LSC-82 and LSC-64 electrodes, distinct from predictions of freestanding bulk material. Both LSC-82 and LSC-64 films exhibited similar capacitive and nonlinear behavior despite having values different from bulk. The magnitude of the capacitance represented an increase from bulk LSC-82 and a decrease from bulk LSC-64, with a p_{O_2} dependence similar to bulk LSC-64. Similarly, the nonlinear harmonics measured for both LSC-82 and

LSC-64 films consistently followed a dissociative-adsorption rate law with compositional values close to those for bulk LSC-64, but with a weaker p_{O_2} dependence than expected. These characteristics were best captured by a mixed surface/mixed bulk model that incorporates lateral and axial inhomogeneity of cation compositions (Sr dopant), as well as large scale film deactivation in the case of LSC-64 films. The dominant contributions to electrochemical response for both LSC-82 and LSC-64 films were small portions of a similarly doped material, suggesting a likely deposition-material independent equilibrium value for film compositions. Deactivation in LSC-64 films was hypothesized to be a result of the formation of an ion transfer blocking layer at the electrode/electrolyte interface.

The complex and unstable nature of the studied thin film electrodes signifies the necessity for deeper understanding of the local phenomena controlling interfacial equilibrium. It is clear that interfacial properties can deviate significantly from those expected for bulk freestanding material. Accurate understanding of these local properties and phenomena could lead to new insights on how to enhance the overall performance of more commercially relevant porous electrodes, which are likely to be subject to the same effects at the electrode/electrolyte interface.

Chapter 3

LSC-64 POROUS ELECTRODES: EFFECTS OF HUMIDITY ON ELECTROCHEMICAL BEHAVIOR

One of the largest problems facing wide spread implementation of mixed-conducting electrodes like LSC is a high level of degradation that leads to perfromance loss, and a lack of understanding for the important processes and properties involved. In particular, LSC electrodes have increased rates of degradation in humid gas environments [11, 21, 22, 24]. Humidity-induced degredation was observed for thin film electrodes (with several different fabrication techniques), porous electrodes, and dense pellets by several different experimental techniques, including: conductivity relaxation, EIS, and isotope tracer diffusion.

The cause of humidity-induced degradation remains unclear as several reports obtain conflicting results. EIS measurements suggest that the primary effect is reduction of ionic conductivity with little to no change in surface exchange kinetics [21], while conductivity relaxation measurements suggest that it is primarily kineticlly driven with little to no changes in diffusion rates [11]. Additionally, X-ray photoelectron spectroscopy has been used to show both an increase in Sr at the surface [11] and a decrease in Sr at the surface [24].

The ability of NLEIS to provide detailed measurements of process nonlinearities, separated by timescale, make it a useful tool in determining the relative importance of co-limiting processes. NLEIS has previously been used to assess the interaction and relative importance of bulk diffusion, surface diffusion, and oxygen exchange kinetics for porous LSC electrodes [28], as well as the effects of Sr redistribution on thin film behavior (discussed in the last chapter as well as reference [29]). This work seeks to extend previous modeling work to characterize the effects of humidity on porous LSC64 electrode behavior.

3.1 Theory

As discussed in section 1.2.1, there are in general four processes that affect electrode performance (Figure 1.2). Specific electrode designs simplify electrode behavior to two processes: co-limitation of surface exchange kinetics and oxygen ion transport. To create the most appropriate physical model for the tested porous electrodes, several assumptions were made in an effort to: account for literature results mentioned in section 1.2.1, conform with previous modeling work, and limit the total degrees of freedom within the model to maintain unique results.

First, the surface exchange reaction is assumed to follow the dissociative-adsorption rate law (discussed in sections 1.4 and 2.1.2), which has been used to model LSC oxygen reduction kinetics for several different types of LSC electrodes [3, 16, 28, 29, 38, 50]. Second, the thermodynamics of the film are assumed to follow the generalized thermodynamic relationships given in section 1.3. Third, oxygen transport is assumed to follow the parallel bulk and surface transport model put forth by Lu *et al*., with the use of oxygen interstitials/ad-atoms as the surface species for ion transport [28, 38]. Finally, two sets of thermodynamics are allowed, one for the bulk and one for the near-surface bulk, to allow for changes in Sr composition as seen in the both the previous chapter on thin films and reported for thin-films and porous electrodes in references [11, 24]. To limit the model degrees of freedom the near-surface bulk is assumed to be negligibly small so that it does not contribute to the bulk thermodynamic behavior, and it is assumed to consist of a single averaged set of thermodynamics rather than a mixed surface model, in agreement with previous modeling work on similar porous electrodes [28].

3.1.1 One-Dimensional Macrohomogenous Porous Electrode Model

Adler *et al*. first proposed a simplified porous electrode model for MIECs with high ionic conductivities that considers 1-dimensional axial gradients within a porous electrode and volume averaged parameters of surface area (a), solid phase tortuosity (τ_o), and porosity

(ε) [4]. With the addition of the surface diffusion term proposed by Lu *et al*., a 1D vacancy material balance can be written in terms of superficial volume as [38]:

$$(1-\varepsilon)\,c_o\frac{\partial x_{v_b}}{\partial t} = -\frac{\partial}{\partial z}\left[\frac{(1-\varepsilon)}{\tau_o}N_{v_b}\right] + \frac{\partial}{\partial z}\left[\frac{(1-\varepsilon)}{\tau_o}N_{\mathrm{O}_s}\right] - 2ar_{\mathrm{da,O_2}} \tag{3.1}$$

where x_{v_b} is the mole fraction of oxygen vacancies (related to the oxygen nostoichiometry by $x_v = 3\delta$, c_o is the concentration of oxygen sites in the bulk, N_{v_b} is the flux of oxygen vacancies in the axial direction), N_{O_s} is the surface flux of oxygen ad-atoms, $r_{\mathrm{da,O_2}}$ is the surface exchange rate assuming the dissociative-adsorption rate law, z is a positional variable that indicates the distance from the electrode/electrolyte interface, and t is time. Even though N_{O_s} represents a surface flux, it is still written in terms of ordinary flux units (mol cm^{-2} s^{-1}), and the volume averaged parameter a has units of $\mathrm{cm}^2/\mathrm{cm}^3$ (representing a ratio of surface area to superficial volume).

The boundary conditions for the vacancy material balance are defined at the electrode/electrolyte interface and at the gas exposed electrode surface located at the top of the electrode film. For simplification, the gas exposed surface at the top of the electrode is considered to be a small fraction of the total surface area, which will contribute negligibly to the overall surface exchange rate. The gas exposed boundary is then defined as having no vacancy flux:

$$N_{v_b}|_{z=L} = 0 \tag{3.2}$$

where L is the thickness of the porous film. At the electrode/electrolyte interface, the total flux of vacancies and oxygen ad-atoms can be related to the ionic current density through Faraday's law:

$$\frac{I(t)}{2F} = \frac{\tilde{i}}{2F}\cos(\omega t) = N_{v_b}|_{z=0} - N_{\mathrm{O}_s}|_{z=0} \tag{3.3}$$

where $\tilde{i}$ and ω are the current density amplitude and frequency respectively, and F is Faraday's constant.

The fluxes of oxygen vacancies and oxygen ad-atoms are assumed to follow moderately

dilute solution theory [42]:

$$N_{v_b} = -\frac{D_{v_b} c_o}{RT} \nabla \mu_{v_b} = -D_{v_b} c_o A_b \frac{\partial x_{v_b}}{\partial y} \tag{3.4a}$$

$$N_{O_I} = -\frac{D_{\mathrm{O}_s} \frac{a}{(1-\varepsilon)} \Gamma_o}{RT} \nabla \mu_{\mathrm{O}_s} = \frac{D_{\mathrm{O}_s} \frac{a}{(1-\varepsilon)} \Gamma_o \gamma_{\mathrm{O}_s}}{x_{v_s}} A_s \frac{\partial x_{v_s}}{\partial y} \tag{3.4b}$$

where D_{v_b} and D_{O_s} are diffusion coefficients for bulk vacancies and oxygen ad-atoms respectively, A_b and A_s are the bulk and near-surface bulk thermodynamic factors, Γ_o is the concentration of oxygen sites on the surface (for oxygen ad-atoms, units of sites/cm^2), x_{v_s} is the mole fraction of near-surface bulk vacancies, γ_{O_s} is the mole fraction of oxygen ad-atoms on the surface (which can be related to x_{v_s} through a mass action equilibrium constant $K_s = x_{v_s} \gamma_{\mathrm{O}_s}$). The right hand sides of Equations (3.4a) and (3.4b) are derived using the equilibrium relationship of electrochemical potentials and the definition of the thermodynamic factors.

The concentrations of vacancies in the bulk and near-surface bulk are assumed to be in equilibrium and can be related through a constant oxygen fugacity (f_{O_2}) and the generalized thermodynamic equation (Equation (1.14)):

$$\Delta G^{\theta}_{\mathrm{vf}}(T, \mathrm{x}) - 2RT \ln x_{v_b} - 3c_{\mathrm{fit}} x_{v_b} = \Delta G^{\theta}_{\mathrm{vf}}(T, \mathrm{x}) - 2RT \ln x_{v_s} - 3c_{\mathrm{fit}} x_{v_s} \tag{3.5}$$

Because $G^{\theta}_{\mathrm{vf}}(T, \mathrm{x})$ is Sr dopant dependent, if the cause of altered thermodynamics in the near surface bulk is assumed to be due to segregation of Sr to that region, the values for bulk and near-surface bulk will differ. However, combination of the standard state free energy term and equilibrium values for vacancies ($x^o_{v_b}$ and $x^o_{v_s}$) will yield the equilibrium p_{O_2} value that is equal between the two regions.

As with the thin film case, for a porous electrode measured against a suitable reference electrode, the total voltage is given by the Nernst potential:

$$V = \frac{RT}{4F} \ln \left[\frac{f_{\mathrm{O}_2}}{p_{\mathrm{O}_2}} \right] |_{z=0} \tag{3.6}$$

The potential is defined at the bottom of the electrode as this represents the location where vacancies in the working electrode will be in equilibrium with vacancies in the reference

electrode (assuming a perfect electrolyte). This allows the use of the Nernst potential through the relationship between vacancies and oxygen fugacities (or oxygen partial pressures in the case of an equilibrated reference electrode). Because the transference number for electrons is near unity for LSC (as discussed in section 1.5) the potential within the electrode is expected to be approximately uniform throughout.

Equations (3.1-3.6), (1.26b), and (1.14) can be combined with the characteristic nondimensionalization parameters given in Table 3.1 to give a dimensionless, fixed length, 1D macrohomogeneous, porous electrode model:

$$U = \left[-\left(A_{o,b}-1\right)\chi_b - \ln\left(1+\chi_b\right)\right]|_{\zeta=0} \tag{3.7a}$$

$$\frac{\partial \chi_b}{\partial \tau} = \frac{\partial}{\partial \zeta}\left[\left(A_{\mathrm{ob}}+\left(A_{\mathrm{ob}}-1\right)\chi_b\right)\frac{\partial \chi_b}{\partial \zeta}\right] + \nu\frac{\partial}{\partial \zeta}\left[\frac{A_{\mathrm{os}}+\left(A_{\mathrm{os}}-1\right)\chi_s}{\left(\chi_s+1\right)^2}\frac{\partial \chi_s}{\partial \zeta}\right] - \kappa\rho_{\mathrm{da}} \tag{3.7b}$$

$$\frac{\partial \chi_b}{\partial \xi}|_{\zeta=1} = 0 \tag{3.7c}$$

$$\alpha\cos(\sigma\tau) = \left[A_{\mathrm{ob}}+\left(A_{\mathrm{ob}}-1\right)\chi_b\right]\frac{\partial \chi_b}{\partial \zeta}|_{\zeta=0} + \nu\frac{\left[A_{\mathrm{os}}+\left(A_{\mathrm{os}}-1\right)\chi_s\right]}{\left(1+\chi_s\right)^2}\frac{\partial \chi_s}{\partial \zeta}|_{\zeta=0} \tag{3.7d}$$

$$\rho_{\mathrm{da}} = \left[\left(1+\chi_s\right)^2 - e^{-2\left(A_{o,s}-1\right)\chi_s}\right] \tag{3.7e}$$

$$\left(A_{o,b}-1\right)\chi_b + \ln\left(1+\chi_b\right) = \left(A_{o,s}-1\right)\chi_s + \ln\left(1+\chi_s\right) \tag{3.7f}$$

where the dimensionless surface exchange rate given by Equation (3.7e) represents the rate law given by Equation (1.26b), with the additional assumptions for dissociative-adsorption.

Nondimensionalization results in two dimensionless parameters that represent relative

Quantity	Dimensional Variable	Dimensionless Form	Dimensional Group
Bulk Vacancies	x_{v_b}	$\chi_b = \frac{x^o_{v_b} - x_{v_b}}{x^o_{v_b}}$	$x^o_{v_b}$
Surface Vacancies	x_{v_s}	$\chi_b = \frac{x^o_{v_s} - x_{v_s}}{x^o_{v_s}}$	$x^o_{v_s}$
Time	t	$\tau = \frac{t}{t^*}$	$t^* = \frac{\tau_o L^2}{D_{v_b}}$
Frequency	ω	$\sigma = \omega t^*$	$\frac{1}{t^*}$
Position	z	$\zeta = \frac{z}{z^*}$	$z^* = L$
Current Density	$\tilde{i}$	$\alpha = \frac{\tilde{i}}{i^*}$	$i^* = \frac{2F(1-\varepsilon)D_{v_b} c_o x^o_{v_b}}{\tau_o L}$
Voltage	V	$U = \frac{V}{V^*} = \psi$	$V^* = \frac{RT}{2F}$
Reaction Rate	r_{da}	$\rho_{\text{da}} = \frac{r_{\text{da}}}{\Re_o}$	$\Re_o$

Table 3.1: Dimensionless parameters for the fixed length, 1D macrohomogeneous, porous electrode model.

roles of electrode processes:

$$\nu = \frac{D_{O_s} a \Gamma_o K_s}{(1-\varepsilon) D_{v_b} c_o x^o_{v_b}} \equiv \frac{\text{surface oxygen diffusion}}{\text{bulk oxygen diffusion}} \tag{3.8a}$$

$$\kappa = \frac{2\tau_o a \Re_o L^2}{(1-\varepsilon) D_{v_b} c_o x^o_{v_b}} \equiv \frac{\text{surface oxygen exchange}}{\text{bulk oxygen diffusion}} \tag{3.8b}$$

Equations (2.10a-g) can be used to solve for the first and higher order harmonics, $U_{m,m}$. Environmental conditions enter the model through the equilibrium thermodynamic factors.

3.2 Experimental Methods

3.2.1 Cell Fabrication

Two cells were tested in this study consisting of a $Ce_{0.9}Gd_{0.1}O_{1.95}$ (GDC) electrolyte pellet (with a cylindrical geometry), with circular, porous LSC-64 working and counter electrodes on the flat faces of the cylinder, and a reference electrode on the radial surface. Figure 3.1 shows an example fabricated cell. To obtain a cylindrical geometry, GDC powder (Praxiar Specialty Ceramics) was pressed uniaxially at 3x10^4 kPa and then fired at $\sim$1400°C for 4 hours. Resulting electrolyte pellets were $\sim$3mm thick.

Electrode ink was prepared by blending LSC-64 powder (Praxair), alpha-terpineol, ethyl cellulose, ethanol and oleic acid (Alfa-Aesar) in a 3 roll mill, with a 1:1 ratio of electrode powder to organics. This ink was used to screen print working and counter electrodes symmetrically on opposite sides of the electrolyte pellet with electrode areas of $\sim$0.2 cm^2. A reference electrode was created by hand painting the sides of the electrolyte pellet with the same electrode ink. Painted cells were then heated at 2°C/min to $\sim$ 1100°C, sintered for 2 hours, and cooled at the same rate to room temperature; all in an active flow of dry air.

3.2.2 Measurement Apparatus

Figure 3.2 is an illustration of the test setup used (NorECS Probostat) for electrochemical testing of porous cells. Working and counter electrodes were contacted with gold mesh

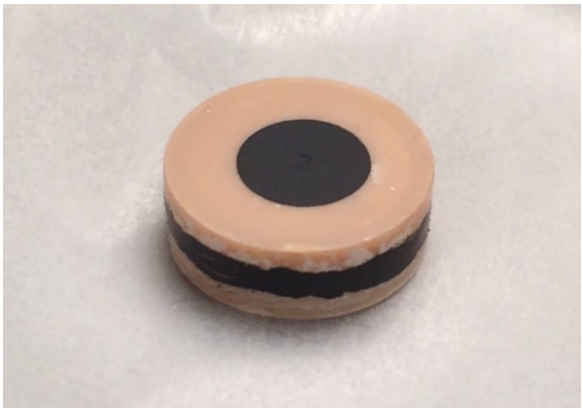

Figure 3.1: Image of a LSC-64/GDC button cell, with screen printed working and counter electrodes.

current collectors, while the reference electrode was contacted with a gold wire wrapped around the cell. The entire cell was then sandwiched between alumina plates that were held together by springs to maintain good electrode/current collector contact. Alumina plates were designed with screened holes above and below the working and counter electrodes to provide sufficient gas flow. All gold contacts were connected through a series of electrical connections to an electrochemical interface (Solartron 1287) and a high speed digitizer (National Instruments 5122) for EIS and NLEIS measurements.

3.2.3 Electrochemical Measurements

Two LSC-64 porous electrode button cells (refered to as cell1 and cell2) were tested using linear EIS and NLEIS (NLEIS data reported for cell1 only) half-cell measurements collected for oxygen partial pressures of 0.01, 0.1, and 1.0 atm, for several temperatures, and in dry and humidified gas environments. Half-cell measurements were performed with a 4 probe setup, where current passed through the working and counter electrode, while the voltage was measured (or controlled) between the working and reference electrode. This was done to isolate the response of a single electrode. For each cell, half-cell measurements

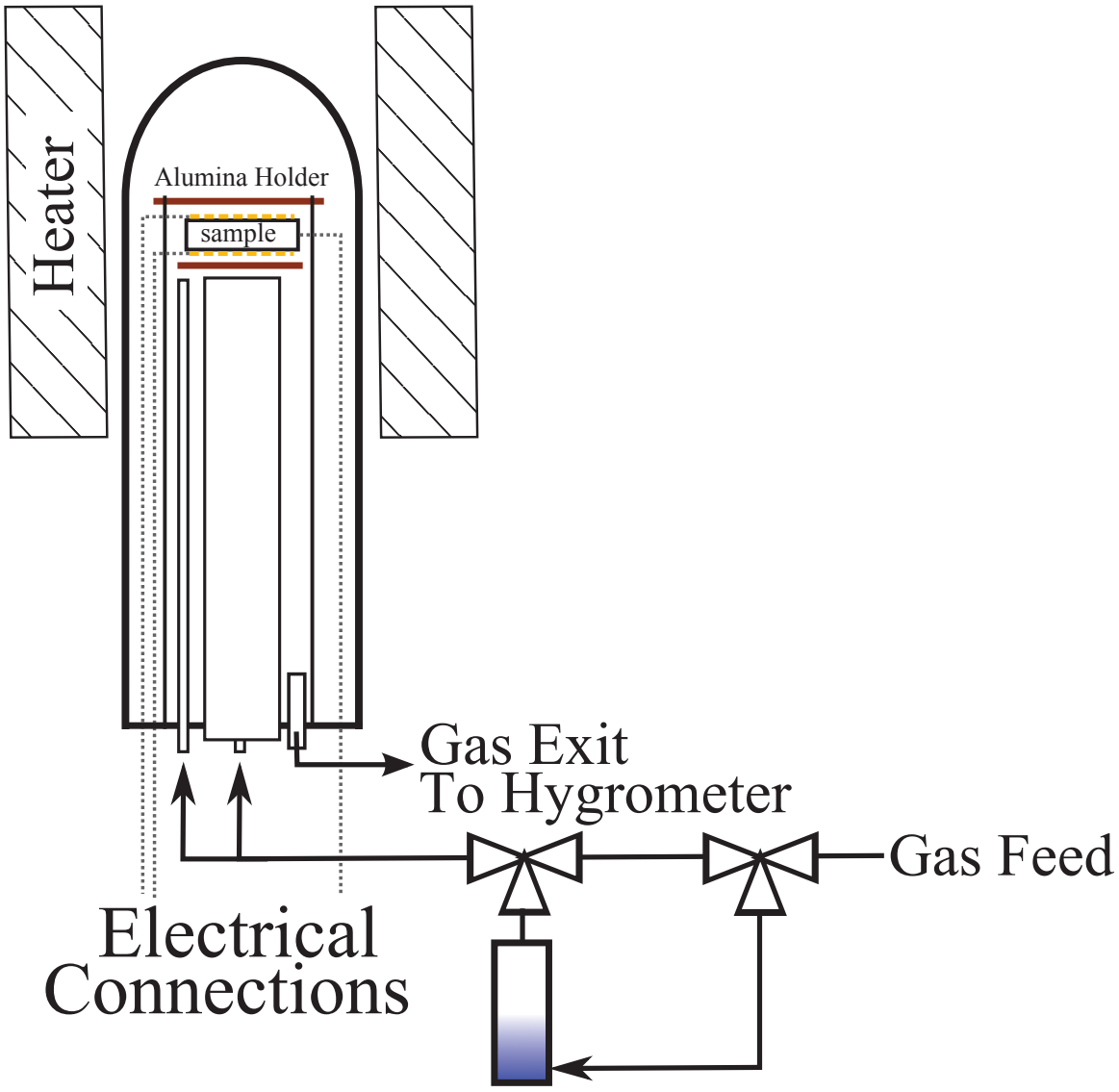

Figure 3.2: Illustration of NorECS Probostat, used for high temperature electrochemical testing of button cells.

(on both electrodes) and symmetric cell measurements were performed to ensure that the electrodes exhibited close to symmetric behavior, indicating that there were no short circuits within the setup.

At each condition studied, linear EIS was measured repeatedly until reproducible results were obtained to ensure the cell had reached equilibrium. Once reproducible impedance spectra had been obtained, an NLEIS measurement was performed, followed by another linear EIS measurement to assess any system drift. A specific order of conditions was chosen to first characterize the dry electrochemical behavior of the cell, then determine humidified behavior, and finally dry behavior post-humidification.

Cell1 was heated from room temperature to 550° (at 2°C/min). Dry electrochemical behavior was then studied at oxygen partial pressures of 0.01, 0.1, and 1.0 atm. Following testing at 550°C additional measurements were made at 650° and 750° and 1.0 atm p_{O_2}. Cell1 was then cooled back to 650° (measurements at 1.0 atm p_{O_2}) and then 550°C, where electrochemical behavior at 0.01, 0.1, and 1.0 atm of p_{O_2} was again studied. All conditions studied to this point were in dry oxygen environments, with 100% oxygen used during heating/cooling steps.

Following the dry electrochemical testing of cell1, water was introduced to the system by bubbling the incoming gas through liquid water maintained at ∼15-20°C, prior to introducing the gas mixture into the heated cell environment. Water contents of ∼2-2.5 mol% were measured by an electrical hygrometer at the gas exit of the system. Humidified electrochemical behavior was then studied at oxygen partial pressures of 0.01, 0.1, and 1.0 atm, at 550°C. The incoming gas was then switched back to dry conditions (verified by a hygrometer). Dry electrochemical behavior (post humidification) was studied at oxygen partial pressures of 0.01, 0.1, and 1.0 atm, at 550°C. The sample was then heated to 650°C and then 750°C in a dry gas environment, and measurements were taken at each temperature and 1.0 atm of oxygen.

Cell2 was heated from room temperature to 750°C (at 2°C/min) in dry 100% oxygen. A similar testing protocol to cell1 was used for cell2, with the exception of alternative

temperature testing. Dry, humidified, and then dry conditions (post-humidification) were tested at 0.01, 0.1, and 1.0 atm p_{O_2}, all at 750°C.

EIS measurements used a voltage perturbation with an amplitude of 10 mV, over a range of frequencies from 0.01 to 100,000 Hz. NLEIS measurements were performed with a current perturbation over a range of perturbation amplitudes and frequencies. Measurements consisted of 10-20 amplitudes per frequency, over a varying range of amplitudes, and 5-10 frequencies per decade, from ∼0.02 to 100,000 Hz. 0.02Hz represents a low end limitation to the test setup used. The amplitude range was chosen based on the measured size of the nonlinearities to yield at-least a 3rd order harmonic, but no more than a 5th order harmonic, at the peak frequency (determined by EIS). Additionally, as significant reversible and irreversible effects have been observed for large polarizations of $La_{1-x}Sr_xMnO_{3-\delta}$ type preovskite electrodes [37] and possibly for dense thin-film LSC electrodes [50], the voltage amplitude was kept below a maximum value of 300 mV to prevent polarization history dependent changes in electrode behavior.

3.3 Experimental Characterization and Modeling Results

3.3.1 Film Characterization

Scanning Electron Microscope (SEM) images of the fractured cross section were obtained for the two studied porous electrodes (Figure 3.3). Film thicknesses for both cells is around ∼6 - 10 μm. Examination of Figure 3.3b shows that cell2 did not obtain good sintering between electrode and electrolyte as a clear gap is seen between them on the left hand side of the image. This phenomenon was seen several times along the entire cross section length and is estimated to cover 10-20% of the electrode/electrolyte interface at the point of the cross section.

An X-Ray Diffraction (XRD) measurement was also obtained (by operator Tim Geary) for cell1 after electrochemical testing to determine the extent of any secondary phase formation. Figure 3.4 shows the diffraction pattern with labeled peaks for the LSC-64 electrode

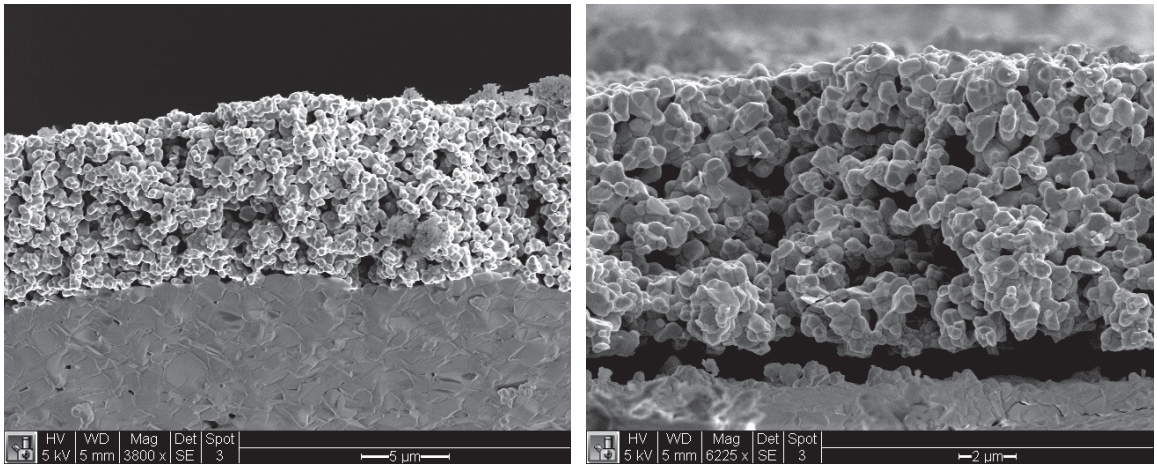

(a) Cell1, 550°C testing (b) Cell2, 750°C testing

Figure 3.3: SEM cross section image of porous LSC-64 electrodes.

and the GDC electrolyte. No significant secondary peaks were measured, indicating that any secondary phase formation is below the detection limits of XRD.

3.3.2 Linear Results

Figure 3.5 gives impedance spectra for half-cell linear EIS measurements on LSC-64 porous electrodes in a dry environment at 550°C (cell1) and 750°C (cell2) and at oxygen partial pressures of 0.01, 0.1, and 1 atm. For both cells there are 3 distinct features: a high frequency offset ($>$ 100 kHz), a moderate frequency arc ($\sim$1-100 kHz), and a low frequency arc ($\sim$0.01-100 Hz). The large p_{O_2} dependence of the low frequency arc, compared to the high frequency offset and moderate frequency arc, indicates that the low frequency arc corresponds to the co-limited porous electrode response. Because data were not collected above 100 kHz (due to limitations in the testing equipment) the exact size of the moderate frequency arc and high frequency offset are convoluted, but the likely size of the high frequency offset falls within the range of the calculated ohmic resistance due to ionic transport in GDC (25-45 Ohms at 550°C and 5-10 Ohms at 750°C) [6]. Additionally, for cell2, the

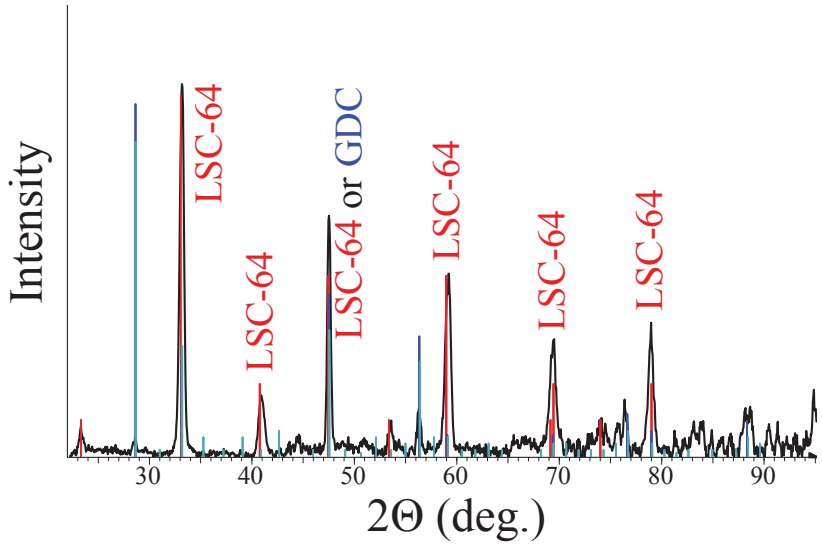

Figure 3.4: X-ray Diffraction measurement for a porous LSC-64 electrode after electrochemical testing in a humidified environment.

moderate frequency arc was occasionally suppressed, but the presence of the arc did not seem to correlate with any environmental conditions.

The low frequency electrode response impedance arcs can be characterized by their shape and characteristic parameters: arc height (R_c) and peak frequency (ω_{chem}). Impedance arcs for both cells, in dry conditions, are Gerischer-like (a half tear drop shape) and exhibit a strong p_{O_2} dependence for both R_c and ω_{chem}, which is consistent with co-limitation of kinetics and transport in an electrode. Addition of water to the gaseous environment ($\sim$2 mol%) causes significant degradation of the low frequency impedance arc, (Figure 3.6). R_c is seen to increase by factors of approximately 3x (cell1) and 1.5x (cell2) while peak frequency (ω_{chem} is seen to decrease by factors of approximately 10x (cell1) and 2x (cell2) at 550°C and 750°C, respectively. At the lowest p_{O_2} (0.01 atm) and temperature (550°C), the impedance becomes distinctly semi-circular at low frequencies. In contrast, the high frequency offset and moderate frequency arc remain largely unaffected for both cells.

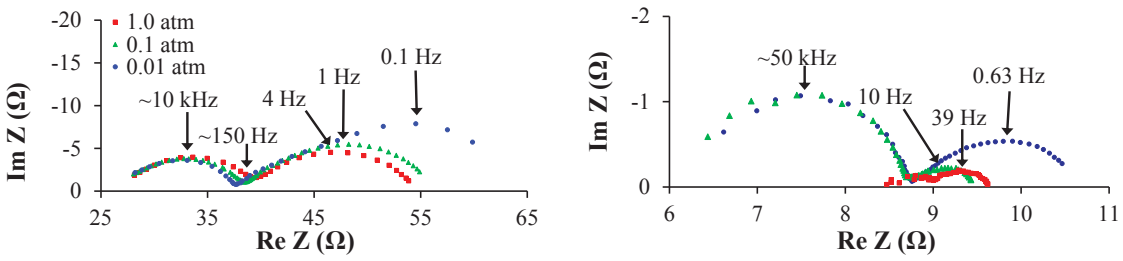

(a) Cell1, 550°C, Dry

(b) Cell2, 750°C, Dry

Figure 3.5: Impedance response of porous LSC-64 electrodes at 550°C and 750°C in 0.01 (blue circles), 0.1 (green triangles), and 1 atm (red squares) of oxygen. Characteristic frequencies of different features are indicated.

Figure 3.7 shows drifts in R_c over time. Changes in experimental conditions (temperature or humidity) are indicated by dashed vertical lines. For both cells/temperatures R_c remains relatively constant in the dry environment over 400+ hours. Upon introduction of humidity, there is a drastic increase in the degradation rate leading to the observed increases in R_c. At long timescales, values of R_c approach a plateau, although gas humidity was removed before the exact equilibrium values were obtained. It should also be noted that the long gap in measured characteristics for cell2 during phase IV was due to a shortage of 100% oxygen gas, leading to a likely drift in oxygen content during that time period.

Returning the electrodes to a dry environment results in partial regeneration of the impedance at a much smaller fraction than the original degradation ($\sim$10%). Impedance at low p_{O_2} and T remains semi-circular (Figure 3.6c). Additionally, testing at 650°C for cell1 shows that the persisting degradation in dry conditions is on the same order as degradation seen from thermal cycling to 750°C and from normal degradation over time (Figure 3.8).

In addition to the partial regeneration seen upon removal of humidity, cell2 also experience a slight increase in performance toward the end of the humidified testing conditions (Figure 3.7c). The decrease in electrode impedance is matched by a decrease electrolyte

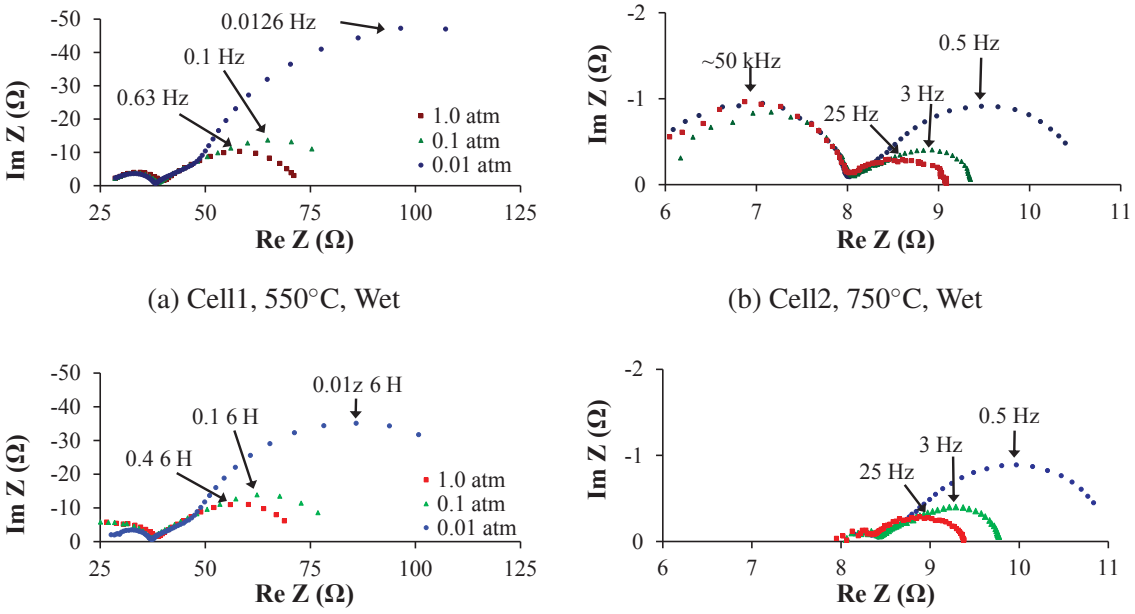

(a) Cell1, 550°C, Wet

(b) Cell2, 750°C, Wet

(c) Cell1, 550°C, Dry

(d) Cell2, 750°C, Dry

Figure 3.6: Impedance response of porous LSC-64 electrodes at 550°C and 750°C in 0.01 (blue circles), 0.1 (green triangles), and 1 atm (red squares) of oxygen, for a humidified gas environment (a,b) and a dry gas environment post-humidification (c,d). Darker colors indicated humidified gas environment. Characteristic frequencies of different features are indicated.

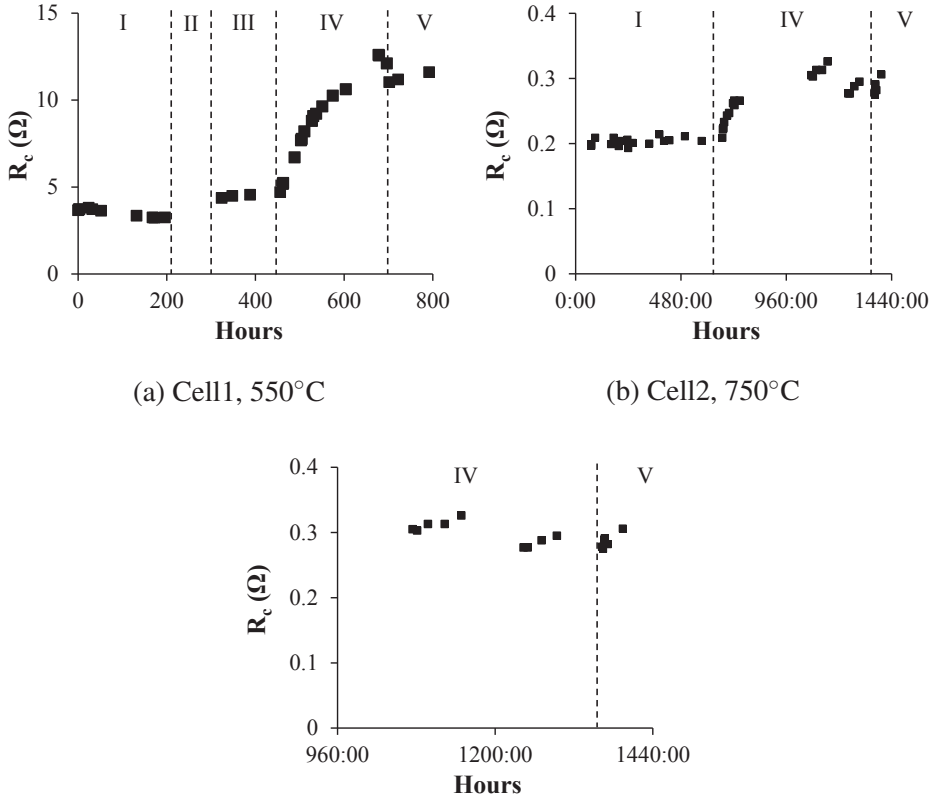

(a) Cell1, 550°C

(b) Cell2, 750°C

(c) Cell2, 750°C, expanded view of IV/V transition

Figure 3.7: Characteristic arc height (R_c) of porous LSC-64 electrodes at 550°C (cell1) and 750°C (cell2), and at 1 atm p_{O_2}. Changing environmental conditions indicated by dashed vertical lines are: dry (I), high temperatures (II), dry post-high temperature (III), humidified (IV), and dry post-humidified (V). Cell2 does not have labels II or III as no higher temperatures were measured. Wet (∼2% humidity) conditions.

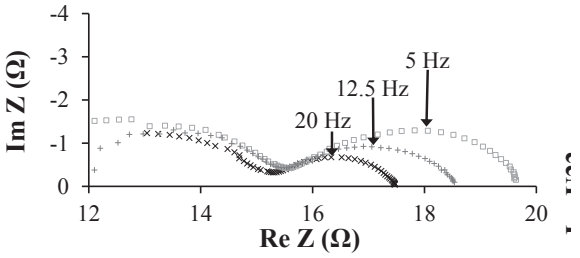

Figure 3.8: Impedance response of porous LSC-64 electrodes at 650°C measured prior to 750°C testing (×), after 750°C testing (+), and after humidity testing at 550°C (□)

resistance, suggesting that the underlying cause of the performance increase is tied to the electrode/electrolyte interface. This phenomenon was observed a few additional times in the initial dry condition testing, leading to the larger variability seen in the dry condition characteristic resistances (Figure 3.7b).

The changes in R_c and corresponding inverse changes in ω_{chem} are highly correlated over the entire range of experimental conditions tested. Figure 3.9 shows the relationship between the characteristic parameters. All impedance spectra corresponding to a Gerischer-like arc have characteristic parameters that follow a power law dependence of $1/\omega_{chem} \sim R_c^2$. For the few conditions where the impedance spectra are semi-circular, the power law dependence becomes closer to $1/\omega_{chem} \sim R_c$.

Plotting characteristic parameters as a function of p_{O_2} shows a power law dependence for both R_c and ω_{chem} that is constant over the changing environmental conditions (Figure 3.10). The only significant deviation occurs at 0.01 atm p_{O_2} and 550°C, coinciding with the change in shape of the impedance.

3.3.3 Nonlinear Response

The 2nd and 3rd harmonic spectra for a porous LSC-64 electrode (cell1) in dry conditions, at 550°C, and across a range of oxygen partial pressures, are shown in Figure 3.11. Higher

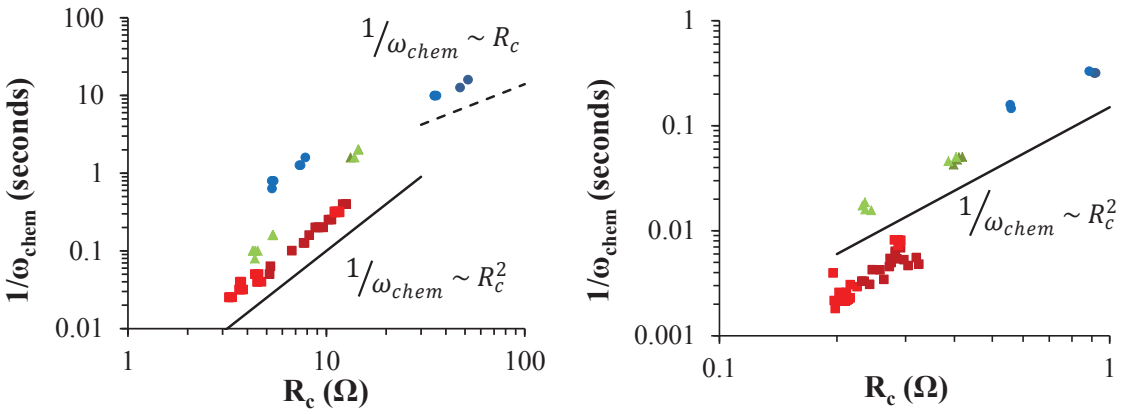

(a) Cell1, 550°C

(b) Cell2, 750°C

Figure 3.9: Correlation of R_c and ω_{chem} degradation, for porous LSC-64 electrodes, at 550°C (cell1) and 550°C (cell2), in 0.01 (blue circles), 0.1 (green triangles), and 1 atm (red squares) of oxygen, and in dry and humidified gas environments. Darker colors indicate a humidified gas environment.

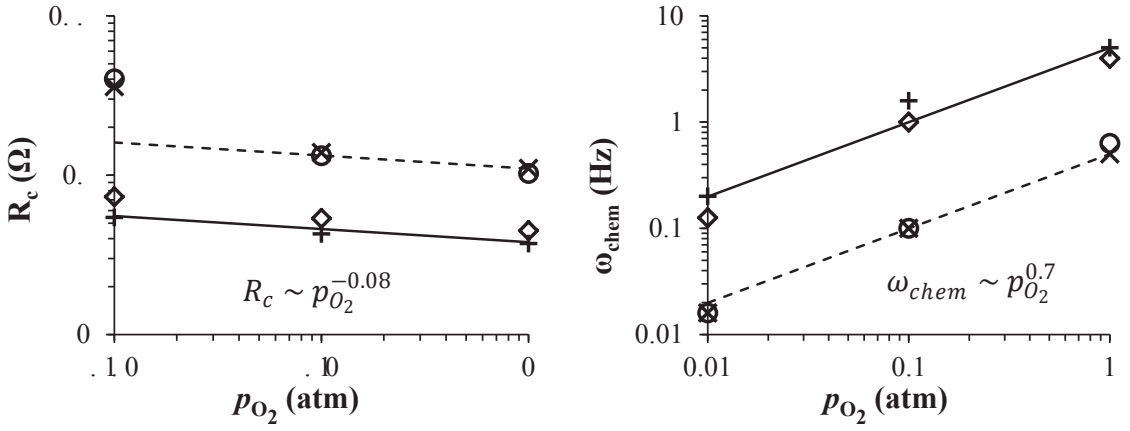

(a) Cell1, 550°C

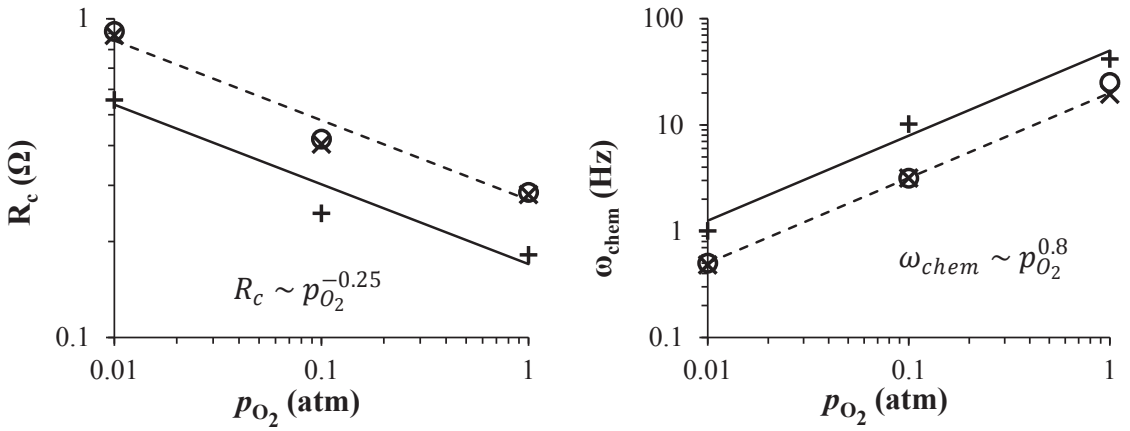

(b) Cell2, 750°C

Figure 3.10: Characteristic parameters of the impedance response for porous LSC-64 electrodes at 550°C (cell1) and 750°C (cell2), as a function of p_{O_2}, and corresponding to following phases of testing: dry (+), dry post-high temperature (◇), humidified (○), and dry post-humidified (×).

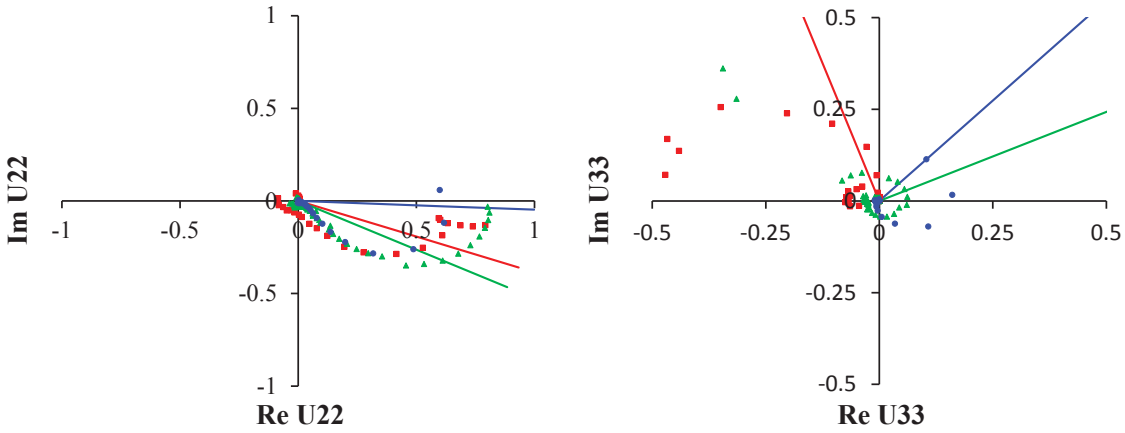

Figure 3.11: 2nd ($U_{2,2}$) and 3rd ($U_{3,3}$) harmonic spectra for a porous LSC-64 electrode at 550°C and 0.01 (blue circles), 0.1 (green triangles), and 1 atm (red squares) p_{O_2}. Phasor lines indicate frequencies of $\omega_{chem}/2$ and $\omega_{chem}/3$ for ($U_{2,2}$) and ($U_{3,3}$) respectively.

harmonic spectra can generally be characterized by the low frequency intercept of the real axis, the overall magnitude of the harmonic, and the location of the phasor line. In general the collected spectra exhibit two features. A small nonlinear feature clustered around the origin, corresponding to frequencies on the same order as the moderate frequency impedance arc, and a large nonlinear feature that spirals out from the origin, corresponding to frequencies on the same order as the low frequency impedance arc. The only exception is for dry conditions at 1.0 atm p_{O_2} where a third very low frequency arc can be seen in the 2nd harmonic, occurring at frequencies that are on the same order as the tail (at frequencies lower than the peak frequency) of the low frequency impedance arc.

The 3rd harmonic spectra are strongly p_{O_2} dependent, with a real intercept that shifts to increasingly negative values with increasing p_{O_2}. Prior to high temperature testing the phasor lines rotated counterclockwise with increasing p_{O_2}, but after high temperature testing the phasor line at 0.1 atm p_{O_2} rotated clockwise to a larger extent than at 1 and 0.01 atm p_{O_2}, breaking the trend. The 2nd harmonic spectra are only weakly p_{O_2} dependent with no

consistent trend in phasor lines.

Figure 3.12 gives harmonic spectra in humidified and post-humidified dry conditions at 550° and across a range of oxygen partial pressures. Similar to the impedance response, the introduction of humidity causes irreversible changes in the harmonic spectra. The real intercept for the dominant low frequency electrode response of the 2nd harmonic (at 1.0 atm p_{O_2}) shifts towards the positive real axis convoluting the very low frequency and low frequency features. Convolution of the two low frequency features and suppression of the moderate frequency feature leavies one dominant nonlinear feature for all harmonic spectra at 550°. The 2nd harmonic at 0.01 atm p_{O_2}, also shifts the real intercept toward the origin. Alternatively, the 3rd harmonic spectra at all p_{O_2} show a shift in the low frequency intercept toward more positive values, with the spectra at 1.0 atm p_{O_2} continuing to spiral into the 3rd quadrant. Interestingly, these trends continued even after the humidity was removed.

The shape of the harmonic spectra at 650°C and 1 atm p_{O_2} were similar to those at 550°C and 1 atm p_{O_2}, with a lager moderate frequency nonlinear feature (Figure 3.13). Because of a large amount of noise, no apparent change can be detected in the 2nd harmonic spectra between dry and post-humidified dry conditions, with the exception of a small phasor rotation clockwise. The 3rd harmonic has a similar shape for the low frequency feature before and after humid conditions, but the moderate frequency and low frequency features are reduced after humidification. These results indicate a similar but smaller affect of humidity, measured at 650°C, as what was seen at 550°C.

3.3.4 Model Results

The 1-dimensional, bulk and surface transport, fixed length porous electrode model outlined in section 3.1.1 covers only the co-limitation of kinetics and solid phase transport within the electrode. For comparison to measured data, any features corresponding to other phenomena have to be accounted for separately. To remove the unaccounted for features in the linear impedance, the ohmic and medium frequency arc resistances (real part of the impedance) are subtracted from the collected data so that the low frequency (Gerischer-

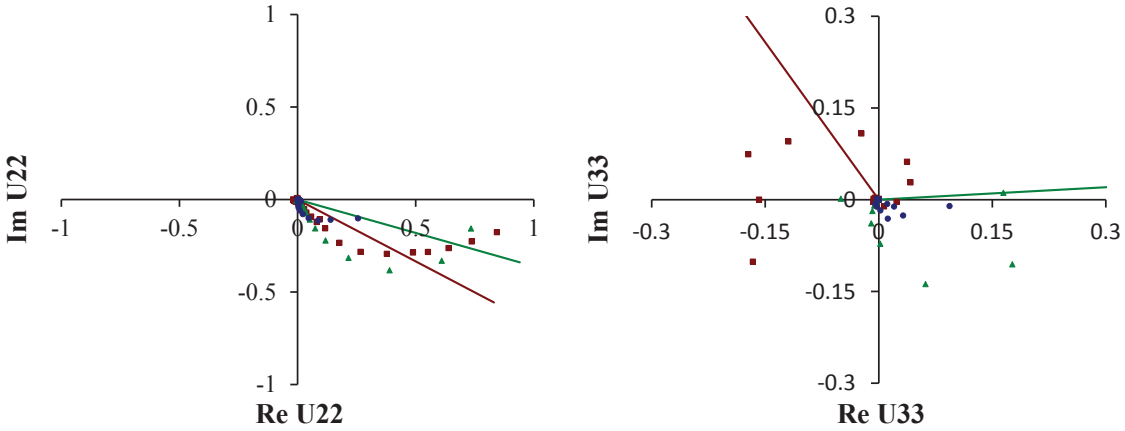

(a) Dry

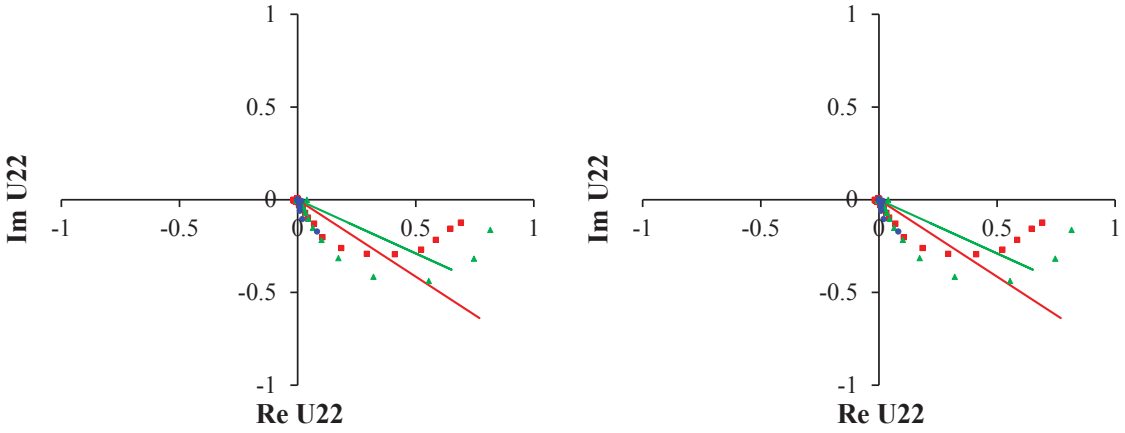

(b) Wet

Figure 3.12: Comparison of 2nd ($U_{2,2}$) and 3rd ($U_{3,3}$) harmonic spectra for a porous LSC-64 electrode at 550°C, 0.01 (blue), 0.1 (green), and 1 atm (red) p_{O_2}, and in dry (diamonds), humidified (darker colored triangles), and post-humidified dry (circles) conditions. Humidified conditions contain ∼2% gaseous water. Phasor lines indicate frequencies of $\omega_{\text{chem}}/2$ and $\omega_{\text{chem}}/3$ for ($U_{2,2}$) and ($U_{3,3}$) respectively.

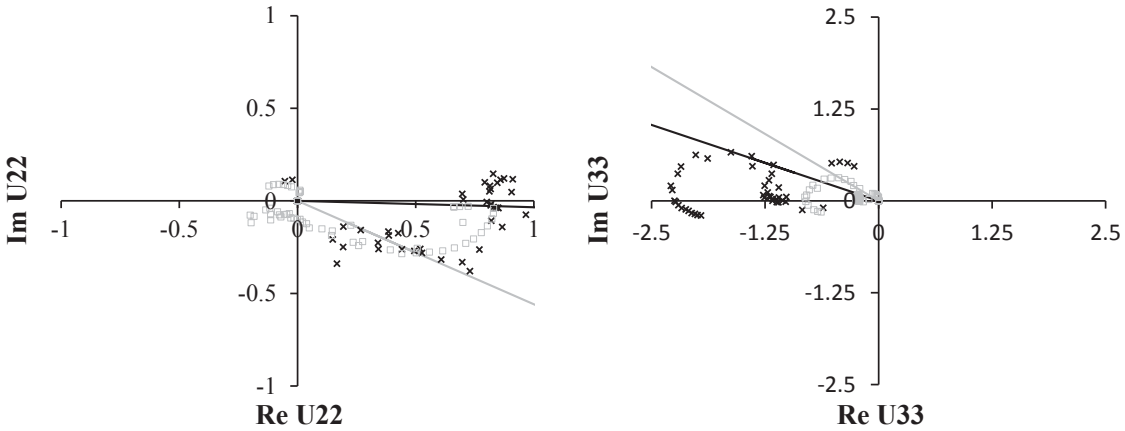

Figure 3.13: 2nd ($U_{2,2}$) and 3rd ($U_{3,3}$) harmonic spectra for a porous LSC-64 electrode at 650°C, in 1 atm p_{O_2}, before (×) and after humidity testing at 550°C (□). Phasor lines indicate frequencies of $\omega_{\text{chem}}/2$ and $\omega_{\text{chem}}/3$ for ($U_{2,2}$) and ($U_{3,3}$), respectively.

like) arc begins at the origin. The resulting electrode-only impedance is then scaled to the characteristic parameters such that the arc height of the scaled impedance is 1 rather than R_c and the peak frequency is 1 rather than ω_{chem}. This allows for dimensionless fitting of the shape of the impedance (which is controlled by relative rates of co-limiting processes), rather than absolute size of the impedance (which is controlled by values of rate coefficients and diffusivities that are often difficult to measure independently). While some features were also identified in the nonlinear harmonic spectra, no pre-fitting corrections were made, as the observed features were relatively small and difficult to deconvolute into contributions from individual process.

There were four adjustable parameters for the 1D fixed length electrode model: the dimensionless parameters κ and ν which represent the relative rates of bulk diffusion to kinetics and surface diffusion respectively, and the thermodynamic factors defining the thermodynamic behavior of the bulk ($A_{o,b}$) and near-surface bulk ($A_{o,s}$) phases. Because the bulk of the material is unlikely to deviate significantly from the original material, the total

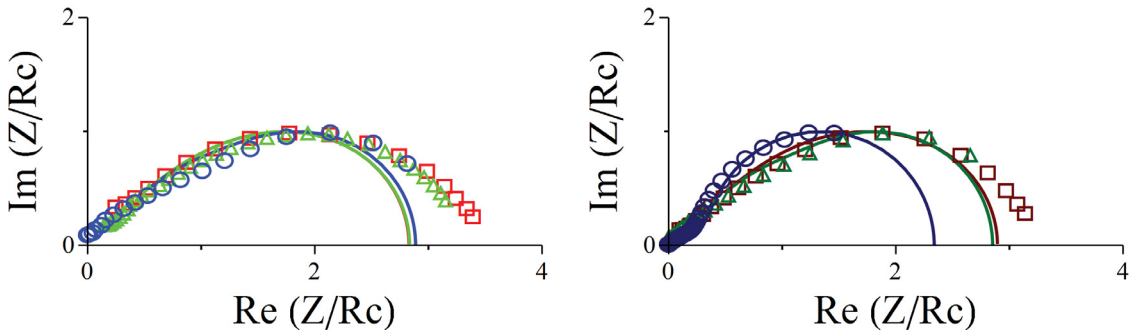

(a) Dry (b) Wet

Figure 3.14: Normalized impedance spectra for a porous LSC-64 electrode at 550°C, 0.01 (blue circles), 0.1 (green triangles), and 1 atm (red squares) pO_2, and in dry (a) and humidified (b) conditions. Darker colors indicated humidified conditions.

degrees of freedom for the fits could be reduced by assuming freestanding bulk behavior for the electrode bulk material. As discussed in section 2.4 (and in further detail in section 3.4), the generalized thermodynamic model can be susceptible to offset errors; it was therefore decided to use a value for Sr content in the generalized thermodynamic model that most closely predicted the reported thermodynamic behavior by Lankhorst *et al.* [36]. Values for the thermodynamic factor ($A_{o,b}$) were then fixed to a calculated value that best approximates the behavior of LSC-64 for each environmental condition tested. The remaining parameters were allowed to vary independently and obtained through simultaneous least squares analysis of the scaled impedance and higher order harmonics.

Figure 3.14 gives example model fits for the scaled impedance at 550°C and in dry and humidified conditions. Deviations from purely Gerischer shape (predicted by model) can be seen at the lowest frequencies for all conditions, except those that become semicircular. The extent of deviation remains approximately constant across p_{O_2} and in dry and humidified gas conditions. For those conditions, where the impedance shape becomes pre-

dominately semi-circular, the applied model was able to accurately predict the coupling of a large semi-circular arc at low frequencies and a Warburg diffusion limit at high frequencies (indicated by the $\sim 45^{\circ}$ linear portion near the origin due to the remaining transport limitations).

Figure 3.15 gives example model fits for 2nd and 3rd order harmonics for the same conditions seen in the example impedance fits. Comparison of Figure 3.15 to Figure 3.12 illustrates the accuracy of the model predictions. In general, good agreement is seen between model and data for the expected trends in both low frequency intercept and phasor rotations as well as the general shape and magnitude of the measured harmonics. Some conditions exhibit a different harmonic shape for the model due to the ability of the model to extend to frequencies below the lowest measured frequency, but agreement between the higher frequency portions and the phasor line suggest a good overall match.

Of particular interest is the ability of the model to accurately predict shifts seen in higher order harmonics upon the introduction of humidity, such as the apparent decrease in magnitude of the 2nd harmonic at 0.01 atm p_{O_2} and the coinciding shift of the low frequency intercept (toward positive real) of the 2nd harmonic spectra at 1 atm p_{O_2}. Indeed, all significant changes in the higher order harmonics, with changing environmental conditions, appear to be predicted by the model.

While the model exhibited a high level of predictive capabilities some quantitative discrepancies remained. In the largest instances, overall magnitudes may be off by a factor of 2. There are two likely driving forces contributing to the inaccuracies seen. First, the harmonic scaling of the model will differ from the harmonic scaling for measured data due to deviations of the impedance data from predicted model behavior at low frequencies. Causes of this deviation are discussed in section 3.4, but it is likely that suppression (or extension) of the Gerischer shape will affect the scaled magnitude of the higher order harmonics. Second, in a few instances, such as the 3rd order harmonic at 1 atm p_{O_2} seen in Figure 3.15, there appears to be a high frequency feature shifting the origin of the low frequency feature toward the negative real. A more pronounced version of this effect is seen in the harmonic

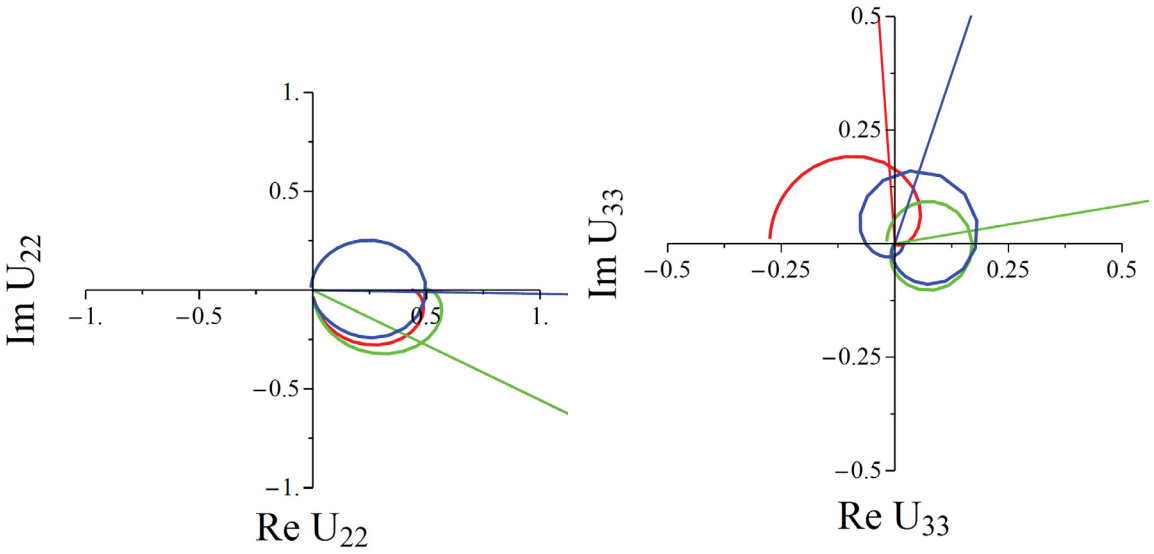

(a) Dry

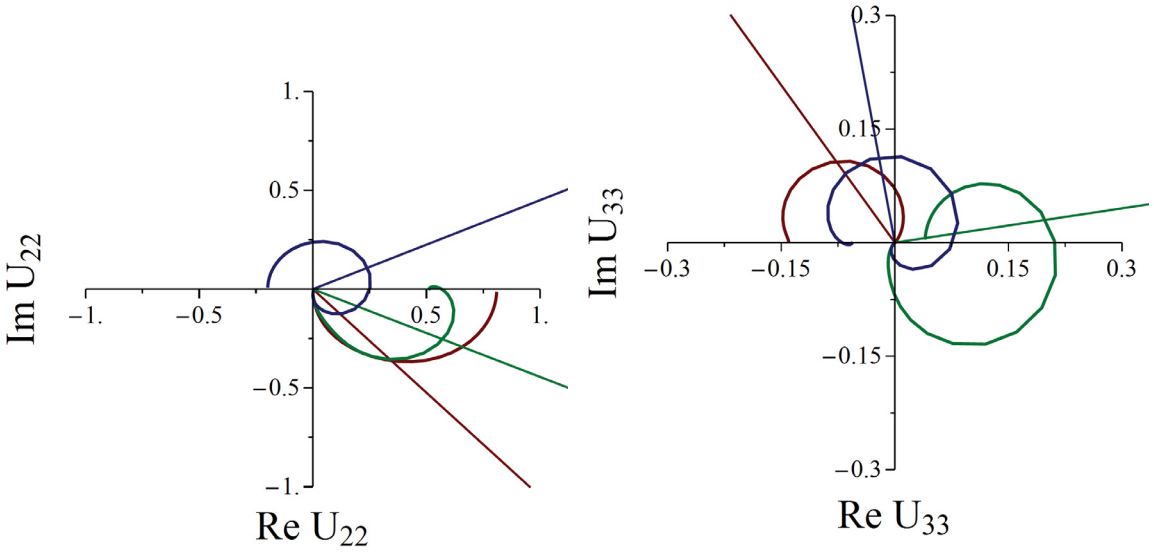

(b) Wet

Figure 3.15: Model of 2nd and 3rd order harmonic spectra for a porous LSC-64 electrode at 550°C, 0.01 (blue), 0.1 (green), and 1 atm (red) p_{O_2}, and in dry (a) and humidified (b) conditions. Darker colors indicated humidified conditions.

spectra collected at 640°C (Figure 3.13). This leads to a shift in the low frequency intercept of the harmonic, and an apparent increase in the total magnitude.

Figure 3.16 reports values obtained for adjustable fit parameters (points), along with the expected dependence predicted by the generalized thermodynamic model (lines), compared across the different environmental conditions outlined in section 3.2. The bulk thermodynamic parameter ($A_{o,b}$) does not change as it was fixed to the expected behavior for LSC-64 across all conditions, and can thus be used to evaluate the near-surface bulk thermodynamic behavior relative to bulk LSC-64. Additionally, the derived model was insensitive to values κ greater than 5, as no secondary transport effects are included in the limit of high kinetics and low transport (active length of the electrode limited to the three phase boundary). Values for κ above 5 are thus adjusted to approximate the expected trend (based on fit values for thermodynamics) with no effect on the outcome of the model. Values of κ below 5 are still based on best fits to impedance and nonlinear harmonic data.

Examining Figure 3.16 shows good agreement between the measured p_{O_2} trends in adjustable parameters and a best fit predicted p_{O_2} trend. Deviation from expected trends would indicate an inconsistent set of thermodynamic behavior. Best fit values for before and after high temperature testing (in dry conditions) are similar, as was expected from similar higher order harmonics observed (not shown). The introduction of humidity to the gaseous environment has 3 predicted affects: depression of the enhancement in near-surface bulk thermodynamics (relative to bulk), slight depression of the relative amount of surface diffusion to bulk diffusion (ν), and large depression of the relative rates of the surface exchange reaction and bulk diffusion (κ). The depression seen in κ causes a transformation from a primarily co-limited regime ($\kappa > 1$) to a primarily kinetically limited regime ($\kappa < 1$). The observed affects of humidification are seen to be irreversible upon the removal of humidity, and in fact are seen to increase slightly under dry conditions post-humidification.

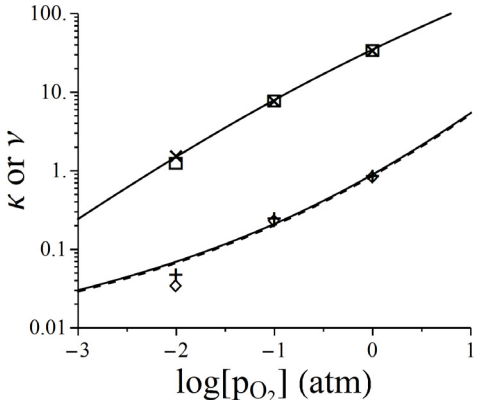

(a) Dry pre-high temperature testing ($\kappa(\times)/\nu(+)$) vs Dry post-high temperature testing ($\kappa(\square)/\nu(\diamond)$)

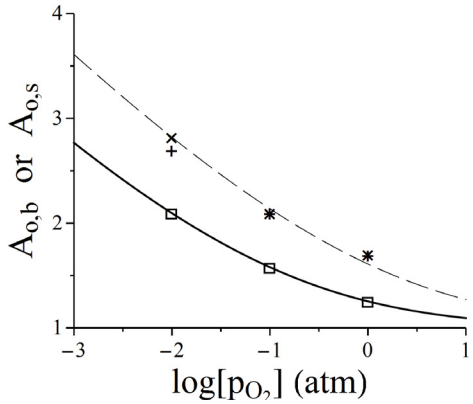

(b) Dry pre-high temperature testing ($A_{o,b}(\square)/A_{o,s}(\times)$) vs Dry post-high temperature testing ($A_{o,b}(\square)/A_{o,s}(+)$)

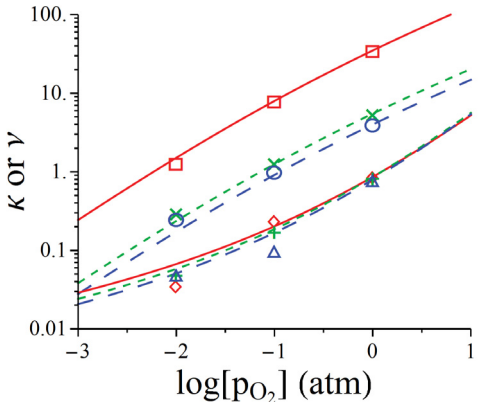

(c) Dry (Red, $\kappa(\square)/\nu(\diamond)$) vs Wet (Green, $\kappa(\times)/\nu(+)$) vs Dry post-humdified testing (Blue, $\kappa(\circ)/\nu(\triangle)$)

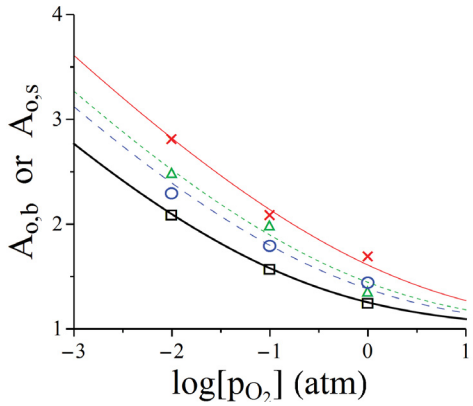

(d) Dry (Red, $A_{o,b}(\square)/A_{o,s}(\times)$) vs Wet (Green, $A_{o,b}(\square)/A_{o,b}(\triangle)$) vs Dry post-humdified testing (Blue, $A_{o,b}(\square)/A_{o,b}(\circ)$)

Figure 3.16: Best fit values of dimensionless (a,c) and thermodynamic (b,d) parameters for the 1D, fixed length, porous electrode model, for an LSC-64 electrode (cell1) at 550°C and across a range of p_{O_2}. Points indicate independently fit values at each p_{O_2}, while lines indicate dependence of parameters predicted by the generalized thermodynamic model.

3.4 Discussion

Analysis of the linear and nonlinear measurements revealed 3 distinct features that can be attributed to different electrochemical processes based on the linear and nonlinear magnitude as well as the trend with changing p_{O_2}. At the highest frequencies, a purely linear offset in the real portion of the impedance is attributed to ohmic resistance for ionic transport in the electrolyte material, with calculated resistance values in good agreement with the approximate measured values for both cells. At moderate frequencies the observed feature has slightly different characteristics for the two electrodes measured. For cell1 the moderate frequency feature consisted of a Gerischer-like shaped impedance with a small p_{O_2} dependence and small but measurable nonlinearities that become increasingly dominant with increasing temperature. For cell2 the moderate frequency feature had a semi-circular rather than Gerischer-like shape for the impedance, no observable p_{O_2} dependence, and would occasionally be absent from measured impedance. Finally, at low frequencies a strongly p_{O_2} dependent feature is measured, with a Gerischer-like (or semi-circular at specific conditions) shaped impedance spectra, and spiral shaped nonlinear harmonic spectra.

Impedance features measured in the moderate frequency range are generally attributed to interfacial kinetic resistances, but the non-semi-circular shape and small p_{O_2} dependence for cell1 make this an unlikely explanation for the observed feature. Detailed analysis of this feature is beyond the scope of this work, but nonuniform composition on the interior of the porous material, near the electrode/electrolyte interface, could have an effect on interfacial kinetics as well as modifying transport near the interface. For large deviations in transport, properties Gerischer-like shapes could be recorded, while small deviations in transport properties would result in a semi-circular shape.

The inconsistent presence of a moderate frequency feature for cell2 may also be related to the observed variability and short term changes seen in impedance response of the electrode. Throughout the electrochemical testing, cell2 would occasionally exhibit short term, correlated changes in the electrode characteristic resistance and the combined ohmic

resistance and characteristic resistance of the moderate frequency feature. Some of these changes would correlate with the disappearance or re-appearance of the moderate frequency feature. Examination of the SEM cross sectional image for cell2 (Figure 3.3b) reveals poor adhesion between the electrode and electrolyte. If the electrode/electrolyte exchange reaction is limited to a small interfacial area because of poor adhesion, current constriction and long lateral vacancy transport pathways away from the well adhered areas could increase both the ohmic and electrode resistances. As more or less electrode interfacial area comes into contact with the electrolyte (from shifts in the experimental apparatus), there would be corresponding shifts in the observed resistances and possibly transitioning from a regime with measurable kinetic resistances to the interfacial reaction to one without.

The low frequency feature is generally attributed to co-limitation of solid phase transport and surface exchange kinetics within a MIEC electrode. At the lowest frequencies measured, the low frequency impedance is seen to deviate from the expected Gerischer shape, and at the highest p_{O_2}, there is a second nonlinear feature corresponding to the same frequency range as the impedance deviations. Lu *et al.* predicted similar deviations at low frequencies for electrodes in a regime of slow kinetics relative to bulk transport, where the active area of the electrode is limited to the three phase boundary, and multi-dimensional transport becomes important [38]. The 2-dimensional transport effects are predicted to decrease as κ decreases and the cell entires a more 1-dimensional regime. This agrees with the observation that measured deviations decrease somewhat upon introduction of humidity and a predicted decrease in κ, but it does not explain the presence of a second nonlinear feature or the continued deviations seen under humidified and post-humidified conditions (which are predicted to be in regimes of primarily 1-dimensional transport). The exact cause of the remaining deviations is unclear, but given the presence of a nonlinear feature at only the highest p_{O_2} it is likely related to a solid phase chemical process, such as a secondary kinetic reaction pathway.

Modeling of the linear and nonlinear electrochemical behavior revealed two important features of the electrode behavior. First, the near-surface bulk is shown to exhibit an in-

creased thermodynamic factor from the predicted value for bulk LSC-64, corresponding to a more easily reducible surface material. Sr segregation is used to accurately explain the change in thermodynamic behavior, with increases in the near-surface bulk Sr composition (x) of $\sim 10\%$. This agrees with previous reports of higher Sr compositions near the surface of similar perovskite materials [11], and with previous modeling work on LSC-64 which predicted a slightly higher amount of Sr segregation [28]. Second, small amounts of oxygen ion based surface diffusion were necessary to account for the observed p_{O_2} trends. This is also in agreement with previous modeling work [28].

Introduction of humidity affects electrode behavior in several ways, with predictable trends in the dimensionless electrochemical response. Analysis of the dimensional linear response shows a drastic increase in the rate of degradation, as evidenced by large changes in the characteristic resistance R_c. The characteristic frequency (ω_{chem}) also exhibited an increased degradation rate, but in a way that was correlated to the degradation rate of R_c. Examining the relationship between R_c and ω_{chem} over time reveals a constant power law dependence of around $n = 2$. Work by Lu *et al.* using a more robust 2-dimensional mode gives an expected power law dependence based on changing dimensional and dimensionless parameters with a fixed thermodynamic behavior [38]. The observed dependence is close to 2 (as measured here), and examination of the dimensionless parameters used reveals that the only adjustable parameter capable of producing such a dependence is the surface exchange reaction rate coefficient. The observed changes in electrode behavior were found to be irreversible upon removal of humidity at 550°C and at 750°C, and upon heating from 550°C to 650°C.

Isolated, irreversible degradation of kinetic rate coefficients is likely related to permanent destruction of active sites. This can be achieved by strong binding of hydroxyl species to vacancy sites used for oxygen reduction. Kreuer *et al.* have reported appreciable proton conduction in similar perovskite materials through a mechanism where hydroxyl ions bind to oxygen vacancy sites [30]. Han *et al.* report a small apparent uptake of water content ($\sim$ 1 ion per 1000 unit cells), on a per volume basis, for LSC of varying compositions

at 300°C [20]. At first it would appear that the relatively small amount of water uptake would be inconsistent with the large changes in the rate coefficient necessary to produce observed degradation behavior. However, if hydroxyl ion conductivity is low and hydroxyl ion/oxygen vacancy reaction rates are assumed to be activated and occur at the most reactive sites for oxygen reduction, it is possible that hydroxyl ions are primarily limited to surface sites (giving a small value on a per volume basis), as well as the sites that are the most active (giving a larger effective change in rate coefficient), and that at elevated temperatures even more water uptake would occur.

Along with the dimensional changes seen, analysis of the nonlinear harmonics indicates two primary changes in dimensionless electrode behavior upon introduction of humidity. The active length of the electrode is seen to increase (indicated by decreases in κ), transitioning from a regime of co-limitation of transport and kinetics to primarily kinetically limited. Additionally, the thermodynamic behavior of the near surface bulk is depressed from its previously elevated values relative to bulk material. The increase in active length of the electrode agrees with the dimensional result of degradation being primarily driven by changes in reaction rate constant. As oxygen exchange kinetics become worse (independent from oxygen vacancy transport), the ratio of relative rates (κ) is expected to decrease, and gradients in oxygen vacancy concentration will extend further into the electrode until they reach end of the electrode, such that electrode response becomes independent of transport. The explanation for rate coefficient changes given previously could also explain some of the changes seen in near-surface bulk thermodynamic behavior. If Sr segregation is assumed to be the primary cause of the increased (relative to bulk) thermodynamic factors of the near-surface bulk, and if Sr is inhomogeneously distributed at the surface, it is possible that hydroxyl ion adsorption occurs most readily at the locations with the highest Sr contents, which are the most easily reducible materials. The remaining unoccupied reaction sites would then be primarily located in lower Sr content material and, as a result, the averaged surface thermodynamic factor would more closely resemble these lower Sr content materials.

3.5 Conclusions

Both linear (EIS) and nonlinear (NLEIS) electrochemical measurements were used to study the electrochemical response of a porous LSC-64 electrode in dry and humidified gas environments, while XRD and SEM techniques were used to characterize the porous film. A fixed length, 1-dimensional, combined transport model was developed to study the effects of a humidified gas environment on the electrochemical response.

The results of EIS and NLEIS characterization and modeling of two porous LSC-64 electrodes can be separated into two general categories: details of the observed electrochemical behavior, and general effects of humidity on those behaviors. LSC-64 porous electrodes exhibited three distinct processes that were separated by timescale using linear and nonlinear impedance spectroscopy: Ohmic electrolyte resistances, an unknown chemical process occurring at moderate frequencies, and co-limitation of transport and kinetics within the LSC electrode. The shape and approximate magnitude of measured impedance and higher order harmonics of the LSC-64 electrodes studied agrees with previous results for porous LSC-64 electrodes, in dry conditions [28]. Small discrepancies were accounted for in the modeling result with a slightly lower enhancement of near-surface bulk and slightly larger relative rates of surface oxygen ion transport, using a similar 1-dimensional electrode model.

Both the linear and nonlinear response for porous LSC-64 electrodes show distinct irreversible changes upon exposure to a humidified gas environment. The primary effect on dimensional linear impedance was an increased degradation rate of the characteristic resistance and frequency, which were correlated in such a way as to give a consistent power law dependence between the two. The correlated rates of degradation was concluded to be primarily driven by shifts in the surface exchange rate coefficient, based on modeling work by Lu *et al*. that predicted a similar correlation for changes in the rate coefficient [38]. Modeling of the linear impedance and nonlinear harmonics revealed a reduction in the active length of the electrode, as well as a reduction in apparent thermodynamics of

the near-surface bulk. Changes in the active length are also attributed to changes in surface exchange rate coefficient, while changes in the near-surface bulk thermodynamic factor are hypothesized to occur because of inhomogeneity in surface Sr content and preferential destruction of active sites in the higher doped Sr material through adsorption of hydroxyl ions on oxygen vacancy sites with a very high binding energy. This phenomenon would also explain the observed changes in the surface exchange rate coefficient.

Chapter 4

SIMULTANEOUS CHEMICAL-ELECTROCHEMICAL IMPEDANCE SPECTROSCOPY TECHNIQUE: FEASIBILITY ANALYSIS

Linear and Non-Linear Electrochemical Impedance Spectroscopy (EIS and NLEIS) are valuable tools for analysis of electrochemical materials and phenomena due to their ability to separate individual rate processes via timescale and nonlinearity. However, like any electrochemical measurement, these techniques are inherently limited to probing i - V relationships, which, for high temperature electrodes, often involve a convolution of kinetic and transport rates involving multiple interfaces and materials. In this work, a new technique is proposed that uses a secondary modulation of reactant gas pressure to gain additional insight into Solid Oxide Fuel Cell (SOFC) behavior. This technique is labeled Simultaneous Chemical and Electrochemical Impedance Spectroscopy (SCEIS).

SCEIS has several possible advantages over traditional EIS and NLEIS techniques. First, because the two perturbations create concentration perturbations that originate at different interfaces (the pressure perturbation originating at the electrode/gas interface and the electrochemical perturbation originating at the electrode/electrolyte interface), it may be possible to isolate portions of the response associated with each interface individually by studying the interaction between the perturbations. By distinguishing the effects of surface processes, such as kinetics and surface transport, from bulk transport, more information can be obtained about the specifics of each phenomenon. Second, by incorporating a p_{O_2} perturbation directly into the time response, it is possible to directly probe the contribution of gaseous reactant concentration to the linear and nonlinear response. The role of gas concentration can then be determined without relying on the system being stable with time

over multiple experiments.

The measurement of interaction terms in a SCEIS experiment is limited by the small amplitudes and frequencies achievable for a pressure perturbation. While electrochemical perturbations can obtain amplitudes that span many orders of magnitude, a pressure perturbation is likely limited to less than a single order of magnitude, and with maximum frequencies that are much lower. In this study, a prototype system is used to determine the feasibility of measuring dual-perturbation interaction terms.

4.1 Theory

For a current perturbation measurement on a SOFC electrode, the flux of oxygen vacancies at the electrode/electrolyte interface is directly related to the current perturbation by FaradayŠs law. As the system reaches a periodic steady state, the concentration of oxygen vacancies near the electrode/electrolyte interface develop a time dependence that is related to the current perturbation:

$$x_V \propto \cos\left(\omega_e t\right) \tag{4.1}$$

where ω_e is the frequency of the current perturbation. In a SCIES experiment, pressure is also varied sinusoidally:

$$p_{O_2} \propto \cos\left(\omega_p t\right) \tag{4.2}$$

where ω_p is the frequency of the pressure perturbation. The surface exchange reaction will depend on both the oxygen partial pressure and the oxygen vacancy concentration. From Equation (1.20) a general reaction rate can be written:

$$r_{O_2} = k_{O_2} p_{O_2}^m x_V^n \left[1 - e^{-\Lambda_j/RT}\right] \tag{4.3}$$

where n and m define the reaction order with respect to oxygen partial pressure and oxygen vacancies respectively. It is important to note that the thermodynamic driving force (Λ) is unaffected by changing reaction orders as it is defined solely by the thermodynamic behavior of the material. Examination of Equations (4.1-4.3) reveals that the surface exchange

rate will contain a multiplication of the two perturbation time dependences:

$$r_{\mathrm{O}_2} \propto \cos(\omega_e t)\cos(\omega_p t) = \frac{\cos[(\omega_e+\omega_p)t]+\cos[(\omega_e-\omega_p)t]}{2} \tag{4.4}$$

Because the flux of oxygen vacancies at the electrode surface is controlled by the surface exchange rate, a multiplied time dependence in the reaction rate will in turn induce a multiplied time dependence in the concentration of oxygen vacancies:

$$x_V \propto \frac{\cos[(\omega_e+\omega_p)t]+\cos[(\omega_e-\omega_p)t]}{2} \tag{4.5}$$

The time dependence of oxygen vacancies will thus contain a periodic component from the electrical perturbation (ω_e) a periodic component from the pressure perturbation (ω_p) and a combined periodic component from the interaction of the two perturbations ($\omega_e \pm \omega_p$).

The measured voltage of the electrode is related to the solid state oxygen fugacity within the electrode through the Nernst equation, and to the concentration of oxygen vacancies through the thermodynamic relationship between oxygen and oxygen vacancies. The voltage response will thus share the periodic steady state time dependence of oxygen vacancies. The defining equations for the voltage response can be derived in a similar manner to the response of an NLEIS experiment (see section 1.6.2), allowing for the additional time dependences of a SCEIS experiment. The applied perturbations can be written as complex exponentials describing the characteristics of the sinusoidal perturbations, while the voltage response can be written in terms of a dual Fourier series with frequencies at integer multiples of the perturbation frequencies:

$$i(t) = \frac{1}{2}\left(\tilde{i}e^{j\omega_e t}+\tilde{i}e^{-j\omega_e t}\right) \tag{4.6a}$$

$$p_{\mathrm{O}_2}(t) = \frac{1}{2}\left(\tilde{p}e^{j\omega_p t}+\tilde{p}e^{-j\omega_p t}\right) \tag{4.6b}$$

$$V = \frac{1}{2}\sum_{k=0}^{\infty}\sum_{m=0}^{\infty}\tilde{V}_{k,m}e^{j\left(k\omega_e+m\omega_p\right)t}+\hat{V}_{k,m}e^{j\left(k\omega_e-m\omega_p\right)t} + \tilde{V}_k^* e^{j\left(-k\omega_e-m\omega_p\right)t}+\hat{V}_k^* e^{j\left(-k\omega_e+m\omega_p\right)t} \tag{4.6c}$$

where $\tilde{i}$ and ω_e are the amplitude and frequency of the current perturbation, $\tilde{p}$ and ω_p are the amplitude and frequency of the pressure perturbation, $\tilde{V}_{k,m}$ and $\hat{V}_{k,m}$ are complex Fourier

coefficients corresponding to the matched ($\tilde{V}$) and unmatched ($\hat{V}$) combination of perturbation frequencies and of order k and m with respect to current and pressure respectively. Single component dependencies are given at indicies of $k = 0$ and $m = 0$ while all other sets of indicies define interaction terms.

As with NLEIS, for moderate amplitudes, a finite length power series can be used to descibe the amplitude independent voltage coefficients. In the case of a SCEIS experiment, two power series are necessary to define the relationship to current amplitude α (where $\alpha = \tilde{i}/i^*$) and p_{O_2} amplitude β (where $\beta = \tilde{p}/p_{O_2,\text{baseline}}$), giving the following power series expansions:

$$\tilde{V}_{k,m}\left(\tilde{i},\tilde{p},\omega_e,\omega_p\right) = \sum_{r=0}\sum_{s=0}\alpha^{k+2r}\beta^{m+2s}\tilde{V}_{k,k+2r,m,m+2s}\left(\omega_e,\omega_p\right) \tag{4.7a}$$

$$\hat{V}_{k,m}\left(\tilde{i},\tilde{p},\omega_e,\omega_p\right) = \sum_{r=0}\sum_{s=0}\alpha^{k+2r}\beta^{m+2s}\hat{V}_{k,k+2r,m,m+2s}\left(\omega_e,\omega_p\right) \tag{4.7b}$$

A full scale analysis of the predicted response for a model of electrode behavior measured with the SCEIS technique is beyond the scope of this work. As a limited subset of that analysis, a portion of the response of the previously described fixed-length, 1-dimensional, porous electrode model is reported over a range of current perturbations (ω_e) and the order of a general reaction rate with respect to p_{O_2} (m from Equation (4.3)) is given in Figure 4.1. Examining Figure 4.1 shows that the slope of the predicted trends is dependent on the reaction order of p_{O_2} within the surface exchange rate.

In practice, the trends of the voltage response coefficients will depend on all of the adjustable parameters within the model. As such, it is possible (but not necessary) that degenerate responses can be predicted with differing values of the adjustable parameters, at least to the extent that differences in the behavior can reasonably be distinguished. Even in such a situation, combination of NLEIS and SCEIS experiments should provide more unique and independent information over a shorter time frame than NLEIS experiments alone can provide. It may, for example, be possible to use a single NLEIS experiment and a single SCEIS experiment to uniquely define both the surface exchange reaction orders an the apparent thermodynamics of the near-surface bulk region.

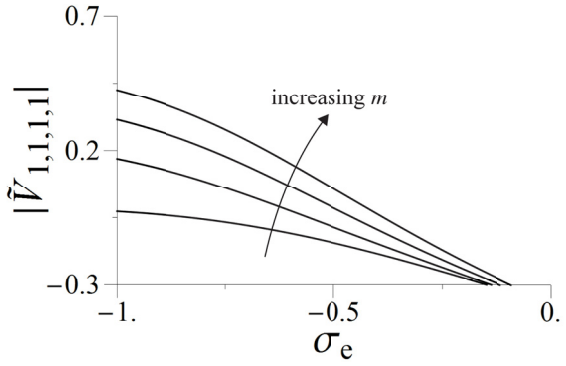

Figure 4.1: Predicted SCIES response to 1D porous model and general reaction rate. The reported results assume no surface diffusion ($\nu = 0$), a purely co-limited response ($\kappa >> 1$), thermodynamic values of the bulk and near-surface bulk that are equal to predicted values of bulk LSC-64 at 1 atm p_{O_2} and 500°C, a second order dependence of the reaction rate with respect to oxygen vacancies ($n = 2$), and a fixed value of pressure perturbation at 1/5 of the characteristic frequency of the impedance response ($\omega_p = 1/5$).

4.2 Experimental Methods

4.2.1 Measurement Apparatus

To create a variable gas environment within a high temperature container, an open ended ceramic tube was connected on one side to a piston/cylinder assembly and on the other side with a gas seal and electrical feed-throughs. An illustration of the experimental apparatus is given in Figure 4.2. The piston is a brass rod, with a diameter of ~ 2 inches, and has Viton o-rings seated in grooves machined into the perimeter of the rod. A stainless steel cylinder with an internal diameter of ~ 2 inches is used for the piston chamber and is connected to the electrolyte tube with Kwik-Flange and Ultra-Torr compression vacuum fittings. The opposite end of the electrolyte tube is sealed with an Ultra-Torr fitting modified to provide an isolated electrical feed through. The pressure within the electrochemical cell can then

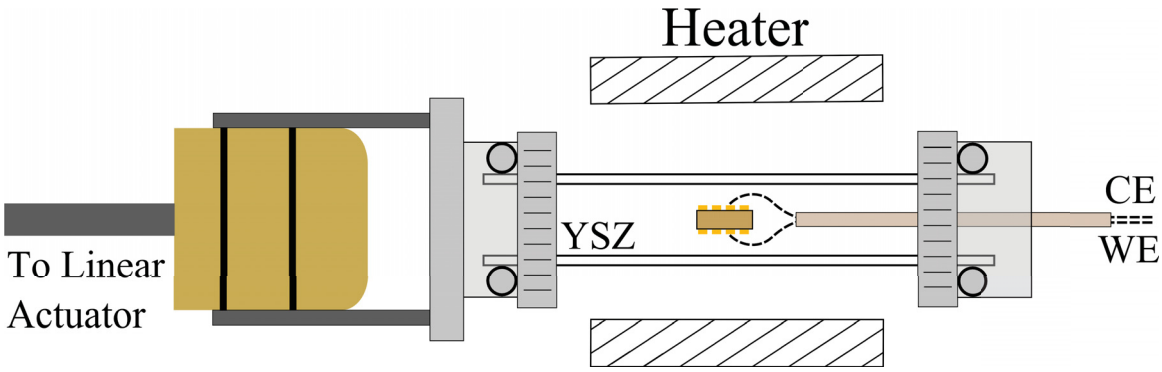

(a) Symmetric button cell setup

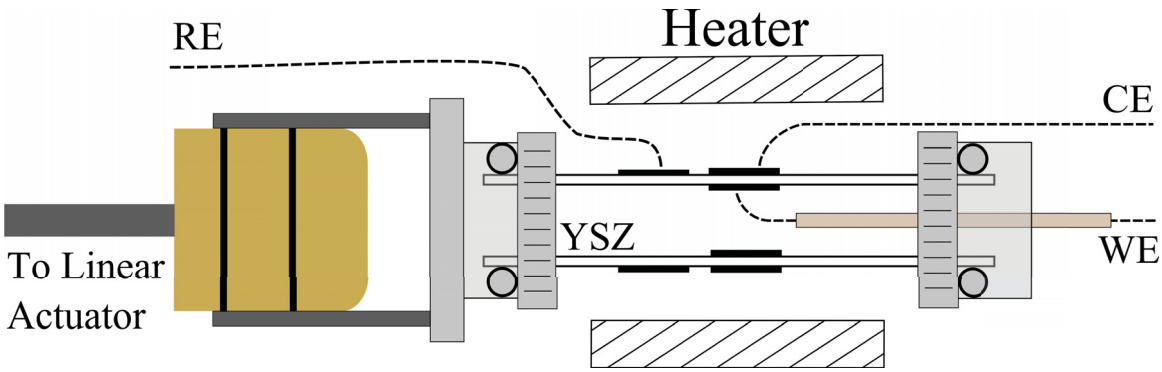

(b) Half cell tubular cell setup

Figure 4.2: Illustration of SCEIS measurement apparatus.

be varied by axial movements of the piston, controlled by a linear actuator, changing the volume of the isolated gas chamber. The piston Kwik-Flange connection is also modified to provide a gas connection to a pressure gauge for measurement purposes.

Two types of SCEIS experiments can be run with this experimental apparatus. Because the ceramic tube chosen is also a good SOFC electrolyte, concentric ring electrodes can be hand painted on the inside and outside of the YSZ tube, with a third reference electrode ring painted on the outside a few cm away from the counter electrode (Figure 4.2b). The tubular cell configuration allows for half cell measurements with a constant P_{O_2} reference

electrode. Alternatively, a button cell electrode can be placed inside of the ceramic tube and symmetric cell measurements can be run (Figure 4.2a).

4.2.2 Electrochemical Measurements

Prior to SCEIS experiments, Linear EIS measurements were taken to determine the resistance of the electrodes as a function of electrical perturbation frequency. EIS measurements employed a voltage perturbation with an amplitude of 10 mV, over a frequency range of 0.01-100,000 Hz, using a frequency response analyzer (Solartron 1260, USA) and a electrochemical interface (Solartron 1287, USA). The measured resistances were used to estimate current amplitudes that would give voltage responses in a range of 10-200 mV.

To achieve a chemical perturbation the piston position was varied in a sinusoidal pattern using a linear servo motor. Piston position was controlled using the supplied servo controller and a standalone frequency generator (Wavetek Model 21). SCEIS measurements were obtained across a range of electrical perturbation frequencies and amplitudes, and chemical perturbation frequencies and amplitudes, to determine the feasibility of measuring interaction terms and chemical perturbation terms with the achievable range of pressure perturbation amplitudes and frequencies. All measurements were taken at 500°C and in atmospheric gas conditions corresponding to a baseline p_{O_2} of ~ 0.21 atm.

4.2.3 Cell Fabrication

The cell studied in this work is similar to those studied in the previous chapter. Cell components consists of a $Ce_{0.9}Gd_{0.1}O_{1.95}$ (GDC) electrolyte pellet (with a cylindrical geometry), with circular, porous LSC-64 working and counter electrodes on the flat faces of the cylinder and a reference electrode on the radial surface. Figure 3.1 in section 3.2.1 shows an example fabricated cell. To obtain a cylindrical geometry, GDC powder (Praxiar Specialty Ceramics) was pressed uniaxially at $3x10^4$ kPa and then fired at $\sim$1400°C for 4 hours. Resulting electrolyte pellets were $\sim$3mm thick.

Electrode ink was prepared by blending LSC-64 powder (Praxair), alpha-terpineol, ethyl cellulose, ethanol and oleic acid (Alfa-Aesar) in a 3 roll mill, with a 1:1 ratio of electrode powder to organics. This ink was used to screen print working and counter electrodes symmetrically on opposite sides of the electrolyte pellet, with electrode areas of $\sim$0.2 cm^2. A reference electrode was created by hand painting the sides of the electrolyte pellet with the same electrode ink. Painted cells were then heated at 2°C/min to $\sim$ 1100°C, sintered for 2 hours, and cooled at the same rate to room temperature; all in an active flow of dry air.

4.3 Experimental Results

EIS measurements were obtained in atmospheric gas conditions at 500° for both symmetric cell and half cell configurations on each electrode. This was done to ensure that the cell was approximately symmetric and that there were no shorts within the system. Figure 4.3 gives the measured half cell and symmetric cell impedance spectra. The half cell measurements are of approximately equal magnitudes and sum to the magnitude of the symmetric cell measurement, indicating approximately symmetric behavior. Additionally, the symmetric cell exhibits fairly low nonstationary behavior, with changes in characteristic parameters of less than $\sim$ 5% over 11 days.

Following EIS measurements, SCEIS measurements were obtained over a range of perturbation frequencies and amplitudes to determine the detection and experimental limitations of the system. Detection was established by examining the Fourier Transformed (FT) voltage response to a SCIES measurement. Figure 4.4 gives representative FTs of a current perturbation and corresponding voltage response for an ordinary EIS measurement. The only detected frequency in both the current perturbation and voltage response is the current perturbation frequency (ω_e). Current FTs were similar for all SCEIS measurements, with no detectable signals other than the perturbation. Figure 4.4 also gives a representative FT for the voltage response to a SCEIS experiment (c). Signals are seen at the current perturbation frequency (ω_e), the pressure perturbation frequency (ω_p), and at the combined frequencies corresponding to interaction terms ($\omega_e \pm \omega_p$).

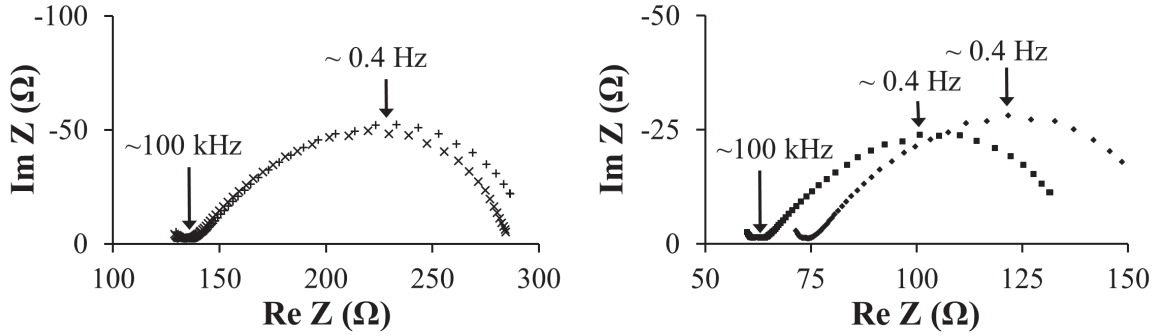

(a) Symmetric cell over time

(b) Half cell for each electrode

Figure 4.3: Symmetric and half cell Impedance results for porous LSC-64 electrode at 500°C and atmospheric gas conditions ($p_{O_2} \sim 0.21$ atm). Symmetric cell measurements are recorded ∼11 days apart. Half cell measurements are for each electrode.

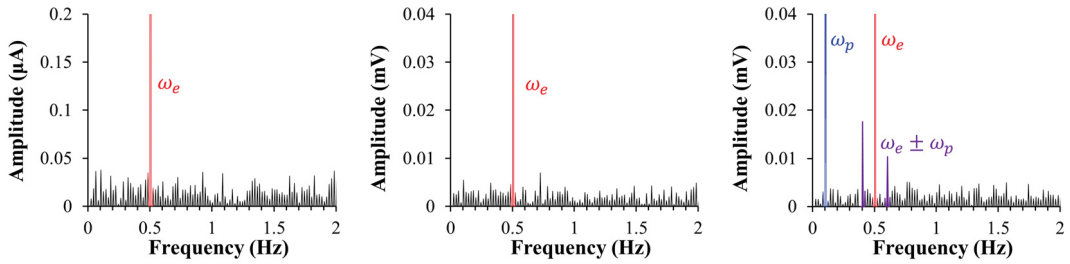

(a) Current

(b) Voltage (EIS)

(c) Voltage (SCEIS)

Figure 4.4: Representative Fourier transforms of current perturbation and voltage response to a SCEIS measurement on a porous LSC-64 electrode at 500°C and atmospheric gas conditions ($p_{O_2} \sim 0.21$ atm). Current perturbation has a frequency of 0.5 Hz and an amplitude of 0.01 mA. For (a) no pressure perturbation was applied, while (c) contains a pressure perturbation with a frequency of 0.1 Hz and an amplitude of ~ 0.2 atm p_{O_2}.

Three limitations were tested for the experimental setup: highest achievable ω_p, largest achievable $\tilde{p}$, and the largest achievable interaction terms at a moderate current amplitude. Figure 4.5 gives the voltage response to pressure perturbations at the maximum values of $\tilde{p}$ (a) and ω_p (b) with the same current perturbation. Examination of Figure 4.3a indicates that the characteristic frequency of the impedance response for the electrode is ~ 0.4 Hz, giving a maximum achievable p_{O_2} perturbation equal to the characteristic frequency at the measured conditions. The maximum achievable $\tilde{p}$ is ~ 0.32 atm p_{O_2}, which produces a voltage response amplitude that is approximately 2% of the response necessary to generate nonlinear harmonics. The maximum ω_p and maximum $\tilde{p}$ were found to be inversely related as ω_p approached the maximum achievable value. Indeed, the maximum achievable $\tilde{p}$ at the maximum achievable ω_p was ~ 0.02 atm p_{O_2}.

Figure 4.6 illustrates the maximum achievable interaction terms at a moderate current amplitude. A moderate current amplitude is defined by the number of observable nonlinear harmonics in the voltage response. Figure 4.6a gives an indication of the relative size of typical nonlinear harmonics and the maximum achievable $\tilde{p}$, while Figure 4.6b illustrates the generated interaction terms. At the larger perturbation amplitudes, many interaction terms are generated, including 3rd order pressure interactions with the primary current perturbation ($\omega_e \pm 4\omega_p$) and 1st order pressure interaction terms with higher order harmonics ($2\omega_e \pm \omega_p$ and $3\omega_e \pm \omega_p$).

4.4 Summary/Conclusions

A new electrochemical technique is proposed that includes simultaneous chemical and electrochemical perturbations (SCEIS). The technique is motivated by the limitations of linear EIS and NLEIS, primarily the convolution of electrode processes occurring within the electrode bulk and on the surface, as well as the convolution of nonstationary and nonlinear behavior over the long timescale necessary for multiple p_{O_2} measurements. Preliminary modeling results suggested that, in addition to obtaining information on a much shorter timescale, new information that was previously impossible to distinguish (such as the re-

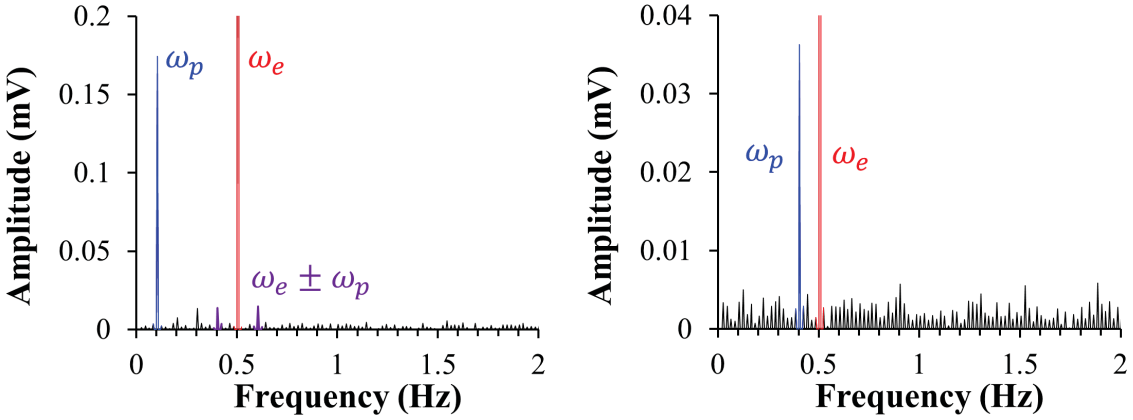

(a) Maximum Pressure Amplitude

(b) Maximum Pressure Frequency

Figure 4.5: Voltage response to a SCEIS measurements on a porous LSC-64 electrode at 500°C and atmospheric gas conditions ($p_{O_2} \sim 0.21$ atm). Current perturbation has a frequency of 0.5 Hz and an amplitude of 0.01 mA for both responses. Pressure perturbation has frequencies of 0.1 Hz (a) and 0.4 Hz (b) and amplitudes of ~ 0.32 atm (a) and ~ 0.04 atm (b) p_{O_2}.

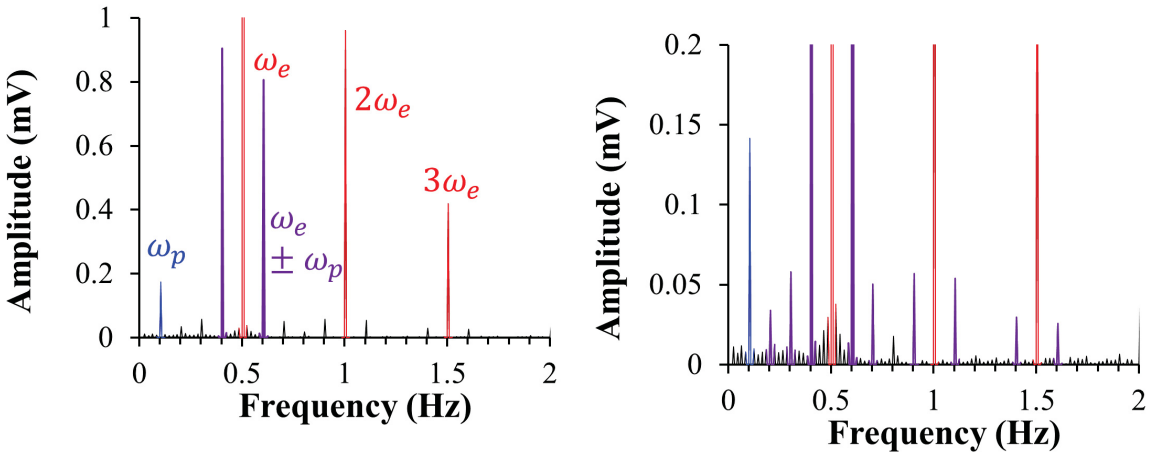

(a) Nonlinear harmonics vs maximum pressure perturbation response

(b) Interaction terms

Figure 4.6: Voltage response to a SCEIS measurements at the maximum achievable pressure perturbation amplitude, and at a moderate current perturbation amplitude, on a porous LSC-64 electrode at 500° and atmospheric gas conditions ($p_{O_2} \sim 0.21$ atm). Current perturbation has a frequency of 0.5 Hz and an amplitude of 0.6 mA, while pressure perturbation has a frequency of 0.1 Hz (a) and a amplitude of ~ 0.32 atm p_{O_2}.

action order of the surface exchange reaction with respect to p_{O_2}) may be determined by a SCEIS experiment. It was, however, previously unclear wheter a pressure perturbation could produce measurable responses and interaction terms over the limited range of achievable amplitudes and frequencies for a mechanical based perturbation.

To test the feasibility of a SCEIS experiment, an experimental apparatus was constructed to test a porous LSC-64 electrode, in a symmetric cell arrangement. The test apparatus consisted of an open ended ceramic tube connected to a piston/cylinder assembly, which was controlled by a linear servo motor and a standalone frequency generator. Maximum achievable magnitude fo the pressure perturbation was an amplitude of ~ 0.32 atm p_{O_2} and a frequency of 4 Hz. As the maximum frequency is approximately equal to the measured characteristic frequency of the impedance, it is likely that the achievable pressure frequencies will be in an appropriate range for study of the electrochemical response of similar electrodes and conditions. A pressure perturbation driven voltage response was found to be measurable at even the smallest perturbation amplitudes studied and interaction terms could easily be generated at the largest pressure amplitudes or at moderate current amplitudes. For the largest combined amplitudes tested, interaction terms coinciding with higher order harmonics were also measured, allowing for the possibility of a higher order nonlinear SCEIS experiment.

While this work provided a strong indication of general feasibility of a SCEIS experiment, analysis of collected data will require a more in-depth investigation of the appropriate models and model fitting procedures. For higher order nonlinear measurements, it is unlikely that the same scaling used for NLEIS can be utilized for a SCEIS experiment, Additionally, as the most interesting ability of a SCEIS experiment is to isolate processes occurring at different interfaces, it is likely that more complex 2 and 3-dimensional models will be necessary to appropriately model the measured behavior.

Chapter 5

SUMMARY

The main focus of this work was to better understand the role of material properties and environmental conditions on the performance and behavior of LSC electrodes. The specific environmental condition studied was the presence of humidity in the gas environment of a porous LSC electrode, which had previously been reported to have significant degradation effects. Material property investigation was accomplished through the study of highly characterized thin film electrodes, which exhibited altered thermodynamic and kinetic behaviors. The presence of in depth material characterization made possible a more detailed and accurate model for prediction of the altered behavior.

Using a combination of linear EIS and NLEIS, the electrochemical behavior of thin film, epitaxially grown, LSC-82 and LSC-64 electrodes were found to deviate significantly from the behaviors predicted by freestanding bulk material, but to be closely related to each-other. A similar magnitude of chemical capacitance was measured for both films, which represented an increase from freestanding bulk for LSC-82 and a decrease from freestanding bulk for LSC-64. In addition, the nonlinear harmonics measured for both LSC-82 and LSC-64 films seemed consistent with a dissociative-adsorption rate law and thermodynamic behavior close to that of freestanding bulk LSC-64 material. These characteristics were best captured by a mixed surface/mixed bulk model that incorporated lateral and axial inhomogeneity of cation compositions (Sr dopant), as well as large scale film deactivation in the case of LSC-64 films, hypothesized to be the result of formation of an ion transfer blocking layer at the electrode/electrolyte interface.

The determination of inhomogeneous composition effects was complicated by the unstable behavior of the thin films, which exhibited large changes in overall electrode resis-

tance as a function of time and large variability between films. The cause of the nonstationary behavior was related to creation/destruction of active sites for the exchange reaction due to the relative stability of the capacitive and thermodynamic behavior

Effects of humidification on porous electrode performance was studied for LSC-64 films, using a fixed length, 1-dimensional, combined transport model. A baseline electrochemical behavior was established in dry gas conditions and compared to previous modeling work on porous LSC-64 electrodes. Three distinct processes were identified in measured impedance spectra: Ohmic electrolyte resistances, an unknown chemical process occurring at moderate frequencies, and co-limitation of transport and kinetics within the LSC electrode. The shape and approximate magnitude of measured impedance and higher order harmonics agreed with previous results for porous LSC-64 electrodes, in dry conditions [28], with small discrepancies attributed to slightly lower values for the enhancement of near-surface bulk thermodynamics and a slightly larger relative rate of surface oxygen transport.

Upon exposure to a humidified gas environment, both the linear and nonlinear responses for porous LSC-64 electrodes showed distinct irreversible changes. EIS measurements showed a significantly increased degradation rate of characteristic parameters, which were correlated in such a way as to give a consistent power law dependence between the two. Based on modeling work by Lu *et al*., the observance of correlated rates was used as evidence of degradation being primarily driven by shifts in the surface exchange rate coefficient.

Modeling of the linear impedance and nonlinear harmonics revealed a reduction in the active length of the electrode, as well as a reduction in apparent thermodynamics of the near-surface bulk. This was related to the conclusion from impedance data through preferential destruction of active sites in a inhomogeneous surface compositions, leading to an apparent decrease in observed thermodynamics for the near-surface bulk do to unavailability of the more reactive, higher doped sites. Hydroxyl ion binding and incorporation were suggested as a possible explanation for the humidity driven destruction of active sites.

Finally, a new electrochemical technique was proposed that included a simultaneous chemical and electrochemical perturbation (SCEIS). Motivation for the technique centered around the likely ability of a SCEIS measurement to isolate processes occurring at different interfaces and to provide direct, short time frame measurements of certain system characteristics. Preliminary modeling results were used to illustrate an example case of fitting a reaction order of the surface exchange reaction with respect to p_{O_2}, based on a single SCEIS measurement.

The feasibility of a SCEIS experiment determined by fabrication of an experimental apparatus and testing of a porous LSC-64 electrode, in a symmetric cell arrangement. The test apparatus consisted of an open ended ceramic tube connected to a piston/cylinder assembly, which was controlled by a linear servo motor and a standalone frequency generator using a mechanical perturbation of piston position to vary the pressure inside a high temperature ceramic tube. A maximum achievable pressure perturbation of ~ 0.32 atm in magnitude and a frequency of 4 Hz was obtained. Additionally, the voltage response to a SCEIS measurement was found to contain a pressure perturbation component and several interaction terms at high pressure perturbations or moderate current perturbations. For the largest combined amplitudes tested interaction terms coinciding with higher order harmonics were also measured, allowing for the possibility of a higher order nonlinear SCEIS experiment. This work provided a strong indication of general feasibility of a SCEIS experiment. With further investigation of modeling techniques, it is possible that analysis of collected data can give more in-depth information on the governing process for oxygen reduction on the solid oxide fuel cell cathode LSC.

BIBLIOGRAPHY

[1] Stuart B. Adler. Mechanism and kinetics of oxygen reduction on porous La1-xSrxCoO3- delta electrodes. *Solid State Ionics*, 111(1-2):125–134, 1998.

[2] Stuart B. Adler. Factors Governing Oxygen Reduction in Solid Oxide Fuel Cell Cathodes. *Chemical Reviews*, 104(10):4791–4844, 2004.

[3] Stuart B. Adler, X.Y. Chen, and J. R. Wilson. Mechanisms and rate laws for oxygen exchange on mixed-conducting oxide surfaces. *Journal of Catalysis*, 245(1):91–109, 2007.

[4] Stuart B. Adler, J. A. Lane, and B. C. H. Steele. Electrode Kinetics of Porous Mixed-Conducting Oxygen Electrodes. *Journal of The Electrochemical Society*, 143(11):3554–3564, 1996.

[5] Stuart B. Adler, J. R. Wilson, and D. T. Schwartz. Full-spectrum nonlinear response of a sinusoidally modulated rotating disk electrode. *Physics of Fluids*, 17(6):063601, 2005.

[6] GB Balazs. ac impedance studies of rare earth oxide doped ceria. *Solid State Ionics*, 76(1-2):155–162, February 1995.

[7] R Bertacco, J P Contour, A Barth, and J Olivier. Evidence for strontium segregation in La0.7Sr0.3MnO3 thin films grown by pulsed laser deposition: consequences for tunnelling junctions. *Surface Science*, 511(1-3):366–372, 2002.

[8] H. J. M. Bouwmeester, H Kruidhof, and A Burggraaf. Importance of the surface exchange kinetics as rate limiting step in oxygen permeation through mixed-conducting oxides. *Solid State Ionics*, 72:185–194, September 1994.

[9] Nigel P Brandon, S. Skinner, and B.C.H. Steele. Recent Advances in Materials for Fuel Cells. *Annual Review of Materials Research*, 33(1):183–213, August 2003.

[10] Daniel J L Brett, Alan Atkinson, Nigel P Brandon, and Stephen J. Skinner. Intermediate temperature solid oxide fuel cells. *Chemical Society reviews*, 37(8):1568–78, August 2008.

[11] Edith Bucher, Werner Sitte, Frederik Klauser, and Erminald Bertel. Impact of humid atmospheres on oxygen exchange properties, surface-near elemental composition, and surface morphology of La0.6Sr0.4CoO3âĹŠδ. *Solid State Ionics*, 208:43–51, February 2012.

[12] Ethan J. Crumlin, Sung-Jin Ahn, D. Lee, E. Mutoro, Michael D. Biegalski, H. M. Christen, and Yang Shao-Horn. Oxygen Electrocatalysis on Epitaxial La0.6Sr0.4CoO3-Âă Perovskite Thin Films for Solid Oxide Fuel Cells. *Journal of the Electrochemical Society*, 159(7):F219–F225, January 2012.

[13] Ethan J. Crumlin, Eva Mutoro, Sung-Jin Ahn, Gerardo Jose la OâĂŹ, Donovan N. Leonard, Albina Borisevich, Michael D. Biegalski, Hans M. Christen, and Yang Shao-Horn. Oxygen Reduction Kinetics Enhancement on a Heterostructured Oxide Surface for Solid Oxide Fuel Cells. *The Journal of Physical Chemistry Letters*, 1(21):3149–3155, November 2010.

[14] Ethan J. Crumlin, Eva Mutoro, Zhi Liu, Michael E Grass, Michael D. Biegalski, Yuehlin Lee, Dane Morgan, Hans M Christen, Hendrik Bluhm, and Yang Shao-Horn. Surface strontium enrichment on highly active perovskites for oxygen electrocatalysis in solid oxide fuel cells. *Energy & Environmental Science*, 5(3):6081, 2012.

[15] R De Souza. Oxygen transport in La1âĹŠxSrxMn1âĹŠyCoyO3Âśδ perovskites Part I. Oxygen tracer diffusion. *Solid State Ionics*, 106(3-4):175–187, February 1998.

[16] Andrew DeMartini. *Measurement and Prediction of the Oxygen Surface Reaction and Thermodynamic Behavior of Solid Oxide Fuel Cell Materials*. Masters, University of Washington, January 2008.

[17] M. Finsterbusch, A. Lussier, J. A. Schaefer, and Y. U. Idzerda. Electrochemically driven cation segregation in the mixed conductor La0.6Sr0.4Co0.2Fe0.8O3-delta. *Solid State Ionics*, pages 1–4, 2012.

[18] Tim T. Fister, Dillon D. Fong, Jeffrey a. Eastman, Peter M. Baldo, Matthew J. Highland, Paul H. Fuoss, Kavaipatti R. Balasubramaniam, Joanna C. Meador, and Paul a. Salvador. In situ characterization of strontium surface segregation in epitaxial La[sub 0.7]Sr[sub 0.3]MnO[sub 3] thin films as a function of oxygen partial pressure. *Applied Physics Letters*, 93(15):151904, 2008.

[19] J. Fleig. Solid Oxide Fuel Cell Cathodes: Polarization Mechanisms and Modeling of the Electrochemical Performance. *Annual Review of Materials Research*, 33(1):361–382, August 2003.

[20] Donglin Han, Yusuke Okumura, Yoshitaro Nose, and Tetsuya Uda. Synthesis of La1âĹŠxSrxSc1âĹŠyFeyO3âĹŠδ (LSSF) and measurement of water content in LSSF, LSCF and LSC hydrated in wet artificial air at 300ÂřC. *Solid State Ionics*, 181(35-36):1601–1606, November 2010.

[21] J. Hayd and E. Ivers-Tiffee. Detailed Electrochemical Study on Nanoscaled La0.6Sr0.4CoO3- SOFC Thin-Film Cathodes in Dry, Humid and CO2-Containing Atmospheres. *Journal of the Electrochemical Society*, 160(11):F1197–F1206, September 2013.

[22] Per Hjalmarsson, Martin Sø gaard, and Mogens Mogensen. Electrochemical performance and degradation of (La0.6Sr0.4)0.99CoO3âĹŠδ as porous SOFC-cathode. *Solid State Ionics*, 179(27-32):1422–1426, September 2008.

[23] J. Jamnik and Joachim Maier. Generalised equivalent circuits for mass and charge transport: chemical capacitance and its implications. *Physical Chemistry Chemical Physics*, 3(9):1668–1678, 2001.

[24] Jong Hoon Joo, Rotraut Merkle, and Joachim Maier. Effects of water on oxygen surface exchange and degradation of mixed conducting perovskites. *Journal of Power Sources*, 196(18):7495–7499, September 2011.

[25] Khabiboulakh Katsiev, Bilge Yildiz, Kavaipatti R. Balasubramaniam, and Paul a. Salvador. Electron tunneling characteristics on La[sub 0.7]Sr[sub 0.3]MnO[sub 3] thin-film surfaces at high temperature. *Applied Physics Letters*, 95(9):092106, 2009.

[26] Tatsuya Kawada, J. Suzuki, Maya Sase, Atsushi Kaimai, K. Yashiro, Y. Nigara, Junichiro Mizusaki, K. Kawamura, and H. Yugami. Determination of Oxygen Vacancy Concentration in a Thin Film of La[sub 0.6]Sr[sub 0.4]CoO[sub 3âĹŠδ] by an Electrochemical Method. *Journal of The Electrochemical Society*, 149(7):E252, 2002.

[27] V. V. Kharton, F Marques, and Alan Atkinson. Transport properties of solid oxide electrolyte ceramics: a brief review. *Solid State Ionics*, 174(1-4):135–149, October 2004.

[28] Cortney R. Kreller. *Measurement and Modeling of Material and Microstructural Factors Governing Performance of Solid Oxide Fuel Cell Cathodes*. Phd, University of Washington, 2011.

[29] Cortney R. Kreller, T. J. McDonald, Stuart B. Adler, Ethan J. Crumlin, E. Mutoro, Sung-Jin Ahn, Gerardo Jose la OâĂŹ, Yang Shao-Horn, Michael D. Biegalski, H. M. Christen, R. R. Chater, and John a. Kilner. Origin of Enhanced Chemical Capacitance

in La0.8Sr0.2CoO3-Âă Thin Film Electrodes. *Journal of the Electrochemical Society*, 160(9):F931–F942, June 2013.

[30] K. D. Kreuer. Proton-Conducting Oxides. *Annual Review of Materials Research*, 33(1):333–359, August 2003.

[31] Markus Kubicek, Ghislain M Rupp, Stefanie Huber, Alexander Penn, Alexander K Opitz, Johannes Bernardi, Michael Stöger-Pollach, Herbert Hutter, and J. Fleig. Cation diffusion in La(0.6)Sr(0.4)CoO(3-δ) below 800 ÂřC and its relevance for Sr segregation. *Physical chemistry chemical physics : PCCP*, 16(6):2715–26, February 2014.

[32] Gerardo Jose la OâĂŹ, Sung-Jin Ahn, Ethan J. Crumlin, Y. Orikasa, Michael D. Biegalski, H. M. Christen, and Yang Shao-Horn. Catalytic activity enhancement for oxygen reduction on epitaxial perovskite thin films for solid-oxide fuel cells. *Angewandte Chemie (International ed. in English)*, 49(31):5344–7, July 2010.

[33] Gerardo Jose la OâĂŹ, B. Yildiz, S. McEuen, and Yang Shao-Horn. Probing Oxygen Reduction Reaction Kinetics of Sr-Doped LaMnO[sub 3] Supported on Y[sub 2]O[sub 3]-Stabilized ZrO[sub 2]. *Journal of The Electrochemical Society*, 154(4):B427, 2007.

[34] Gerardo Jose la OâĂŹ, B. Yildiz, S. McEuen, and Yang Shao-Horn. Probing Oxygen Reduction Reaction Kinetics of Sr-Doped LaMnO[sub 3] Supported on Y[sub 2]O[sub 3]-Stabilized ZrO[sub 2]. *Journal of The Electrochemical Society*, 154(4):B427, 2007.

[35] M. H. R. Lankhorst and H. J. M. Bouwmeester. Determination of Oxygen Nonstoichiometry and Diffusivity in Mixed Conducting Oxides by Oxygen Coulometric Titration II: Oxygen Nonstoichiometry and Defect Model for La0.8Sr0.2CoO3-delta. *Journal of the Electrochemical Society*, 144(4):1268–1273, 1997.

[36] M. H. R. Lankhorst, H. J. M. Bouwmeester, and H. Verweij. High-temperature coulometric titration of La(1-x)Sr(x)CoO(3-delta): Evidence for the effect of electronic band structure on nonstoichiometry behavior. *Journal of Solid State Chemistry*, 133(2):555–567, 1997.

[37] Hee Y. Lee, Woo Seok Choi, Seung M. Oh, H. D. Wiemhofer, and W. Gopel. Active Reaction Sites for Oxygen Reduction in La[sub 0.9]Sr[sub 0.1]MnO[sub 3]âĹŢYSZ Electrodes. *Journal of The Electrochemical Society*, 142(8):2659, 1995.

[38] Yunxiang Lu, Cortney R. Kreller, and Stuart B. Adler. Measurement and Modeling of the Impedance Characteristics of Porous La[sub 1âĹŠx]Sr[sub x]CoO[sub 3âĹŠδ] Electrodes. *Journal of The Electrochemical Society*, 156(4):B513, 2009.

[39] A. Lussier, J. Dvorak, S. Stadler, J. Holroyd, M. Liberati, E. Arenholz, S.B. Ogale, T. Wu, T. Venkatesan, and Y. U. Idzerda. Stress relaxation of La1/2Sr1/2MnO3 and La2/3Ca1/3MnO3 at solid oxide fuel cell interfaces. *Thin Solid Films*, 516(6):880–884, January 2008.

[40] Junichiro Mizusaki, Y. Mima, S. Yamauchi, and K. Fueki. Nonstoichiometry of the perovskite-type oxides La1âĹŠxSrxCoO3âĹŠδ. *Journal of Solid State Chemistry*, 80(1):102–111, May 1989.

[41] Junichiro Mizusaki, J. Tabuchi, T. Matsuura, S. Yamauchi, and K. Fueki. Electrical Conductivity and Seebeck Coefficient of Nonstoichiometric La[sub 1âĹŠx]Sr[sub x]CoO[sub 3âĹŠδ]. *Journal of The Electrochemical Society*, 136(7):2082, 1989.

[42] John Newman and Karen Thomas-Alyea. *Electrochemical Systems*. John Wiley & Sons, Inc., Hoboken, NJ, third edition, 2004.

[43] A. N. Petrov, V. A. Cherepanov, O. F. Kononchuk, and L. Ya. Gavrilova. Oxygen nonstoichiometry of La1âĹŠxSrxCoO3âĹŠδ (0 < x âL'd' 0.6). *Journal of Solid State Chemistry*, 87(1):69–76, July 1990.

[44] Martin Sø gaard, Peter Vang Hendriksen, M. Mogensen, F Poulsen, and E. Skou. Oxygen nonstoichiometry and transport properties of strontium substituted lanthanum cobaltite. *Solid State Ionics*, 177(37-38):3285–3296, 2006.

[45] Y TERAOKA, T NOBUNAGA, K OKAMOTO, N MIURA, and N YAMAZOE. Influence of constituent metal cations in substituted LaCoO3 on mixed conductivity and oxygen permeability. *Solid State Ionics*, 48(3-4):207–212, November 1991.

[46] L. M. van der Haar, M. W. den Otter, M. Morskate, H. J. M. Bouwmeester, and H. Verweij. Chemical Diffusion and Oxygen Surface Transfer of La[sub 1âĹŠx]Sr[sub x]CoO[sub 3âĹŠδ] Studied with Electrical Conductivity Relaxation. *Journal of The Electrochemical Society*, 149(3):J41, 2002.

[47] P. A. W. Van Der Heide. Systematic x-ray photoelectron spectroscopic study of La{1-x}Sr{x}-based perovskite-type oxides. *Surface and Interface Analysis*, 33(5):414–425, May 2002.

[48] W. Wagner and K. M. DeReuck. *Oxygen : international thermodynamic tables of the fluid state, 9*. Blackwell Scientific Publications, Oxford, 1987.

[49] J. R. Wilson. *Measurement and Prediction of Nonlinear Harmonics as a Tool for Dynamic Characterization of Electrochemical Systems*. Doctoral, Univeristy of Washington, 2007.

[50] J. R. Wilson, Maya Sase, Tatsuya Kawada, and Stuart B. Adler. Measurement of oxygen exchange kinetics on thin-film La0. 6Sr0. 4CoO3-delta using nonlinear electrochemical impedance spectroscopy. *Electrochemical and Solid-State Letters*, 10(5):B81–B86, 2007.

[51] J. R. Wilson, D. T. Schwartz, and Stuart B. Adler. Nonlinear electrochemical impedance spectroscopy for solid oxide fuel cell cathode materials. *Electrochimica Acta*, 51(8-9):1389–1402, 2006.

Appendix A
LEAST SQUARES ANALYSIS

Least squares fitting was an integral part of the modeling done in this work, and the general implementation involved built in least squares regression algorithms from the software package *Mathematica*. The focus of this appendix will be to outline the general fitting procedures used, highlight some of the details for the fitting algorithms, and to briefly discuss parameter sensitivity.

The two specific algorithms used are Nelder-Mead and Differential Evolution, which represent numerical global optimization methods that seek to find global minimums in noisy non-linear data sets through direct search methods. Details of the algorithms and their implementation in the software package *Mathematica* are beyond the scope of this appendix, but is important to note that both methods are numerical minimizations, allow for the constraint of adjustable parameters to a specified range, and are reasonably resistant to confinement to local minima in the search for a global minimum.

A.1 Generalized Thermodynamic Model Fitting

To derive the final form of the continuous generalized thermodynamic model, several intermediate models were fit to available nonstiochiometry data with discrete values of fitting parameters with changing Sr dopant concentration and temperature. At each step the dependent variable used for least squares regression was the overall thermodynamic driving force (Λ), and the regression algorithm used was Nelder-Mead. The first step was fitting of $\Delta G^{\theta}_{\mathrm{vf}}(T,\mathrm{x})$ and $c_{\mathrm{fit}}(T,\mathrm{x})$ from Equation 1.14 using nonstiochiometry data extracted from References [36, 40] with discrete values of parameters at each Sr dopant concentration and

temperature. The thermodynamic driving force for the equation can be written as:

$$\Lambda = -RT \ln p_{O_2} + \Delta G^{\theta}_{vf}(T,\mathrm{x}) - 2RT \ln \frac{\delta}{3} - c_{fit}(T,\mathrm{x})\delta \tag{A.1}$$

At equilibrium the thermodynamic driving force should be equal to zero, making the least squared error term simply the square of the driving force (Λ^2). To account for any offset in nonstiochiometry data (as discussed in Section 1.3.2) an offset term (δ_o) was added to those data sets which did not approach full stoichiometry at the highest p_{O_2} and lowest T, giving a modified thermodynamic driving force:

$$\Lambda = -RT \ln p_{O_2} + \Delta G^{\theta}_{vf}(T,\mathrm{x}) - 2RT \ln \frac{\delta - \delta_o}{3} - c_{fit}(\mathrm{x})\,(\delta - \delta_o) \tag{A.2}$$

Fits of $\Delta G^{\theta}_{vf}(T,\mathrm{x})$, $c_{fit}(T,\mathrm{x})$, and δ_o were obtained for each data set consisting of a single temperature and Sr dopant concentration. Examination of best fit values for $c_{fit}(T,\mathrm{x})$ and δ_o as a function of X and T showed no consistent trends and relatively small values of δ_o compared to measured nonstiochiometries (δ), with the exception of the LSC-82 data set measured by Lankhorst *et al*. (Figure 1.5). Refitting Equation (A.2) assuming a constant c_{fit} and no offsets for any data set, except the previously mentioned LSC-82 set, resulted in a nearly identical fit with the total error changing by less than 1%. Examination of $\Delta G^{\theta}_{vf}(T,\mathrm{x})$ as a function of T (Figure 1.6) reveals a mostly linear depedence. Applying a linear least squares regression to the extracted values of $\Delta G^{\theta}_{vf}(T,\mathrm{x})$ gives temperature independent values of $\Delta H^{\theta}_{vf}(\mathrm{x})$ and $\Delta S^{\theta}_{vf}(\mathrm{x})$ (Figure 1.7). While the trends of $\Delta H^{\theta}_{vf}(\mathrm{x})$ and $\Delta S^{\theta}_{vf}(\mathrm{x})$ seen in Figure 1.7 do not indicate an obvious form of x dependence, it is likely that both the entropy and enthalpy exhibit activated and will contain an exponential term. In addition, a linear term was added as a first approximation to any non-exponential behavior. The T and x dependence of each fitting parameter can the be given as:

$$c_{fit} = \text{const.} \tag{A.3a}$$

$$\Delta G^{\theta}_{vf}(T,\mathrm{x}) = \Delta H^{\theta}_{vf}(\mathrm{x}) - T\Delta S^{\theta}_{vf}(\mathrm{x}) \tag{A.3b}$$

$$\Delta H^{\theta}_{vf}(\mathrm{x}) = \Delta H^{\theta}_{fit,1} + \Delta H^{\theta}_{fit,2} e^{-x\Delta H^{\theta}_{fit,3}} + x\Delta H^{\theta}_{fit,4} \tag{A.3c}$$

$$\Delta S^{\theta}_{vf}(\mathrm{x}) = \Delta S^{\theta}_{fit,1} + \Delta S^{\theta}_{fit,2} e^{-x\Delta S^{\theta}_{fit,3}} + x\Delta S^{\theta}_{fit,4} \tag{A.3d}$$

A least squares regression on Λ, given by Equations (A.2) and (A.3), was performed accross all data sets simultaneously to obtain values of the fitting parameters c_{fit}, $\Delta H^{\theta}_{\text{fit,i}}$, and $\Delta S^{\theta}_{\text{fit,i}}$. This regression was repeated with each value of $\Delta H^{\theta}_{\text{fit,i}}$ and $\Delta S^{\theta}_{\text{fit,i}}$ independently set to zero to assess the necessity for of the additional dependence, which was accomplished through visual inspection of agreement between predicted and measured nonstiochiometry values. The linear dependence for $\Delta H^{\theta}_{\text{vf}}(\text{x})$ was found to have a negligible affect on the overall model agreement, and final values for the remaining parameters are summarized in Table 1.3.

A.2 Thin Film Model Fitting

The thin film electrode model is given by Equations (2.9a-b, 2.10a-d), where $A_{o,s1}$, $A_{o,s2}$, θ, $A_{o,b1}$, $A_{o,b2}$, and λ_1 are the adjustable fitting parameters. Using Equations (1.18c), (1.15), and (1.16), the adjustable fitting parameters become x_{s1}, x_{s2}, θ, x_{b1}, x_{b2}, and λ_1. Fits of the surface and bulk adjustable parameters were obtained independently through least squares regression of the higher order harmonics and volume specific capacitance, respectively.

Bulk parameters(x_{b1}, x_{b2}, and λ_1) were fit primily through least squares regression of the volume specific capacitance, given by Equations (2.14, 2.15), with constant values as a function of p_{O_2} but changing with T (As explained in more detail in Section 2.3.3). Bluk Sr compositional parameters x_{b1} and x_{b2} were constrained to be within the range of values used for fitting of the generalized thermodynamic model ($0.1 \leq x_b \leq 0.7$) and to have a total Sr composition less than that of the as deposited material ($x_{b1} + x_{b2} \leq 0.2$ or 0.4), while the volume fraction was constrained to physically meaningful values ($0 \leq \lambda_1 \leq 1$). Least squares regression was then done using both Nelder-Mead and Differential Evolution and assuming a range of initial values for the parameters, where each individual parameter was set to a value at the high, middle, and low end of the constrained ranges independently. The varying initial ranges and regression algorithms were used to ensure a global minimization was achieved. In all cases the fit values obtained did not change, indicating that the values represented a single global minimum.

Fits for the surface parameters (x_{s1}, x_{s2}, and θ) were obtained through simultaneous least squares regression of the 2nd and 3rd order harmonic voltage coefficients (see Sections 1.6.2 and 2.1.3), with constant values as a function of p_{O_2} but changing with T (see Section 2.3.4). Surface Sr compositional parameters x_{s1} and x_{s2} were also constrained to be within the range of values used for fitting of the generalized thermodynamic model ($0.1 \leq x_s \leq 0.7$) but were not constrained to a total Sr composition, as the surface was assumed to be of negligible volume. Least squares regression was again performed using both Nelder-Mead and Differential Evolution algorithms, and assuming a range of initial values for the parameters in a manner similar to that described for bulk fitting. In addition, because the 2nd and 3rd harmonics depend on bulk and surface properties the best fit bulk parameters were initially used. The bulk parameters were found to have a unique affect on the 2nd and 3rd harmonics and slight changes ($< 5\%$) were implemented iteratively, resolving for best fit surface parameters, to obtain a complete set of best fit compositional parameters for both the bulk and surface regions. As with the bulk regions, changes in regression algorithm and initial values did not change the obtained best fit values.

In addition to least squares regression analysis, manual parameter manipulation and visual inspection was used to assess the likelihood of degenerate model fits. While the fitting parameters often had overlapping effects at a single T and p_{O_2}, across a range of p_{O_2} there did not appear to be any alternative fits that could capture the observed trends in both the higher order harmonics and VSC.

A.3 Porous Model Fitting

The porous electrode model is given by Equations (2.10a-g), where $A_{o,s}$, κ, and ν are the adjustable fitting parameters (with $A_{o,b}$ fixed to predicted values for LSC-64). Fitting of the porous electrode model was very similar to that of the thin film electrode model. The independent variables used for least squares regression were the 2nd and 3rd order harmonic voltage coefficients, and both Nelder-Mead and Differential Evolution regression algorithms were used, along with a range of initial values for adjustable parameters (varied

independently to ensure a global minimum). Unlike the thin film model, adjustable parameters were allowed to vary as a function of p_{O_2} independent of the predicted trends from the generalized thermodynamic model. However, fits to a porous model that defined trends in p_{O_2} based on predictions of the generalized thermodynamic model were used to estimate likely initial values for the p_{O_2} independent fits. As with the thin film model, variation of initial values and regression algorithms did not alter the best fit values for adjustable parameters, indicating a global minimum was reached.